The University Of Sheffield.

Comparison of hyperpolarised gas MRI and CT-based surrogates of ventilation

Bilal Ahmed Tahir

BEng (Hons), MSc, MSc, Dip. IPEM

A thesis submitted for the degree of Doctor of Philosophy

Academic Unit of Clinical Oncology

Department of Oncology & Metabolism

Faculty of Medicine

The University of Sheffield

December 2016

Abstract

Background: Non-contrast CT-based surrogates of regional ventilation derived from pulmonary images acquired at multiple inflation levels have been proposed as alternatives to established modalities. However, their physiological accuracy has yet to be validated prior to clinical translation.

Purpose: To address the hypothesis that these surrogates can provide information comparable to a direct measure of ventilation from hyperpolarised gas MRI ventilation via:

i. development of a methodology for registering CT and gas MRI.
ii. comparison of these surrogates with gas MRI at the lobar level.
iii. evaluation of the impact of inflation levels when comparing gas MRI and ventilation CT.
iv. development of an image acquisition and analysis framework to facilitate spatial correlations of both techniques.
v. assessment of the effect of using different gases on the correlation.

Methods:

i. A method to indirectly register gas MRI to CT via same-breath ^{1}H-structural MR images was developed and its accuracy was assessed.
ii. A ventilation model based on expansion of lobar CT segmentations was compared with gas MRI lobar ventilation measurements.
iii. The spatial overlap of ventilation CT was compared to gas MRI acquired at two different inflation levels.
iv. An image acquisition protocol was designed to minimise differences in acquisition settings between scans such as posture and breathing manoeuvre and analysis methods were developed to enable direct regional and voxel level correlations.
v. The effect of using two different noble gases, namely, ^{3}He and ^{129}Xe, on correlation with ventilation CT was assessed.

Results:

i. The indirect method of registration was more accurate than direct registration.
ii. Despite subtle differences, lobar ventilation measurements derived from CT and hyperpolarised gas MRI were comparable.
iii. Comparison of ventilation CT and gas MRI varied with inflation state.
iv. The spatial correlation between ventilation CT and gas MRI increased at coarser levels.
v. A marked improvement in correlation was observed for ^{3}He and ^{129}Xe MRI in contrast to when ventilation CT was compared with either ^{3}He and ^{129}Xe MRI.

Conclusion: Although CT-based surrogates of ventilation show promise for replacing established ventilation modalities such as hyperpolarised gas MRI, particularly at coarser levels, they cannot be assumed to be equivalent to the techniques they purport to replace.

Acknowledgements

First and foremost, I owe my deepest gratitude to my principal supervisor, Dr Rob Ireland, for being relentless in securing funding for this research. Furthermore, he has been a constant source of support throughout the PhD and has ensured that I enjoy and take pride in my research. I also thank him for all the effort he put into training me and for allowing me to attend numerous conferences and training workshops and encouraging me to develop as an independent researcher. Equally, I would like to express my special appreciation and thanks to my second supervisor, Professor Jim Wild, for the considerable time and effort he has devoted to furthering my research. He has also taught me how to survive in an academic research environment and has been instrumental in allowing me to grow as a research scientist.

I would also like to thank the whole Polarised Lung and Respiratory Imaging Systems (POLARIS) team for welcoming me to their laboratory. In particular, I thank (in no particular order) Helen Marshall, Felix Horn, Guilhem Collier, Andy Swift, Paul Hughes, Neil Stewart, Fung Chan, Madhwesha Rao, Laurie Smith, Graham Norquay, Nick Weatherley, Chris Johns, Martin Brook and Alberto Biancardi for greatly contributing to my work and personal development. Likewise, I thank my colleagues at Weston Park Hospital and Clinical Oncology who have always been approachable and willing to help. I am particularly grateful to Matthew Hatton, James Swinscoe and Kerry Hart.

Over the past few years, I have been fortunate to receive financial support from a variety of sources to conduct the work contained in this thesis. This includes a prestigious research endowment from the James Morrison Trust in Sheffield and additional funding from Weston Park Cancer Charity.

Finally, all this would have been impossible without the support of my loving family for their unceasing encouragement and patience throughout my studies.

Bilal Tahir

Contents

List of Figures

List of Tables

Abbreviations

2D	Two Dimensional
3D	Three Dimensional
4D	Four Dimensional
COPD	Chronic obstructive pulmonary disease
CT	Computed Tomography
DIR	Deformable image registration
DSC	Dice Similarity Coefficient
DTPA	Diethylenetriamine-pentaacetic Acid
FRC	Functional Residual Capacity
Galligas	Gallium-68
Gy	Gray
He	Helium
HP	Hyperpolarised
HU	Hounsfield Units
IMRT	Intensity Modulated Radiotherapy
MAA	Macroaggregated Albumin
MRI	Magnetic Resonance Imaging
NSCLC	Non-small cell lung cancer
PET	Positron Emission Tomography
ROI	Region of interest
RT	Radiotherapy
RV	Residual Volume
SBRT	Stereotactic Body Radiation Therapy
SCC	Spearman Correlation Coefficient
SGV	Specific gas volume
SPECT	Single Photon Emission Computerised Tomography
TLC	Total Lung Capacity
TRE	Target Registration Error
VMAT	Volumetric Modulated Arc Therapy
Xe	Xenon

Chapter 1
Introduction

Several methods of generating non-contrast CT-based surrogates of regional ventilation derived from pulmonary CT images acquired at different inflation levels have been proposed. These methods are based on the assumption that either lung expansion and/or density changes of corresponding parenchymal voxels equate to ventilation. However, their physiological accuracy has yet to be validated prior to widespread clinical use. Thus, a central focus of enquiry in the field has been the validation of these techniques against more established measures of pulmonary function including imaging modalities. In this chapter, the underlying theory of the techniques and previous validation studies are reviewed. The overall aim and specific objectives of the thesis are also introduced.

1.1 Motivation

Worldwide, lung cancer is the leading cause of cancer deaths with the majority (> 87%) of patients dying within 5 years of their initial diagnosis (Gibson *et al.*, 2013). Despite significant improvements in alternative treatment techniques, surgical resection remains the standard of care for early stage non-small cell lung cancer (NSCLC) offering cancer control, improved overall survival and quality of life. However, a majority of lung cancer patients smoke and smoking is an important risk factor for other pulmonary co-morbidities including chronic obstructive pulmonary disease (COPD), which is present in around 75% of patients (Papi *et al.*, 2004). Such pre-existing impairment of lung function means patients are at higher risk of post-operative morbidity and mortality and pulmonary complications have been shown to be the most costly post-operative complication, resulting in longer hospital stays (Dimick *et al.*, 2004). A significant

proportion of patients with early stage NSCLC are unable to tolerate the further loss in lung function from resection and are thus unsuitable for curative surgery. Radiotherapy provides an alternative, potentially curative, treatment modality. However, its efficacy is limited by the incidence of radiation induced pneumonitis for cancer patients who already tend to suffer from reduced pre-treatment pulmonary function (Rodrigues *et al.*, 2004).

The current paradigm in thoracic radiotherapy is to assume homogenous function throughout the lungs (Ireland *et al.*, 2016). However, lung cancer patients have been shown to have regional alterations in lung function, owing to other pulmonary co-morbidities (Papi *et al.*, 2004). Consequently, it is highly desirable to acquire regional measures of lung function to spatially assist in preferential sparing of functional lung during the treatment planning process. This 'functional avoidance treatment planning' concept has been applied to several functional imaging modalities including single photon emission computed tomography (SPECT) (Seppenwoolde *et al.*, 2000; Christian *et al.*, 2005), and Helium-3 magnetic resonance imaging (^{3}He MRI) (Ireland *et al.*, 2007a).

In addition to lung cancer, several respiratory diseases are characterised by impaired lung function on a regional basis. In particular, obstructive lung diseases such as asthma, COPD and cystic fibrosis exhibit marked increases in ventilation heterogeneity compared with normal subjects due to airway narrowing or closure. For asthmatics, the impact of therapeutic interventions such as bronchial thermoplasty may benefit from the quantitative information produced by ventilation from treatment planning to the assessment of regional pathophysiology response to treatment (Thomen *et al.*, 2015). For COPD patients, regional ventilation can help assess the impact of lung volume reduction surgery (Kurose *et al.*, 2004). For paediatrics with cystic fibrosis, an early detection of ventilation dysfunction may enable intervention prior to disease irreversibility (Thomen *et al.*, 2015). Thus, the ability to visualise and quantify regional lung ventilation is highly desirable. However, current regional ventilation modalities suffer from some or all of the following: poor spatial and

temporal resolution, requirement of contrast agent and specialised equipment inaccessible to most clinical radiotherapy centres.

Computed tomography (CT) images of the lungs are routinely utilised in the clinic for the radiological assessment of respiratory diseases and radiotherapy treatment planning. Over the past decade, CT-based surrogates of regional ventilation, sometimes referred to as 'ventilation CT', which are derived from pulmonary CT images acquired at different inflation levels without added contrast have been proposed as an alternative to clinically established lung function modalities (Guerrero *et al.*, 2005; Guerrero *et al.*, 2006; Reinhardt *et al.*, 2008; Fuld *et al.*, 2008; Ding *et al.*, 2012; Aliverti *et al.*, 2013). However, prior to widespread clinical use, the physiological accuracy must be validated to provide confidence that the computed image is a true reflection of regional ventilation.

1.2 Theory

Calculation of ventilation CT is a three step process. Firstly, CT images are acquired either at multiple breath-holds at different respiratory states (most commonly inspiration and expiration) or during tidal breathing via respiratory correlated 4DCT. Secondly, a deformation field is created, which spatially maps one of the acquired images (e.g. inspiration) to another (e.g. expiration) through non-rigid image registration. Finally, a ventilation metric is either computed directly on the deformation field by quantifying the local volume change or on the aligned images by quantifying intensity change on a voxel by voxel basis.

1.2.1 Intensity metric

Several methods have been proposed to compute the ventilation image, the most prevalent being the intensity (Guerrero *et al.*, 2005; Guerrero *et al.*, 2006; Fuld *et al.*, 2008; Castillo *et al.*, 2010) and Jacobian (Reinhardt *et al.*, 2008; Ding *et al.*, 2012) based metrics. The intensity based metric originates from theory proposed by Simon (2000). Guerrero first used it to derive a ventilation metric for breath-hold CT images registered non-rigidly using an optical flow algorithm (Guerrero *et al.*, 2005). The underlying assumption of this theory is that the

fraction of air in a voxel located in a CT image with an associated Hounsfield unit (HU) is equal to:

$$F_{air} = -\frac{HU}{1000}$$

Any voxel in the lung parenchyma is comprised of both air and tissue, each with an associated HU (Simon, 2000). If it can be assumed that uniform air distribution exists in the volume and that the change in volume between respiratory phases is attributable to changes in air volume only as shown in Figure 1.1 (i.e. tissue is incompressible and there is no change in the volume of tissue between inspiration and expiration) (Simon, 2000), then the fractional volume change between inspiration and expiration can be given by (Guerrero *et al.*, 2005):

$$\frac{\Delta V}{V_{air}^{exp}} = \frac{F_{ins} - F_{exp}}{F_{exp}(1 - F_{ins})}$$

where ΔV is the local air volume change caused by inspiration, V_{air}^{exp} is the local air volume at expiration and F_{ins} and F_{exp} are the voxel fraction of air in the inspiration and expiration images, respectively. This measure is assumed to be a surrogate for specific ventilation which is defined as the ratio of fresh gas (including oxygen) volume delivered to the alveoli following inspiration over the expiratory volume (Simon, 2005; Simon *et al.*, 2012) and can be calculated directly from the aligned inspiration and expiration CT images by the following equation (Guerrero *et al.*, 2005; Guerrero *et al.*, 2006; Fuld *et al.*, 2008; Castillo *et al.*, 2010):

$$\frac{\Delta V}{V_{air}^{exp}} = 1000\,\frac{\overline{HU}_{ins} - HU_{exp}}{HU_{exp}(1000 + \overline{HU}_{ins})}$$

where $\overline{HU}_{ins}$ is the interpolated HU value of the voxels in the deformed inspiration image which spatially correspond to the voxel in the expiration image and HU_{exp} is the HU of the expiration voxel. The intensity metric is thus effectively a measure of change in fractional content of air per voxel between respiratory phases.

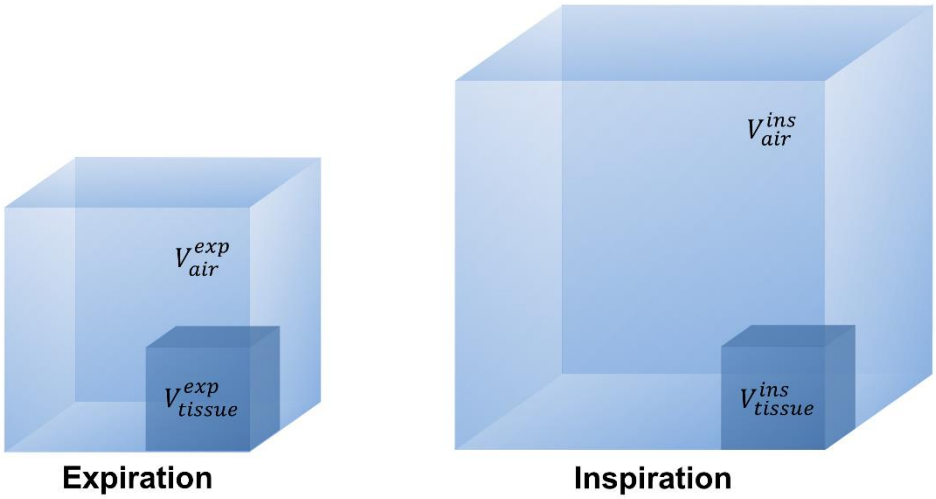

Figure 1.1 Example parenchymal region at expiration and inspiration demonstrating the fundamental assumption of the intensity metric in terms of constant tissue volume between inflation states.

1.2.2 Jacobian metric

An alternative metric, referred to as the Jacobian, is independent of the image intensity value. This was introduced to circumvent uncertainties introduced into the CT image by noise and reconstruction artefacts (Reinhardt *et al.*, 2008). This metric calculates local volume change between the two respiratory phase images by computing the Jacobian determinant (J) of the deformation field $h(x, y, z)$ as:

$$J\big(h(x,y,z)\big) = \begin{vmatrix} 1+\frac{\partial h_x(x,y,z)}{\partial x} & \frac{\partial h_x(x,y,z)}{\partial y} & \frac{\partial h_x(x,y,z)}{\partial z} \\ \frac{\partial h_y(x,y,z)}{\partial x} & 1+\frac{\partial h_y(x,y,z)}{\partial y} & \frac{\partial h_y(x,y,z)}{\partial z} \\ \frac{\partial h_z(x,y,z)}{\partial x} & \frac{\partial h_z(x,y,z)}{\partial y} & 1+\frac{\partial h_z(x,y,z)}{\partial z} \end{vmatrix}$$

The Jacobian determinant provides a measure of volume change such that a voxel value of one represents preservation of local volume while values less than and greater than one correspond to contraction and expansion of local volume, respectively. Values less than zero are indicative of singularities in the deformation field.

Strictly speaking, the Jacobian metric computes an image of regional volume change and is not equivalent to specific ventilation which is a direct physiological measure of the fractional volume of fresh gas delivered to the lung volume unit (Simon, 2005; Simon *et al.*, 2012). In addition, as shown in Figure 1.2, it is based on the assumption that no tissue volume exists in the inspiratory and expiratory images and volume changes are solely due to the change in air volume (Reinhardt *et al.*, 2008; Ding *et al.*, 2012).

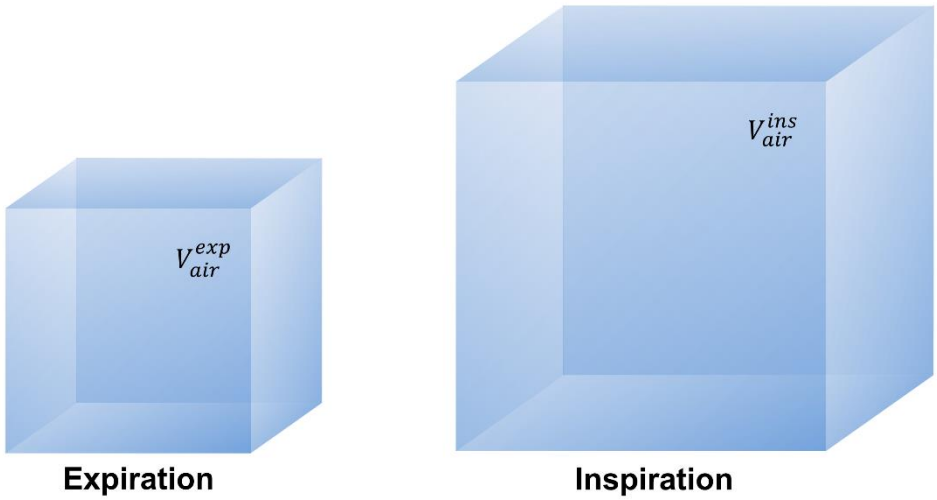

Figure 1.2 Example parenchymal region at expiration and inspiration demonstrating the fundamental assumption of the Jacobian metric in terms of zero tissue volume between inflation states.

1.2.3 Specific gas volume

A recent metric to be proposed is based on inflation-induced changes in specific gas volume (Aliverti *et al.*, 2013). As with the intensity metric, this metric computes surrogates of ventilation from CT density differences between aligned inhale and exhale images. It differs, however, in the way that it models ventilation. Specific gas volume (SGV) was initially proposed by Coxson *et al.* (1995) and is defined in units of millilitres of gas volume per gram of tissue (ml/g). It is calculated for each inhalation level via the following equation:

$$SGV = specific\ volume_{gas\&tissue} - specific\ volume_{tissue}$$

The specific volume of tissue is assumed to be constant, regardless of inflation level, and is equivalent to 0.94 ml/g (Hogg and Nepszy, 1969). The specific volume of gas and tissue is computed directly from thoracic CT images as follows:

$$specific\ volume_{gas\&tissue} = \frac{1024}{HU+1024}$$

1.2.4 Other metrics

A number of other metrics to model ventilation have also been proposed. These include a geometric method first proposed by Zhang *et al* (2010) which computes volume change by partitioning cubic voxels into six independent tetrahedrons defined by the positions of eight voxel vertices at expiration which are deformed at inspiration (Zhang *et al.*, 2010; Zhang *et al.*, 2011). The volumetric sum of these tetrahedrons yields the surrogate of specific ventilation (Zhang *et al.*, 2010; Castillo *et al.*, 2010; Zhang *et al.*, 2011). Ding *et al* (2012) have devised a hybrid metric comprising of both intensity and Jacobian based metrics, which purports to account for both air and tissue volume changes. Recently, Kipritidis *et al.* (2016) proposed the 4D-CT time averaged regional product of air and tissue densities as a surrogate of ventilation.

1.2.5 Discussion

The metrics computed on the raw HU values are susceptible to registration errors and CT noise at the voxel level. In order to account for these uncertainties, a common post-processing approach in the literature is to filter the images (Guerrero *et al.*, 2005; Castillo *et al.*, 2010), thus providing a smoothed local measure of ventilation with some loss of data complexity. Filtering has been shown to significantly increase the correlation of the ventilation images against more established modalities (Kipritidis *et al.*, 2014).

Although metrics computed directly on the deformation field such as the Jacobian metric are independent of CT noise and thus only affected by registration error (Du *et al.*, 2012), their numerical stability has been questioned; small variations in deformation fields with similar registration accuracies have been shown to lead to significantly larger changes in the underlying distributions of the computed ventilation images (Castillo *et al.*, 2017).

The fundamental assumption inherent in most ventilation metrics is that changes in lung density and volume between inflation levels are due solely to the influx of air whilst regional tissue and blood volume remain constant (Ding *et al.*, 2012). Previous 4DCT work has shown lung mass to vary cyclically with respiratory phase, perhaps due to the distention of the vasculature and inflation related differences in cardiac output (Guerrero *et al.*, 2006). More recent investigations with dual energy CT has confirmed that the regional distribution of pulmonary blood volume is sensitive to inflation level with marked variations observed in dependant and non-dependant regions (Fuld *et al.*, 2013). The hybrid metric purports to account for the effects of inflation-induced regional perfusion variations. However, as it is based on both the intensity and Jacobian metrics, it suffers from the aforementioned limitations of both metrics.

1.3 Validation

In order for lung ventilation CT to be used in the clinic, its physiological accuracy must be validated against established clinical imaging modalities. This includes determining the best ventilation metric and the most robust non-rigid registration algorithm. Initial studies were limited to global measures (Guerrero *et al.*, 2005; Guerrero *et al.*, 2006). Currently, there is a growing body of literature evaluating the technique with comparisons against assumed ground truth or gold standard ventilation imaging modalities such as nuclear medicine imaging, hyperpolarised gas MRI and Xenon (Xe)-CT. This section reviews the studies relating to each validation technique and identifies limitations and gaps in the literature. **Table 1.1** summarises previous studies validating ventilation CT against other pulmonary functional imaging modalities.

1.3.1 Comparisons with global measures

Early studies were limited to validation of the ventilation information by a self-consistency check involving the comparison of segmented lung from the ventilation images with the tidal volumes calculated from the difference between the segmented lung masks at inspiration and expiration (Guerrero *et al.*, 2005; Guerrero *et al.*, 2006; Castillo *et al.*, 2010). Guerrero *et al* (2005) compared breath-hold CT ventilation volumes derived from the intensity metric with CT measured tidal volumes and demonstrated high correlation via linear regression (R^2 = 0.985). A similar result was shown for 4D-CT ventilation with R^2 = 0.984. Castillo *et al* (2010) compared left and right lung tidal volumes with ventilation volumes derived from three metrics: intensity, Jacobian and geometric. They demonstrated high correlation with R^2 values of 0.99, 0.94 and 0.94, respectively.

Yamamoto *et al* (2011a) evaluated the effect of thresholding on the tidal volume comparison method. Lung ventilation contours derived from either the intensity and Jacobian based metrics were segmented and compared against CT tidal volumes with a threshold at -250 HU and -600 HU. They showed that the -600 HU threshold method yielded higher correlation values, suggesting that the

higher contrast features such as small vessels in the -250 threshold mask could have led to inaccuracies in the HU values (Yamamoto *et al.*, 2011a).

Ventilation CT images have also been validated against global measures of emphysema. Yamamato *et al* (2011a) investigated the correlation of 4D-CT derived ventilation for 12 patients with emphysema. Their hypothesis was that as lung regions not affected by emphysema are significantly more ventilated than emphysematous regions, 4D-CT ventilation would demonstrate higher ventilation in non-emphysematous regions. They tested this hypothesis for ventilation derived from the intensity and Jacobian metrics. Voxels with HU values lower than -910 were identified as emphysematous. Statistically significant differences were demonstrated only for the intensity based metric, indicating that it could be a better surrogate of ventilation than the Jacobian metric.

Comparing CT ventilation-derived metrics such as defective lung volumes and coefficients of variation with global measurements of spirometry, moderate correlations between FEV_1 and FEV/FVC, ranging from 0.43 to 0.73 (n = 15) and 0.38 (n = 98) to 0.73 for the intensity and Jacobian metrics have been reported, respectively, in lung cancer (Brennan *et al.*, 2015; Yamamoto *et al.*, 2014).

Given the regional nature of ventilation heterogeneity, the major limitation of these studies is that they only provide global measures of comparison and do not physiologically validate the local ventilation information against clinically established imaging techniques.

Table 1.1 Summary of previous studies validating CT-based surrogates of ventilation against other imaging modalities. Average values are shown. Where multiple metrics were studied, the value for the highest performing metric is quoted.

Study	Reference Modality	Subjects	Time interval between CT and reference	CT breathing manoeuvre	Reference breathing manoeuvre	CT ventilation metric	Comparison method	Key finding(s)
Nuclear Medicine imaging studies:								
Castillo et al. 2010	^{99m}Tc-DTPA SPECT ventilation	7 humans	Same day	4D-CT	Free breathing	Intensity and Jacobian	DSC of five percentiles bands, ranging from 0-20% up to 81-100%	Low DSCs with highest correlation for lowest percentile band (<0.4).
Yamamoto et al. 2010	^{99m}Tc-DTPA/^{99m}Tc-MAA SPECT ventilation/perfusion	1 human	Same day	4D-CT	Free breathing	Intensity and Jacobian	Voxel-wise SCC	Low/moderate SCCs for V/Q (0.18/0.48)
De Backer et al. 2010	^{99m}Tc-DTPA SPECT ventilation	6 humans	≤ 24 hours	Breath-hold (FRC and TLC)	Free breathing	Lobar expansion	Absolutes differences in percent lobar ventilation	Low differences (2.1%)
Castillo et al. 2012	^{99m}Tc-MAA SPECT perfusion	10 humans	One week	4D-CT	Free breathing	Intensity	DSC of defect regions	High DSCs (0.78)
Yamamoto et al. 2014	^{99m}Tc-DTPA SPECT ventilation	16 humans	9 days	4D-CT	Free breathing	Intensity and Jacobian	DSC of defect regions	Low DSCs (0.39)
Vinogradskiy et al. 2014	^{99m}Tc-DTPA planar ventilation	15 humans	≤ 62 days	4D-CT	Free breathing	Intensity	Correlation of percent ventilation in each lung and lung third.	Good and moderate correlation for each lung (0.65) and lung third (0.45), respectively.
Kipritidis et al. 2014	^{68}Ga-aerosol PET ventilation	12 humans	Same session	4D-CT	Free breathing	Intensity and Jacobian	Voxel-wise SCC and DSC	Moderate SCC (0.42); moderate and strong DSCs for low function (0.52) and good

								function (0.88) regions, respectively
Eslick et al. 2015	^{68}Ga-aerosol PET ventilation	11 humans	Same session	Breath-hold (End-expiration and inhalation)	Free breathing	Intensity	Correlation for percent lobar ventilation	Excellent correlation (0.96)
Kipritidis et al. 2016	^{68}Ga-aerosol PET ventilation	65 humans (25 pre-RT, 22 mid-RT and 18 post-RT)	Same session	4D-CT	Free breathing	Intensity, Jacobian and time averaged regional product of air and tissue densities	Voxel-wise SCC	Moderate SCC (0.50)
Xenon CT studies:								
Fuld et al. 2008	Xe-CT specific ventilation	4 sheep	Same session	4D-CT	Mechanically ventilated	Intensity	Correlation for manually defined ROIs with varying size (average: 1.6 ml)	Increasing correlation for increasing ROI size (small: 0.59; medium: 0.71; large: 0.76)
Reinhardt et al. 2008	Xe-CT specific ventilation	5 sheep	Same session	4D-CT	Mechanically ventilated	Jacobian	Correlation for 4 mm thick ROIs	High correlation (0.73)
Ding et al. 2012	Xe-CT specific ventilation	4 sheep	Same session	4D-CT	Mechanically ventilated	Intensity, Jacobian and Hybrid	Correlation for 20×20×20 mm^3 ROIs	High correlation (0.82)
Zhang et al 2016	Xe-CT specific ventilation	4 sheep	Same session	4D-CT	Mechanically ventilated	Intensity, Jacobian and Geometric	Voxel-wise SCC and DSC	Moderate SCC (0.44) and DSC for lower 30% ventilated volumes (0.55)
MRI studies:								
Mathew et al. 2012	^{3}He MRI static ventilation	11 humans	1.5 weeks	4D-CT	Breath-hold (FRC+1L)	Intensity	DSC of ventilated volume of each individual lung	High DSCs (0.87)

Abbreviations: DTPA = diethylenetriamine-pentaacetic acid; MAA = macroaggregated albumin; DSC = dice similarity coefficient; SCC = Spearman correlation coefficient; ROI = region of interest; FRC = functional residual capacity; TLC = total lung capacity

1.3.2 Comparisons with nuclear medicine imaging

Nuclear medicine imaging is the most common method for imaging lung function. It employs radioactive tracers which are either inhaled or administered intravenously in order to image ventilation and perfusion, respectively. Common tracers for imaging ventilation include technetium-99m (^{99m}Tc) diethylenetriamine-pentaacetic acid (DTPA) and ^{133}Xe gas. Pulmonary perfusion is normally imaged by ^{99m}Tc macroaggregated albumin (MAA). Once in the body, the radioactive tracer emits gamma photons which can be detected by a gamma camera and can yield superimposed planar images of the distribution of the radiotracer by a technique referred to as planar scintigraphy. By acquiring images at multiple angles around the patient and subsequently performing image reconstruction, 3D images of lung function can be computed. The SPECT technique typically requires 10-30 minutes for a volumetric acquisition (Petersson *et al.*, 2007).

The first physiological validation against SPECT was demonstrated by Castillo *et al* (2010). They compared the spatial overlap of five percentage intervals of 20% up to 100% by the Dice similarity coefficient between 4D-CT ventilation derived from the intensity, Jacobian and geometric metrics with that of ^{99m}Tc DTPA SPECT ventilation imaging for seven patients. They found statistically significant differences in the coefficients in favour of the intensity metric over the Jacobian and geometric metrics, with the highest correlation observed in the lowest percentile band. However, the reported dice coefficients for each percentile were low (< 0.4), possibly due to the susceptibility of ^{99m}Tc DTPA to airway deposition artefacts.

In a methodological study of one patient, 4D-CT ventilation images derived from both intensity and Jacobian based metrics were compared with both SPECT ventilation and perfusion imaging, resulting in poor correlation coefficients of 0.030/0.357 and 0.184/0.479 for each metric, respectively (Yamamoto *et al.*, 2010). This was consistent with the findings of Castillo *et al* (2010) who also reported weak correlations. Surprisingly, the correlation of

SPECT perfusion was slightly higher despite the ventilation signal being compared. The higher correlation for perfusion could be attributable to the severe Chronic obstructive pulmonary disease (COPD) disease progression of the patient in the study. SPECT ventilation images scanned with ^{99m}Tc labelled DTPA commonly demonstrate false ventilation due to central airway deposition (Magnant *et al.*, 2006; Jogi *et al.*, 2010). It has also been suggested that technegas be used as an alternative to DTPA for this cohort of COPD patients (Jogi *et al.*, 2010).

Although the study had the advantage that images for both modalities were acquired on the same day, similar to Castillo *et al* (2010), there were some differences in the breathing manoeuvre and patient positioning. The SPECT scans were acquired during free breathing without respiratory training to improve patient breathing and reduce artefacts. This is in contrast to the 4D-CT acquisition which employed audio-visual biofeedback (Venkat *et al.*, 2008) to control breathing. Furthermore, the 4D-CT ventilation images were derived from the end-inspiration and end-expiration images only, while the SPECT images were averaged over many breathing cycles. An improvement to this methodology would be to compare 4D-CT ventilation accounting for all phases in the respiratory cycle (Yamamoto *et al.*, 2010) and in conjunction use breathing training to ensure similar breathing techniques for both image modalities.

Another limitation of the SPECT validation method relates to the inherent low resolution of SPECT images (around 10mm). The high resolution 4D-CT ventilation image has to be downsampled to match the SPECT resolution and thus loses local ventilation information. This provides a more regional ventilation comparison which would not validate the local ventilation represented by each voxel in the CT ventilation image. Perhaps the major limitation of this study is the limited clinical conclusions that can be drawn from it because there was only one patient in the cohort.

^{99m}Tc MAA SPECT perfusion has also been compared to 4D-CT ventilation derived from the intensity metric for ten patients with malignant airway stenosis

(Castillo *et al.*, 2012). Moderately high spatial coincidence was shown by the dice coefficient (mean DSC = 0.78) in non-functional regions distal to lesion obstruction (Castillo *et al.*, 2012). The spatial correspondence for five patients in their study is shown in Figure 1.3.

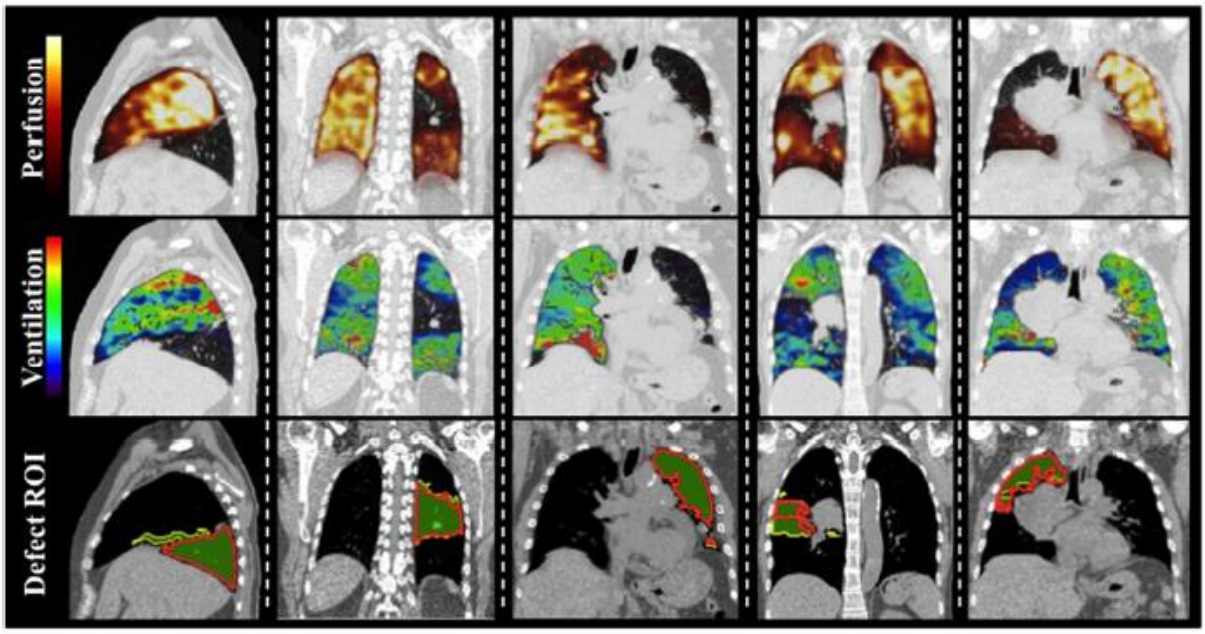

Figure 1.3. Comparison of SPECT perfusion (top row) with 4D-CT ventilation (middle row) for five patients with malignant airway disease. Reproduced with permission from Castillo et al. (2012).

From a methodological view, the major limitation of this study was the validation of the ventilation information against a non-ventilation perfusion measurement assumed to be ground truth. On the basis of the results of a recent study comparing SPECT ventilation and perfusion defects for 51 lung cancer patients (Yuan *et al.*, 2011), the study by Castillo *et al* (2012) assumes matched ventilation and perfusion defects for the cohort of patients in this study. However, Yuan *et al* (2011) showed 39% of patients in their cohort to have discrepancies between ventilation and perfusion, with 8% of patients with higher ventilation than perfusion and 31% showing the opposite. Their own conclusions are that perfusion is insufficient to provide a complete picture of lung function and additional information from ventilation is needed (Yuan *et al.*, 2011).

Another limitation of this study is that SPECT scans were acquired one week after the 4DCT scans (Castillo *et al.*, 2012). Although both were acquired prior

to treatment, thus ensuring that radiation induced changes did not affect the underlying ventilation distribution, some physiological changes may have occurred during the time interval between scans. A further drawback of this study and potential cause of error relates to the multi-modal image registration between the SPECT and 4DCT ventilation images. An affine registration was employed which does not account for the postural differences in imaged physiological states due to different breathing manoeuvres. Furthermore, registration validation only consisted of a visual inspection. An improvement would be to use a more objective validation method such as measuring Euclidean distances between anatomical landmarks.

Although regional lung function has traditionally been assessed by nuclear imaging, conventional planar and tomographic techniques suffer from poor accuracy, spatial and temporal resolution and aerosol depositions in defect regions (Petersson *et al.*, 2007). This may reduce correlation against ventilation CT. The efficacy of ventilation-based nuclear imaging can be improved by position emission tomography (PET) by inhalation of Gallium-68 (^{68}Ga) carbon nanoparticles, commonly referred to as Galligas, and has shown moderate vowel-wise correlations with 4D-CT (Kipritidis *et al.*, 2016; Kipritidis *et al.*, 2014). However, although the image data of these studies were acquired to enable improvements over ventilation CT versus SPECT studies with 4D-CT acquired at the same session and couch as PET, inherent discrepancies in image acquisition settings still remained. In general, the PET Galligas ventilation images in those studies were acquired over a minimum time scale of 10 minutes to ensure sufficient accumulation of the tracer, increasing for poor inhalations or low administered doses (Callahan *et al.*, 2014). By contrast, 4D-CT is acquired over a single tidal breath. Such differences may reduce spatial correlations between the two modalities.

Given the uncertainties in the HU values due to image noise and registration errors, some investigators have compared CT-based ventilation models with nuclear medicine imaging at the lobar level. In previous work by De Backer *et al.* (2010), a CT model of ventilation computed from two breath-hold CT scans based on the volume expansion between lobes was compared to SPECT lobar

ventilation in a cohort of 6 mild asthmatic patients. As this ventilation model utilized lobar segmentations only, it has the advantage of being independent of image registration. More recently, Eslick *et al.* (2016) compared ventilation derived from the intensity metric with PET Galligas for 11 lung cancer surgical resection candidates. Both studies have observed high correlations, indicating that correlation may be improved at courser levels. However, the same aforementioned limitations in comparisons with nuclear imaging apply.

1.3.3 Comparisons with Xe-CT

Ventilation can also be imaged and quantified by Xenon-enhanced CT (Xe-CT). This techniques employs radio-dense Xe gas as an inhaled contrast agent to increase the HU values of the pulmonary airspaces. The rate of gas wash-in and wash-out can be estimated from serial Xe-CT images, providing a direct and quantifiable measure of regional specific ventilation (Simon *et al.*, 2012).

Several studies have validated non-contrast CT surrogates of ventilation against Xe-CT specific ventilation. The first published study compared ventilation CT derived by the Jacobian method in 4 mm thick regions equally spaced along the ventral–dorsal direction for the lungs of five healthy sheep at constant pressure (Reinhardt *et al.*, 2008). Using linear regression, moderately high correlation (mean $R^2 = 0.73$) was demonstrated.

In a follow-up study, intensity, Jacobian and hybrid Jacobian metrics of ventilation were compared with Xe-CT ventilation for four sheep (Ding *et al.*, 2012). Using linear regression, spatial correspondence was evaluated for 20×20×20 mm^3 cubes with average correlation coefficients of $R^2 = 0.58$, $R^2 = 0.75$ and $R^2 = 0.82$ demonstrated for each measure, respectively. Statistically significant differences between the hybrid and intensity measure were observed for all animals in the study. Figure 1.4 shows the comparison for a sheep claimed to be representative of their study cohort.

Ding *et al* (2012) also evaluated the spatial correspondence for 150×8×40 mm^3 regions of interests and demonstrated higher correlation for intensity (R^2 = 0.87), Jacobian (R^2 = 0.88) and hybrid metrics (R^2 = 0.92). Furthermore, statistically significant differences between the metrics were not demonstrated for most animals for the larger 150 × 8 × 40 mm^3 regions of interests, suggesting that local and regional evaluation is preferred over global measures for improved assessment of the best ventilation metric (Ding *et al.*, 2012). Both studies (Reinhardt *et al.*, 2008; Ding *et al.*, 2012) reported limited clinical findings due to the small cohort and the use of non-human subjects. More recently, Zhang *et al.* (2016) employed the same dataset and performed voxel-wise correlations for the intensity, Jacobian and geometric metrics. Moderate Spearman correlations were observed of 0.44.

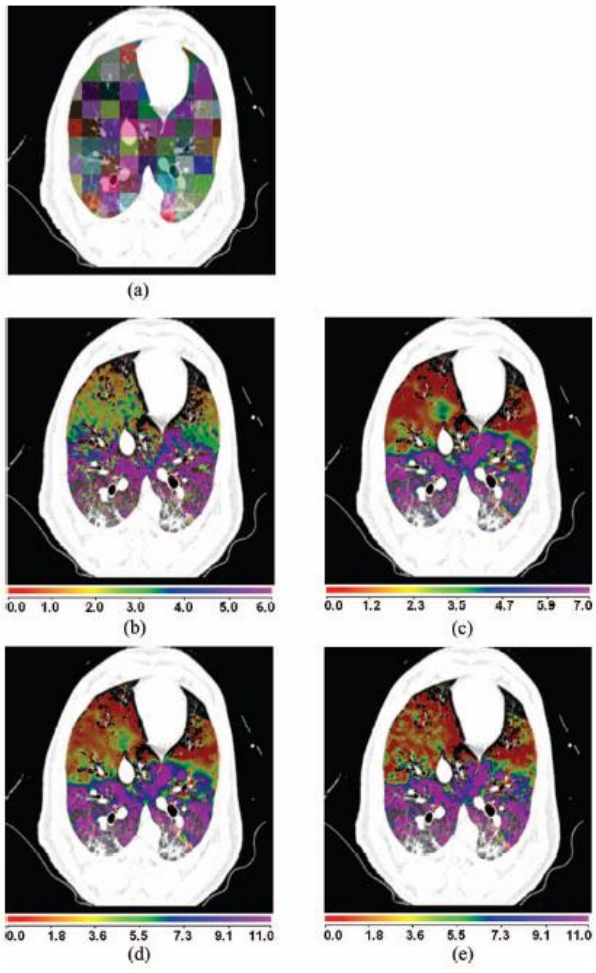

Figure 1.4. Example sheep comparison of (b) Xe-CT ventilation with 4D-CT ventilation derived from (c) Jacobian, (d) hybrid and (e) intensity based metrics. (a) Colour coded cubes representing regions of interests. Reproduced with permission from Ding *et al.* (2012).

Although Xe-CT is considered to be the gold standard in ventilation imaging and provides superior resolution to other modalities, due to the requirement of high temporal resolution, it suffers from limited axial coverage of up to 3 cm (Reinhardt *et al.*, 2008), thus not allowing for volumetric validation of the complete ventilation CT image. This also poses significant challenges on performing viable spatial correlations, owing to the difficulties in accurately registering the selected Xe-CT slabs to the volumetric CT images.

1.3.4 Comparisons with hyperpolarised gas MRI

Conventional MRI provides images of the hydrogen protons in water molecules. However, it suffers from a number of drawbacks for the lungs. These include the low proton density in the lungs, millions of air-tissue interfaces which gives rise to magnetic susceptibility artefacts and negligible signal from the airspaces. These limitations can be overcome by performing MRI by inhaling discreet volumes of magnetised noble gases such as Helium-3 (^{3}He) or Xenon-129 (^{129}Xe). The technique provides high resolution maps of the gas distribution in the pulmonary airspaces. Regions of hyposignal are indicative of ventilation defects (van Beek *et al.*, 2004).

Previously, Mathew *et al* (2012) evaluated the spatial correspondence of 4D-CT ventilation derived from the intensity based metric with ^{3}He MRI for eleven lung cancer patients. Using the dice similarity coefficient, they demonstrated a high degree of spatial overlap for both ipsilateral (86 ± 12%) and contralateral lung (88 ± 12%). Figure 1.5 shows their comparison for a patient in their study, indicating high ipsilateral spatial correlation with discrepancies in contralateral lung.

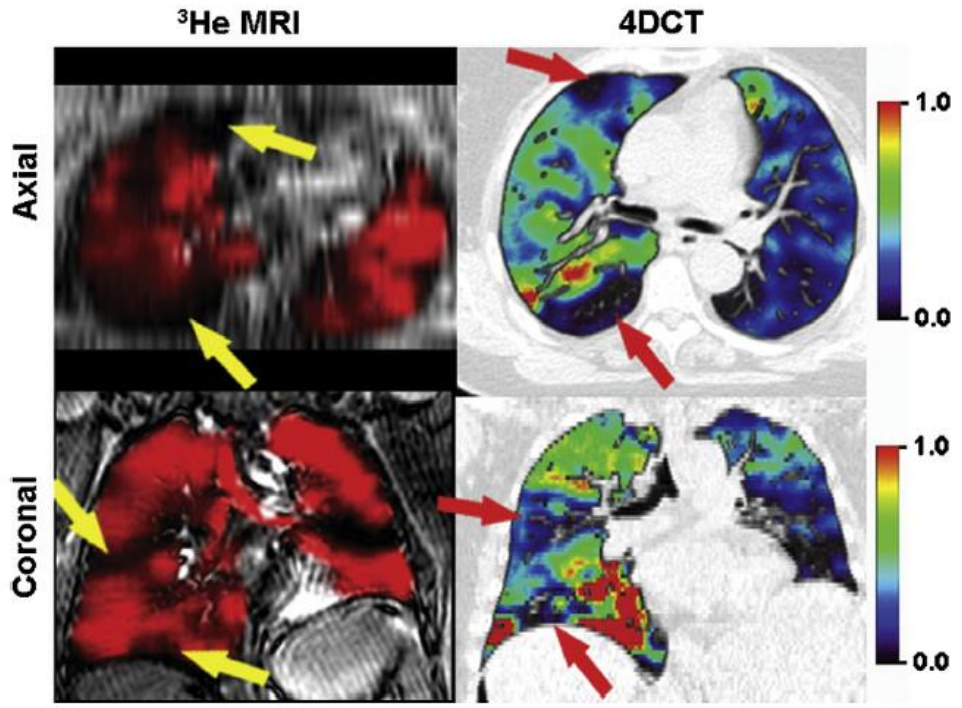

Figure 1.5. Comparison of 4D-CT ventilation with ^{3}He MRI ventilation. Arrows indicate matching ventilation defects. Reproduced with permission from Mathew *et al.* (2012).

However, this work had several methodological limitations. Firstly, the image acquisition protocol was not optimised to minimise potential discrepancies between the two modalities; the two different scans were acquired at a mean interval of 1.5 weeks for each patient and thus some of the regional ventilation differences in their study could be attributable to disease progression and time-related physiological differences. Furthermore, differences in patient positioning (treatment planning couch vs diagnostic MRI couch) and breathing manoeuvre (inspiratory breath-hold vs tidal breathing) were not explicitly accounted for, potentially leading to differences in the imaged physiologic states and registration errors. Ireland *et al.* (2008) demonstrated significant improvements in rigid registration by reproducing the same breath-hold and body positions during image acquisition of CT and ^{3}He MRI. Secondly, only fiducial anatomical landmark affine registration was used to ensure the CT ventilation and HP gas images were in the same spatial domain without accounting for deformable differences between the two images, owing to postural differences. Thirdly, only ventilation derived from an intensity metric was evaluated in this study with no reference to other prominent metrics such

as the Jacobian metric. Fourthly, the assessment of spatial correlation was limited to comparing the spatial overlap of binary thresholded images from both modalities by the dice overlap coefficient. Such overlap measures provide a more global comparison and thus voxel-wise and region of interest analysis may improve the comparison by assessing the correlation of the intensity distribution of corresponding regions within the binary segmentations.

An alternative gas to ^{3}He for hyperpolarised gas MRI is ^{129}Xe. ^{129}Xe has begun to play a more important role in recent years, owing to global depletions in ^{3}He (Patz *et al.*, 2007). ^{129}Xe MRI exhibits some differences in ventilation distributions compared with ^{3}He MRI (Svenningsen *et al.*, 2013; Kirby *et al.*, 2013) and it would thus be of relevance to the research community to study how it correlates with CT-based surrogates of ventilation.

1.3.5 Reproducibility

Reproducibility of ventilation CT derived from 4D-CT images has been investigated by Du *et al.* (2012) and Yamamoto *et al.* (2012). In the former, the intra-session ventilation reproducibility of two consecutive 4D-CT scans was investigated for three sheep and nine patients (Du *et al.*, 2012). The scans were acquired within 10 minutes of each other. The ventilation metric used was the Jacobian based metric and the spatial correspondence between scans was compared by computing the average voxel by voxel ratio of the Jacobian ventilation images. Although strong correlations were shown for the sheep cohort, the human cohort demonstrated moderately weak correlations. This could be due to the fact that the sheep were mechanically ventilated while under anaesthesia without being moved during image acquisition while the humans breathed via audio coaching (Du *et al.*, 2012).

The results demonstrated for the human cohort in Du *et al* (2012) are in agreement with those of Yamamoto *et al* (2012) who evaluated the reproducibility for both intra- and inter-session 4D-CT image acquisition. For the intra-session patients, 4D-CT image acquisition was repeated for six lung cancer patients with a five-minute interval. The inter-session cohort consisted

of another six patients imaged by 4D-CT repeated at an interval of fifteen days. Using the Spearman voxel based correlation coefficient, where a value of 1 indicates perfect spatial correlation (Zou *et al.*, 2003), they demonstrated only moderate correlations with coefficients of 0.53 ± 0.20 and 0.48 ± 0.11 for intra- and inter-session scans, respectively (Yamamoto *et al.*, 2012). Figure 1.6 shows a comparison between scans for the weakest correlated inter-session patient in the study.

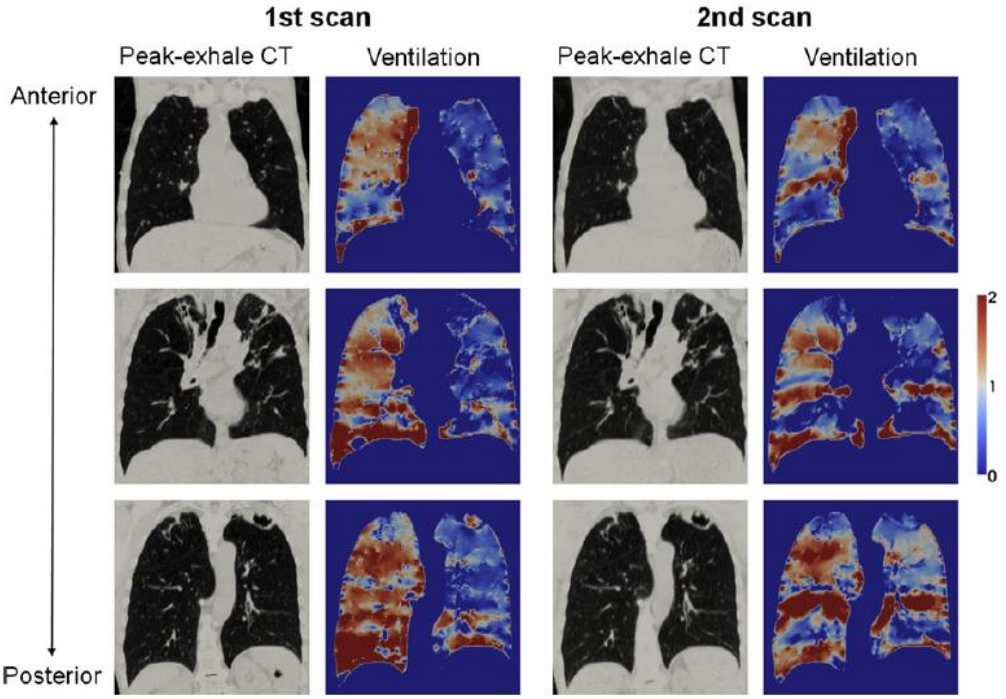

Figure 1.6. Comparison of baseline scan with follow-up for an inter-session patient with weakest spatial correlation (Spearman coefficient = 0.36) in study. Reproduced with permission from Yamamoto *et al.* (2012).

They suggest several factors which could have caused the ventilation discrepancies between scans. One factor is the possible presence of artefacts in the 4D-CT images which has been shown to affect 90% of scans (Yamamoto *et al.*, 2008). Another factor relates to the degree of respiratory variation between scans. Recently, Mistry *et al.* (2013) evaluated the effects of different breathing manoeuvres during CT imaging and observed marked differences in the distribution of the computed CT ventilation images. Gated

image acquisition and breathing training could improve the reproducibility of the tidal breathing procedure (Yamamoto *et al.*, 2012).

The inferior reproducibility for the inter-session cohort could be due to several factors including differences in patient positioning and underlying physiological changes occurring during the fifteen day interval (Yamamoto *et al.*, 2012). In fact, a drawback of this study was that the repeat scans were acquired with different arm positions (arms down vs. up). Differences in ventilation and respiratory measures have been shown to be sensitive to arm position (Couser *et al.*, 1992). An improved follow-up study would thus ensure the same imaging protocol be used for repeat scans.

To date, only 4D-CT ventilation reproducibility has been investigated in the literature. However, no published work exists evaluating the reproducibility of breath-hold CT ventilation. Such a study would be of clinical relevance to the radiotherapy community as breath-holds are integrated in several motion mitigation strategies, aimed at reducing safety margins.

1.4 Innovation and scientific contribution

Prior to clinical use, the physiological accuracy of ventilation CT needs to be established. A growing body of literature devoted to validation of the technique is emerging. Whilst preliminary studies were limited to global validations, more recent work has shown an increased interest in regional validations against pulmonary functional imaging modalities. Although considerable efforts have been made towards this goal, previous studies suffer from a number of methodological limitations which may have led to an erroneous evaluation of the technique's physiological accuracy. These include discrepancies in acquisition settings between scans such as different breathing manoeuvres, prolonged time intervals, limited volumetric coverage of the reference modality, inaccurate registration of CT and the reference modality and unsophisticated methods of comparison. Several metrics may be used to compute the ventilation signal. Intensity and Jacobian based methods have gained particular interest in the literature. Several of the recent validation

studies have directly compared the ventilation signals derived from these metrics with available imaging modalities. However, conflicting results are reported and it is not clear which, if any, of the metrics is a suitable surrogate for pulmonary ventilation. A concerted effort, therefore, is warranted to develop and evaluate methods to address these limitations.

1.5 Thesis aims and objectives

The overall study aim of this thesis is to address the hypothesis that:

Surrogates of regional ventilation derived from inhale and exhale CT data can provide information comparable to a direct measure of ventilation from hyperpolarised gas MRI ventilation.

In order to investigate this hypothesis, the following specific objectives have been set out:

1. To develop a methodology for registering CT and hyperpolarised gas MRI.
2. To compare CT-based surrogates of ventilation with hyperpolarised gas MRI at the lobar level.
3. To evaluate the impact of inflation levels when comparing gas MRI and ventilation CT.
4. To develop a novel image acquisition and analysis framework to facilitate regional and voxel level correlations of CT-based surrogates of ventilation with hyperpolarised gas MRI.
5. Investigate the effect of using different hyperpolarised noble gases on the correlation of gas MRI and ventilation CT.

1.6 Thesis organisation

This chapter has reviewed the underlying theory and validation of CT-based surrogates of ventilation. Chapters 2 to 5 each constitute self-contained studies, comprising of an abstract, formal introduction, methods, results, discussion and conclusion. These chapters detail the work undertaken to address each of the aforementioned specific objectives defined to test the overall hypothesis of the thesis. Specifically, the thesis is organised as follows:

- **Chapter 2** addresses the first specific objective, where a novel method of registering hyperpolarised gas MRI to CT utilising ^{1}H-structural MR images that are acquired in the same breath-hold as the gas MRI is described.
- **Chapter 3** addresses the second specific objective, detailing the methods developed and tested to compare lobar lung ventilation, computed from expiratory and inspiratory CT segmentations with that of hyperpolarised gas MRI.
- The third specific objective is addressed in **Chapter 4**, in which the spatial overlap of CT based ventilation is compared to hyperpolarised gas MRI acquired at two different inflation levels.
- **Chapter 5** addresses the fourth specific objective by describing a novel framework for facilitating spatial correlation of ventilation CT and hyperpolarised gas MRI. The fifth specific objective is also addressed in this chapter by evaluating the effect of using two different noble gases, namely, ^{3}He and ^{129}Xe, on the spatial correlation.[1]
- **Chapter 6** includes a summary of the research, potential clinical applications, limitations and future research directions.
- Finally, **Chapter 7** is the Appendix, where the results of the inspiratory and expiratory breath-hold CT registration validation experiments are presented and the publications resulting from this thesis thus far are summarised.

[1] Chapters 2 to 4 retrospectively analyse a CT and MR asthma dataset generously provided by the AIrPROM (Airway Disease Predicting Outcomes through Patient Specific Computational Modelling) consortium. Chapter 5 investigates a lung cancer radiotherapy dataset, the protocol of which the author was directly involved in.

Chapter 2
A method for quantitative analysis of regional lung ventilation using deformable image registration of CT and hybrid hyperpolarised gas/^{1}H MRI

Background: Hyperpolarised gas MRI generates highly detailed maps of lung ventilation and physiological function while CT provides corresponding anatomical and structural information. Fusion of such complementary images enables quantitative analysis of pulmonary structure-function. However, direct image registration of hyperpolarised gas MRI to CT is problematic, particularly in lungs whose boundaries are difficult to delineate due to ventilation heterogeneity.
Purpose: This study presents a novel indirect method of registering hyperpolarised gas MRI to CT utilizing ^{1}H-structural MR images that are acquired in the same breath-hold as the gas MRI. The feasibility of using this technique for regional quantification of ventilation of specific pulmonary structures is demonstrated for the lobes.
Methods: The direct and indirect methods of hyperpolarised gas MRI to CT image registration were compared using lung images from 15 asthma patients. Rigid, affine and diffeomorphic[2] image transformations were implemented. Registration accuracy was evaluated using the target registration error (TRE) of anatomical landmarks identified on ^{1}H MRI and CT. The Wilcoxon signed-rank test was used to test statistical significance.
Results: For the rigid transformation, there was no statistically significant difference between the direct and indirect methods (TRE=17.4±3.9mm vs. 17.2±3.3mm, p=0.570). For the affine transformation, the indirect method of image registration was significantly more accurate than the direct method (TRE=14.7±3.2 vs. 19.6±12.7mm, p=0.036). Using a deformable transformation, the indirect method was also more accurate than the direct method (TRE=13.5±3.3 vs. 20.4±12.8mm, p=0.006).

[2] It is noted that rigid and affine transforms fall in the class of diffeomorphisms in the sense that they constitute differentiable maps with differentiable inverses. However, for brevity, throughout this thesis, the term ‘diffeomorphic’ is used to describe non-affine (deformable) transforms.

Conclusion: Accurate image registration is critical for quantification of regional lung ventilation with hyperpolarised gas MRI within the anatomy delineated by CT. Automatic deformable image registration of hyperpolarised gas MRI to CT via same breath-hold ^{1}H MRI is more accurate than direct registration. Potential applications include improved multi-modality image fusion, functionally-weighted radiotherapy planning, and quantification of lobar ventilation in obstructive airways disease.

2.1 Preface

The majority of the material in this chapter was originally published as a full length article in the journal *Physics in Medicine and Biology*:

> Tahir BA, Swift A, Marshall H, Parra-Robles J, Hatton MQ, Hartley R, Kay R, Brightling CE, Vos W, Wild JM, Ireland RH (2014). A method for quantitative analysis of regional lung ventilation using deformable image registration of CT and hybrid hyperpolarised gas/^{1}H MRI. Physics in Medicine and Biology, 59(23): 7267-77.

Additional material is presented here that could not be included in the published article.

The work has also been presented at the following conferences:

> Tahir BA, Swift AJ, Marshall H, Leung G, Hatton MQ, Hartley R, Kay R, Brightling CE, Wild JM and Ireland RH. Image registration accuracy of synchronously acquired ^{1}H and hyperpolarised ^{3}He MRI to X-ray CT for lung cancer treatment planning. UK Radiation Oncology Conference 2013, Nottingham, United Kingdom

> Tahir BA, Swift AJ, Marshall H, Leung G, Hatton MQ, Hartley R, Kay R, Brightling CE, Wild JM and Ireland RH. Target registration error of diffeomorphic image registration of same breath-hold ^{1}H and hyperpolarised ^{3}He MRI to lung CT for radiotherapy treatment planning. IPEM Medical Physics and Engineering Conference 2014, Glasgow, Scotland

2.2 Introduction

Computed tomography is the gold standard for high-resolution structural imaging of the lung but has limited functional sensitivity and soft tissue contrast. The quality of proton structural MRI of the lungs has improved in recent years through the use of MR sequences (Wild *et al.*, 2012) such as ultra-short echo time (Lederlin and Crémillieux, 2013) and balanced steady state free precession (Rajaram *et al.*, 2012) to the point where the scans have diagnostic utility in certain conditions. Hyperpolarised gas (^{3}He and ^{129}Xe) MRI provides highly detailed images of lung ventilation and regional pulmonary function with sensitivity to different aspects of pulmonary physiology and lung disease (Van Beek *et al.*, 2004; Fain *et al.*, 2010). Visualization and quantification of this functional data superimposed upon anatomical images may be advantageous in order to maximize the complementary information relating to form and function.

In practice, fused hyperpolarised gas and anatomical lung imaging could be achieved either by the application of image registration or same breath-hold data acquisition. While hyperpolarised gas and ^{1}H MRI is routinely performed in the same imaging session, coil and pulse sequence designs have only recently realized the capability for same breath-hold acquisition of hyperpolarised gas and ^{1}H lung MRI (Wild *et al.*, 2011; Wild *et al.*, 2013). Additionally, superior analytical interpretation and quantification is provided by registration of the hyperpolarised gas MRI not only to ^{1}H MRI but also to the more detailed images of lung structure provided by high-resolution x-ray CT. However, there is little prospect of a hardware solution for combined MR/CT imaging and as such an image registration solution is required.

Registration of hyperpolarised gas MRI and CT has been shown to facilitate functionally weighted radiotherapy treatment planning for lung cancer patients (Ireland *et al.*, 2007a) and enable comparison of CT and ^{3}He MRI measures of ventilation (Mathew *et al.*, 2012). Clinical investigations of other obstructive lung diseases, such as cystic fibrosis, asthma and emphysema (van Beek *et al.*, 2004), could also potentially benefit from the fusion of hyperpolarised gas

ventilation MRI with matched anatomical images. In addition, multimodality image fusion of hyperpolarised gas MRI and CT has the potential to facilitate quantification of ventilation for specific pulmonary structures such as the lobes which cannot be identified on hyperpolarised gas MR images (Tahir *et al.*, 2014a).

Preliminary work on hyperpolarised gas MRI to CT image registration demonstrated the feasibility of fusing the images semi-automatically using control point rigid registration (Ireland *et al.*, 2007a). Subsequently, an enhanced acquisition and registration protocol was reported (Ireland *et al.*, 2008). Although hyperpolarised gas MRI to CT registration accuracy was improved, the method still requires the input of operator landmarks that have an associated inter-observer variability. Ideally the registration would be performed fully automatically.

In this study, our first hypothesis is that as the ^{1}H MRI acquired in the same breath-hold as hyperpolarised gas MRI is independent of ventilation defects and structurally similar to the CT then it can facilitate automatic hyperpolarised gas MRI/CT image registration. This is analogous to the way CT images from PET/CT can be used as the intermediary for PET image registration (Ireland *et al.*, 2007b).

A secondary issue with registering hyperpolarised gas MRI to corresponding anatomical images is that quantitative evaluation of registration error is difficult (Ireland *et al.*, 2008), particularly if significant ventilation defects exist. A method that enables calculation of the target registration error (TRE) of corresponding expert defined anatomical landmarks (Murphy *et al.*, 2011) would be beneficial for assessing hyperpolarised gas MRI registration, especially for distinguishing between registration algorithms. Therefore, in this study, our second hypothesis is that inclusion of same breath-hold ^{1}H MRI can provide a method for quantifying the TRE for hyperpolarised gas MR image registration.

In this work, we evaluate the role of synchronously acquired ^{1}H MRI in facilitating automatic hyperpolarised gas MRI/CT image registration and quantitative TRE analysis of hyperpolarised gas MR image registration. This was investigated firstly by performing a ventilation defect simulation study to investigate the impact of defective ventilation and secondly by a cohort of 15 asthma patients to evaluate the impact of the registration methods in a real world situation. In so doing, we demonstrate the feasibility of regional quantification of hyperpolarised gas MR derived ventilation using the underlying lung anatomy from CT.

2.3 Methods

2.3.1 Image acquisition

The study was performed with national research ethics committee approval (ClinicalTials.gov: NCT01545726). Between February and November 2012, 15 asthma patients gave written informed consent to undergo both hyperpolarised ^{3}He MRI and CT during breath hold at functional residual capacity (FRC) + 1L and total lung capacity (TLC), respectively. ^{1}H MRI were acquired in the same breath hold as the ^{3}He MRI acquisition (Figure 2.1) (Wild *et al.*, 2011), on a GE HDx 1.5T MR scanner (GE Healthcare, Princeton, NJ, USA). Hyperpolarised ^{3}He and ^{1}H MR images were acquired coronally with in-plane resolutions of 3×3 mm^2 and 3×6 mm^2 and voxel matrices of 128×128×24 and 128×64×24, respectively, and slice thicknesses of 10 mm for both. CT was acquired axially on a Sensation 16 scanner (Siemens, Forchheim, Germany). The following CT settings were used: tube voltage, 120kV; tube current, 120mAs; rotation time, 0.5s; pitch, 1.5. Where available, a B30f reconstruction kernel was used or the next kernel closest to it (e.g. B35f, B60 etc.). CT in-plane resolution was approximately 0.86×0.86 mm^2 with a pixel matrix of 512×512. CT slice thickness was 1 mm with approximately 600 slices for each patient.

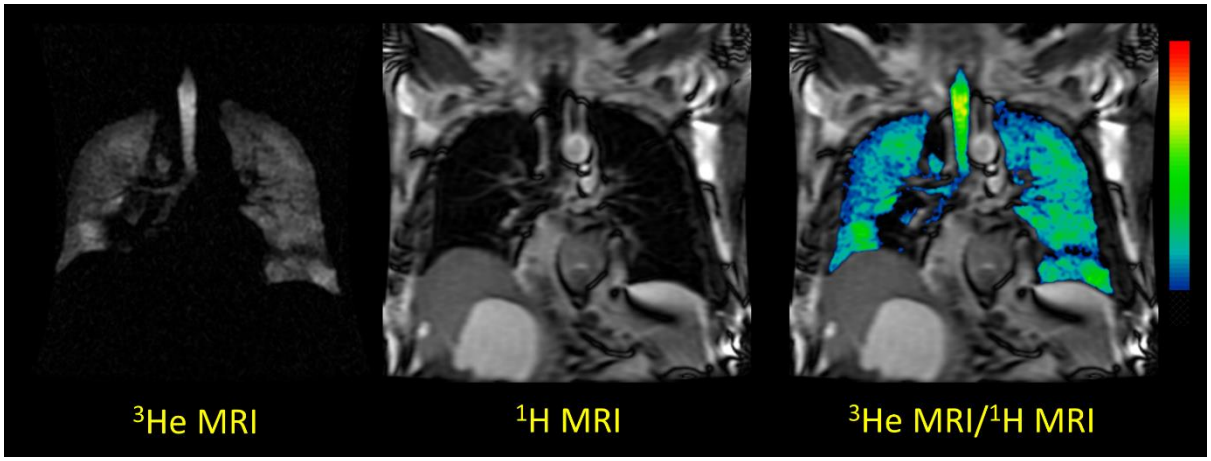

Figure 2.1 ^{3}He and ^{1}H MRI acquired during the same breath-hold for patient 2.

2.3.2 Image registration

Image registration was performed using the `antsRegistration` tool incorporated as part of the Advanced Normalization Tools (ANTs) (Avants *et al.*, 2011; Avants *et al.*, 2012). For each patient, the ^{3}He MRI and ^{1}H MRI (moving images) were registered to CT (fixed image) using three different transforms; rigid, affine and diffeomorphic. CT was resampled to a matrix size of 512×512×160 voxels to reduce the computational time in performing registrations.

A coarse pre-alignment rigid transform was applied to align the centers of mass of the CT and MR image intensities. The resulting transform was then applied to the affine stage. Due to the multimodal nature of the problem, the mutual information similarity metric was used with 32 histogram bins optimized via the gradient descent algorithm with a step size of 0.1. A multi-resolution Gaussian pyramid with 5 levels was used with down-sampling factors 8x6x4x2x1 and corresponding smoothing Gaussian sigmas of 4x3x2x1x0 mm. A maximum of 10,000 iterations were set for each resolution level to ensure convergence (Glocker *et al.*, 2011).

An additional diffeomorphic transformation that copes with large deformations while preserving topology of anatomical structures (Avants *et al.*, 2008) was also applied to the resulting transform of the affine pipeline with the same parameters for the multi-resolution Gaussian pyramid and similarity metric.

The Greedy Symmetric Normalization algorithm (SyN) provided by the ANTs registration suite was the chosen algorithm as it was the highest performing algorithm at a recent pulmonary image registration competition (Murphy *et al.*, 2011). A step size of 0.2 was selected for the gradient descent optimization algorithm.

To reduce the computational time in performing the registration, 16 cores via two Intel Xeon E5-2670 processors @ 2.60 GHz were run in parallel on a 64-bit high performance Linux server (Iceberg, University of Sheffield) using the multi-threading options available in Insight Toolkit version 4 (ITK, www.itk.org). Computational times for the full diffeomorphic pipeline ranged from 28 to 37 minutes, including the rigid pre-alignment and affine stages.

As the ^{1}H and ^{3}He MRI were acquired in the same breath-hold and spatially co-registered (Wild *et al.*, 2011), the same transform to map ^{1}H MRI to CT was applied to map ^{3}He MRI to CT with linear interpolation for the indirect registrations using the `antsApplyTransform` tool available in ANTs.

2.3.3 Ventilation defect simulation study

To investigate the impact of defective ventilation on ^{3}He to CT registration, image registration was performed on a series of simulated ventilation images generated from a patient image exhibiting homogenous ventilation. Segmentation software (Mimics; Materialise, Leuven, Belgium) was used to contour the lobes of the inspiratory CT data by identification of major fissures in both lungs. Lobar segmentations were reviewed by an expert radiologist and manually adjusted where segmentation errors were present. CT lobar binary masks were then warped to the spatial domain of the ^{3}He MRI by applying the inverse transform of a diffeomorphic registration. An example coronal slice is shown in Figure 2.2. Starting with the full set of lobes, the ^{3}He image was masked by successive lobar removal. This resulted in multiple combinations of segmented ^{3}He MRI:

1. Left lower Lobe (LLL)
2. Left upper lobe (LUL)
3. Right lower lobe (RLL)
4. Right upper and middle lobes (RUML)
5. LLL + LUL
6. RUML + RLL
7. LLL + LUL + RUML
8. RLL + RUML + LLL
9. RUML + RLL + LUL
10. LUL + LLL + RUML + RLL

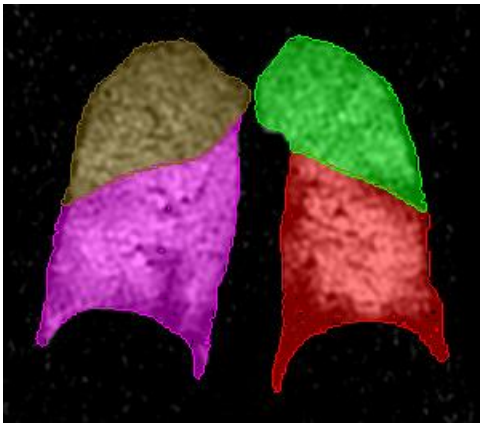

Figure 2.2 Coronal slice of registered CT lobes fused with ^{3}He MRI for the simulation study.

2.3.5 Asthma patient study

For each of the fifteen patients, the following six registration pipelines were performed to register ^{3}He MRI to CT either directly or indirectly (Figure 2.3) via the same breath-hold ^{1}H MR image:

1. Rigid direct — Rigid registration of ^{3}He MRI to CT
2. Rigid indirect — Rigid registration of ^{1}H MRI to CT
3. Affine direct — Affine registration of ^{3}He MRI to CT
4. Affine indirect — Affine registration of ^{1}H MRI to CT
5. Diffeomorphic direct — Diffeomorphic registration of ^{3}He MRI to CT
6. Diffeomorphic indirect — Diffeomorphic registration of ^{1}H MRI to CT.

For all the registration pipelines, only the transform (affine or diffeomorphic) and moving image (^{3}He MRI for direct and ^{1}H MRI for indirect) were varied.

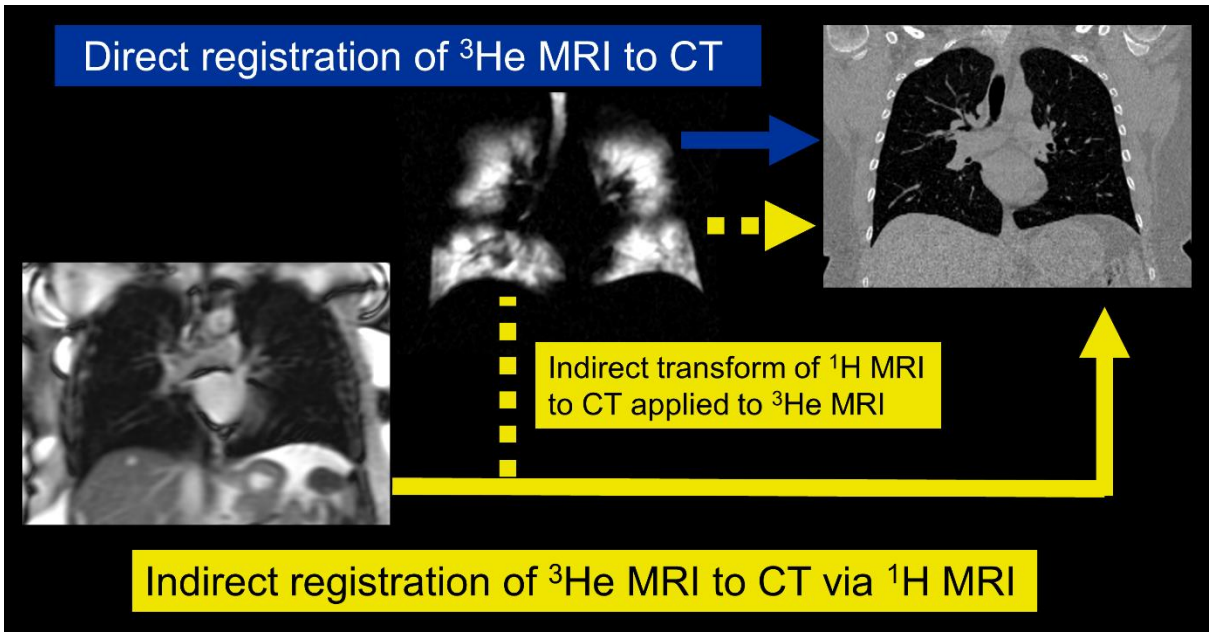

Figure 2.3 Workflow of direct and indirect registration methodology.

2.3.6 Registration evaluation

The registration accuracy of each registration pipeline for the simulation and patient studies was assessed quantitatively where pairs of anatomical landmarks were identified using Slicer 4 (Fedorov *et al.*, 2012), on the ^{1}H MR and CT images and then reviewed independently by a chest radiologist (Dr

Andy Swift). Landmark locations included the apex and base of the lungs, arch of the aorta and bifurcations of the trachea and blood vessels. The transformations derived from the direct ^{3}He MRI to CT and indirect ^{1}H MRI to CT registrations were applied to the landmark coordinates to enable the mean target registration error (TRE) of the corresponding landmarks to be calculated for all points. TRE is defined as the Euclidean distance between two corresponding points (Murphy *et al.*, 2011). Figure 2.4 shows an example of corresponding landmarks identified on ^{1}H MRI and CT, alongside the ^{3}He MRI that was acquired in the same breath hold as the ^{1}H MRI.

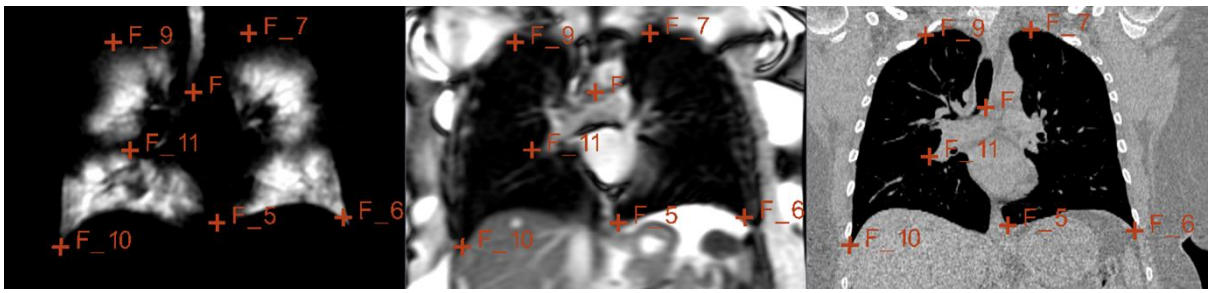

Figure 2.4 An example of corresponding landmarks identified on ^{1}H MRI (middle) and CT (right) images, alongside the ^{3}He MRI (left) that was acquired in the same breath hold as the ^{1}H MRI.

2.3.7 Statistics

The Wilcoxon signed-rank test implemented in IBM SPSS (version 20.0; Chicago, Il, USA) was used to test the statistical significance of the differences between the direct and indirect registration of ^{3}He MRI to CT. In addition, the TRE for the indirect diffeomorphic pipeline was compared to all other pipelines. A p value less than 0.05 was considered statistically significant.

2.3.8 Lobar segmentation and regional ventilation quantification

As an example to demonstrate the feasibility of quantification of ^{3}He MRI ventilation of pulmonary structures identifiable only on CT, the percentage ventilation per lobe was calculated by taking the ratio of ^{3}He MRI volume in a given lobe to the total ^{3}He MRI volume in the lungs. The CT lobes were segmented as described for the simulation study. These lobar segmentations were used to mask the registered ^{3}He MRI which were segmented via the Otsu

histogram based method which separates the foreground ventilated volume from signal void hypo-ventilated regions and background noise (Otsu, 1979).

2.4 Results

2.4.1 Ventilation defect simulation study

Table **2.1** displays the TRE results for the simulation study. An error > 50mm was generated for all the direct registration methods when the ^{3}He ventilated region was set to only one or two lobes. With improving ventilation, the error is reduced to the range 17.4 to 22.0mm, which, for this patient, is a comparable order of magnitude to the indirect method (range 16.0 to 18.7mm).

Table 2.1 Mean target registration errors (TRE) for the simulation study.

Single lobe	TRE (mm)
LLL	174.5
LUL	135.8
RLL	140.1
RUML	139.3
2 lobes (one lung)	
LLL+LUL	139.8
RUML+RLL	80.1
3 lobes	
LLL+LUL+RUML	23.4
RLL+RUML+LLL	21.5
RUML+RLL+LUL	28.1
4 lobes (both lungs)	
Full ^{3}He	20.7
Full ^{1}H (indirect)	18.7

2.4.2 Asthma patient study

A median of 31 anatomical landmarks per patient (range 22 to 42) were identified on both the ^{1}H MRI and CT images. For this group of patients, the mean±SD target registration error for the direct rigid, indirect rigid, direct affine, indirect affine methods, direct diffeomorphic and indirect diffeomorphic algorithms were 17.4±3.9mm, 17.2±3.3mm, 19.6±12.7mm, 14.7±3.2mm, 20.4±12.8mm and 13.5±3.3mm, respectively. Table **2.2** displays the TRE results for all 15 patients. The Wilcoxon signed-rank test demonstrates a statistically significant difference between the direct and indirect affine (p=0.036) and diffeomorphic (p=0.006) methods of image registration. No statistically significant difference was observed between the direct and indirect rigid methods (p=0.570). The TRE of 13.5±3.3mm for the diffeomorphic indirect method, using ^{1}H MRI, was more accurate than all the other methods (p values ranging from 0.001 to 0.015). These results are displayed graphically as a box plot in Figure 2.5. Table **2.3** displays p values comparing TREs for every method.

Table 2.2 Mean target registration errors (in mm) for the direct and indirect rigid, affine and diffeomorphic registration methods.

	Rigid		Affine		Diffeomorphic	
Patient	Direct	Indirect	Direct	Indirect	Direct	Indirect
1	12.9	12.5	11.6	12.9	12.1	11.5
2	23.6	22.7	13.4	15.4	11.3	12.0
3	14.8	15.6	23.6	14.1	26.3	10.6
4	18.4	16.0	22.0	19.6	20.7	18.7
5	20.0	18.5	14.0	11.7	12.7	10.2
6	19.8	19.8	23.7	19.8	25.1	19.7
7	21.4	22.5	14.9	14.8	15.1	14.5
8	14.9	18.6	15.3	17.3	15.0	15.9
9	14.7	16.5	62.6	16.8	63.4	15.8
10	21.8	18.8	20.3	12.3	22.4	12.1
11	19.8	14.5	13.0	9.7	14.6	8.8
12	12.6	17.5	13.9	16.6	13.7	15.4
13	10.1	11.2	8.8	9.2	13.1	8.9
14	19.5	18.3	18.5	16.1	20.8	13.9
15	16.7	14.8	18.0	14.3	19.7	14.0
Mean	17.4	17.2	19.6	14.7	20.4	13.5
SD	3.9	3.3	12.7	3.2	12.8	3.3
Median	18.4	17.5	15.3	14.8	15.1	13.9
Range	10.1-23.6	11.2-22.7	8.8-62.6	9.2-19.8	11.3-63.4	8.8-19.7
P value Direct vs indirect	0.594		0.036		0.006	
P value vs indirect diffeomorphic	0.015	0.003	0.005	0.001	0.006	N/A

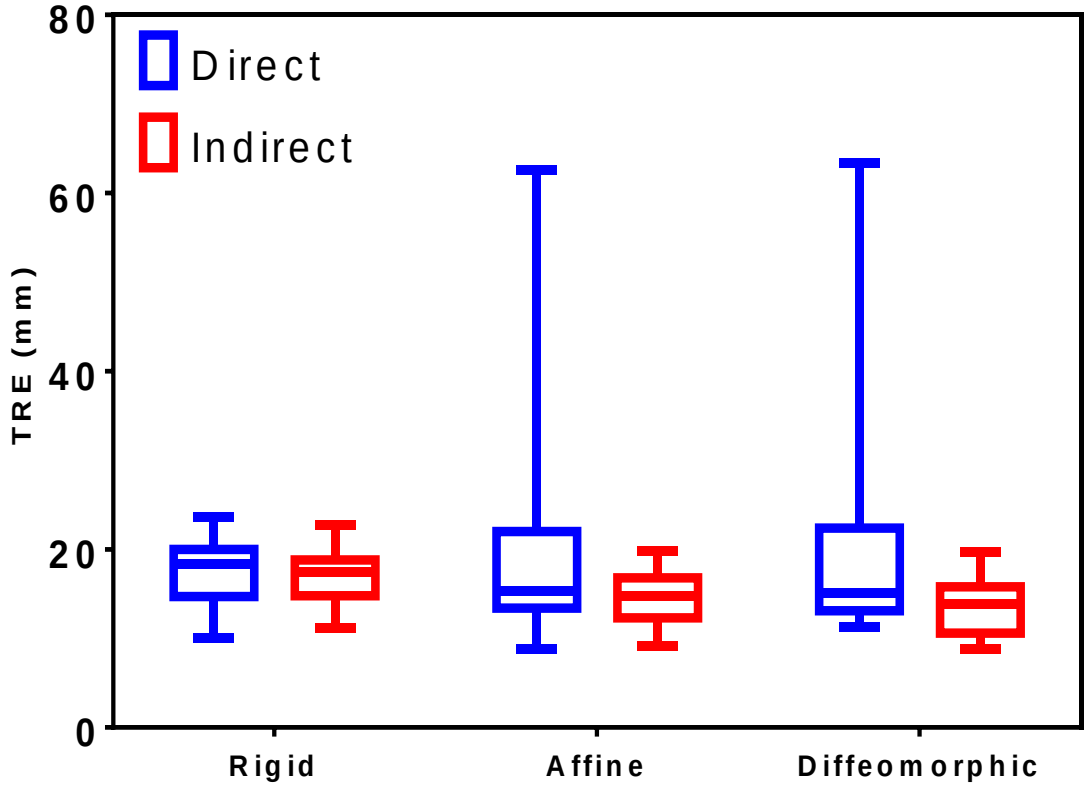

Figure 2.5 Box plot of target registration errors (TRE) for the direct and indirect rigid, affine and diffeomorphic registration methods. The central mark of each box represents the median, with its edges the 25th and 75th percentiles. The whiskers extend to the minimum and maximum values.

Table 2.3 Wilcoxon p values comparing TREs for all methods.

		Rigid		Affine		Diffeomorphic	
		Direct	Indirect	Direct	Indirect	Direct	Indirect
Rigid	Direct	N/A	0.594	0.691	0.081	0.532	0.015
	Indirect	0.594	N/A	0.932	0.011	0.629	0.003
Affine	Direct	0.691	0.932	N/A	0.036	0.088	0.005
	Indirect	0.081	0.011	0.036	N/A	0.27	0.001
Diffeomorphic	Direct	0.532	0.629	0.088	0.27	N/A	0.006
	Indirect	0.015	0.003	0.005	0.001	0.006	N/A

An example in which the direct method failed was for patient 9, which was characterized by extreme hypoventilation including no ventilation in both the left and right lower lungs (Figure 2.6). The direct registration broke down for the affine and diffeomorphic methods as the amount of ventilation was insufficient to permit multimodal alignment.

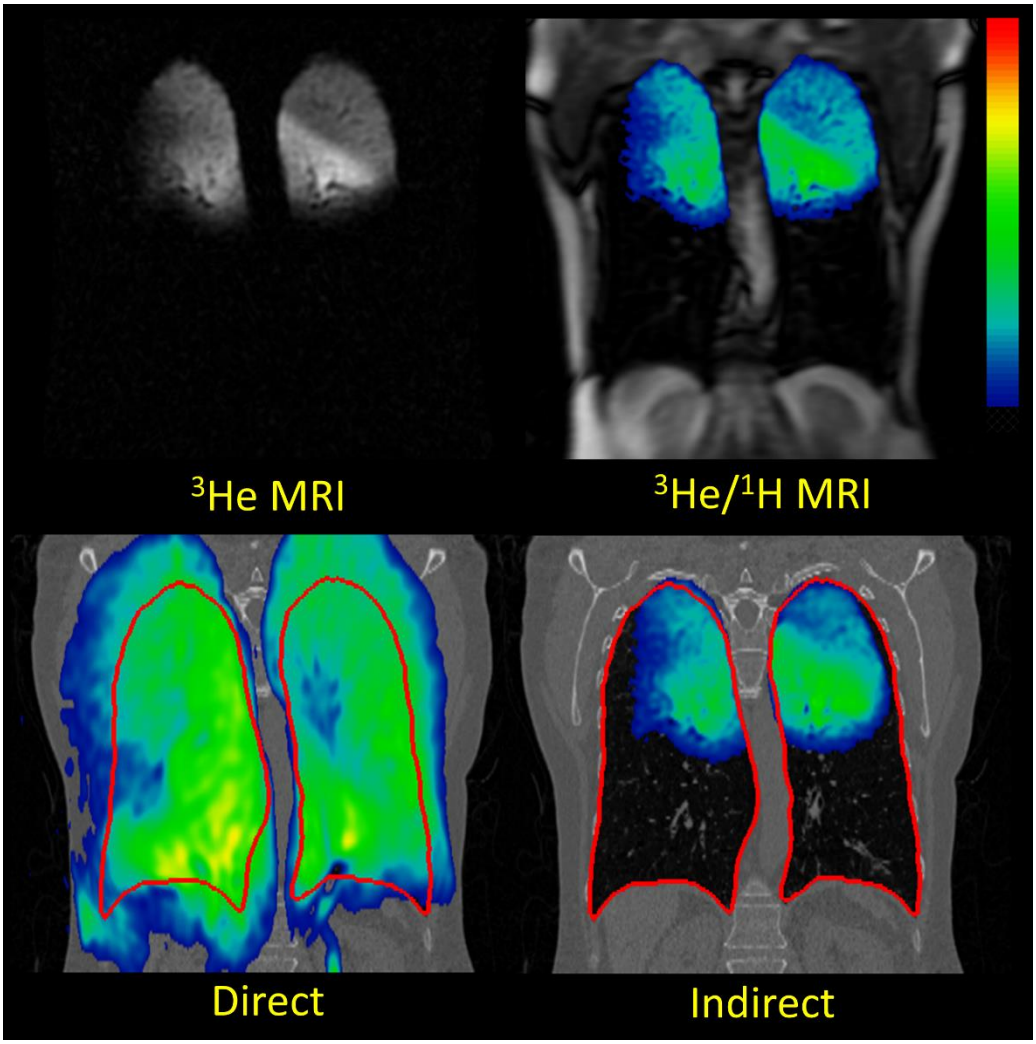

Figure 2.6 Corresponding coronal slices of patient 9 showing registered ^{3}He MRI fused with CT via the direct (bottom left) and indirect (bottom right) diffeomorphic methods with preregistered ^{3}He MRI (top left) and ^{1}H MRI fused with ^{3}He MRI (top right). The direct method breaks down, attempting to stretch the ^{3}He images which show ventilation in the upper lobes only, across the whole lung.

Although not as extreme an example, Figure 2.7 (blue arrow) demonstrates where the direct method inaccurately registers ^{3}He MRI to CT by increasing the ventilation signal near the base of the left lung. Conversely, the indirect method yields a more clinically realistic registration.

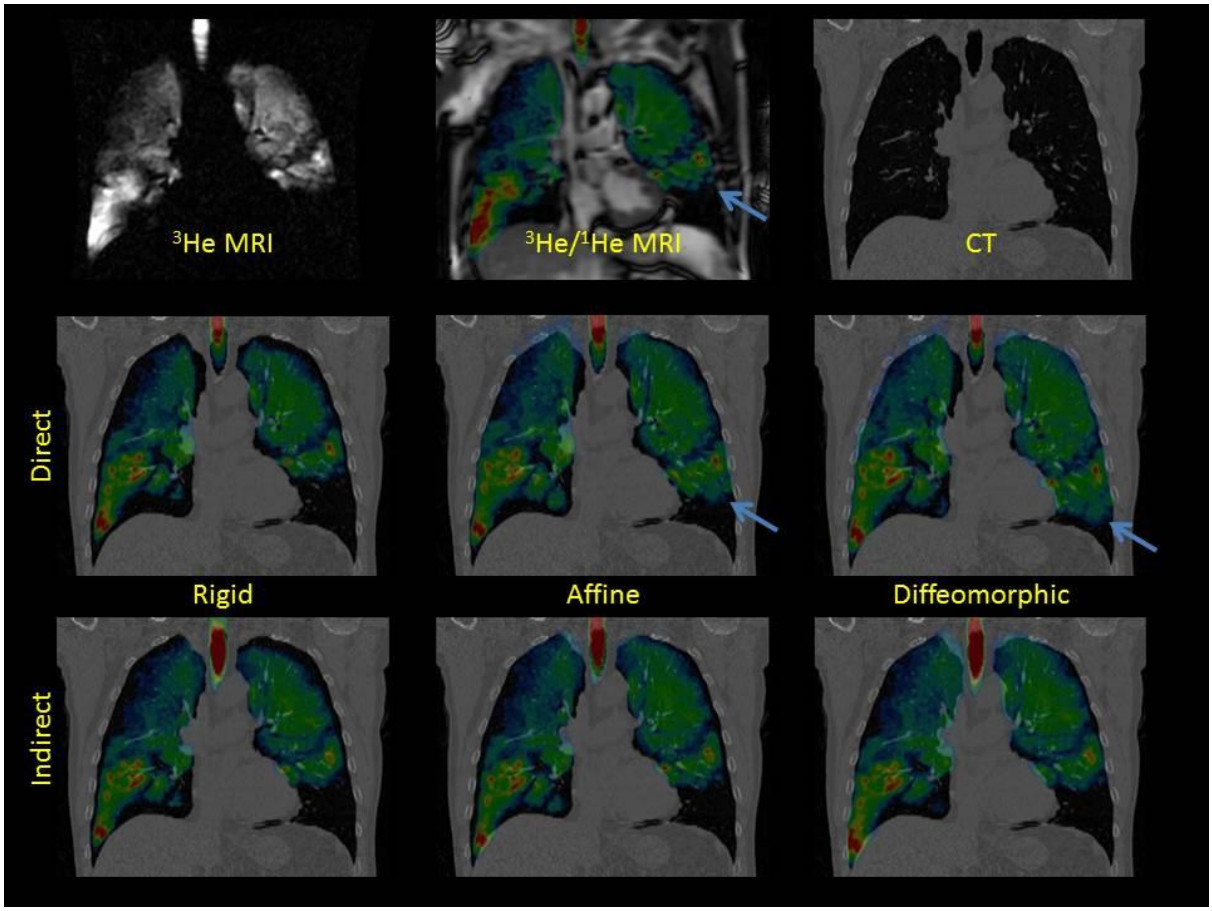

Figure 2.7 Corresponding coronal slices of patient 14 showing registered ^{3}He MRI fused with CT via the direct (middle row) and indirect (bottom row) rigid, affine and diffeomorphic methods with preregistered ^{3}He MRI (top left), ^{1}H MRI fused with ^{3}He MRI (top centre) and CT (top right). The blue arrows near the base of the left lung indicates a registration error in the direct affine and diffeomorphic methods when compared to the corresponding slice of the unregistered ^{3}He MRI.

The potential for providing regional quantitative ventilation of specific anatomical structures is demonstrated in Figure 2.8 for patient 11 where the pulmonary CT lobar masks are superimposed on the registered ^{3}He MRI. For this patient, the percentage ventilation for each lobe was RUL=18.39% RML=14.71%, RLL=25.06%, LUL=27.20%, and LLL=14.64%. This method of quantifying lobar ventilation will be explored further in Chapter 3.

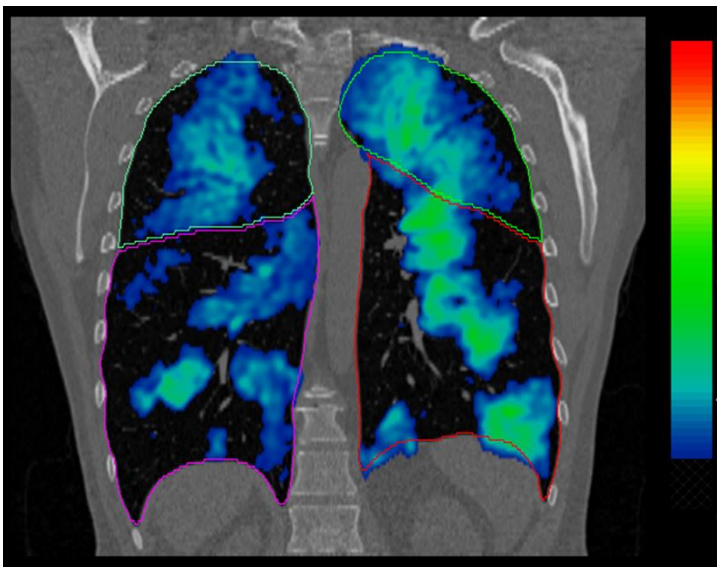

Figure 2.8 Example slice of patient 11 showing the CT lobar masks fused with ^{3}He MRI after registration.

2.5 Discussion

Image registration of hyperpolarised gas MRI has previously been published in the context of perfusion MRI using controlled gas administration in pigs (Rizi *et al.*, 2003; Hong *et al.*, 2005) while human *in vivo* ^{3}He MRI to CT image registration has been reported as part of a study on the feasibility of lung cancer treatment planning with ^{3}He MRI (Ireland *et al.*, 2007a). Furthermore, the importance of the image acquisition procedures on the resultant image registration of ^{3}He MRI to CT has been demonstrated (Ireland *et al.*, 2008). When there are major differences in patient positioning and posture between the MRI and CT image acquisitions, there can be large errors in image registration when a rigid algorithm is applied.

The data set used in this study is from asthma patients. A previously reported ^{3}He MRI registration paper involved lung cancer patients (Ireland *et al.*, 2008). The registration accuracy was improved in that work by having the patient positioning match as closely as possible between the MRI and CT acquisitions. In the current work, matching MRI and CT patient positioning was not part of the study protocol. The CT was performed in a standard manner, involving a breath hold that was different to that used for the MRI acquisition and with a curved diagnostic bed. The objective of the current study was not to improve upon the radiotherapy level of registration accuracy, but rather to investigate the use of the same breath-hold ^{1}H MRI within the image registration and whether it enables target registration error (TRE) analysis to be performed along with quantification of regional ventilation.

In the present work, the additional ^{1}H MRI is used as an intermediate step in the registration of hyperpolarised gas MRI to CT. The method of automatic registration assumes intrinsic spatial registration of gas MRI and ^{1}H MRI, preferably due to same breath-hold acquisition (Wild *et al.*, 2011), although the method is still potentially viable if hyperpolarised gas and ^{1}H MR image registration is acquired from separate breath-holds (Ireland *et al.*, 2009).

In addition, application of the image registration transformation that is calculated from hyperpolarised gas MRI to CT to the ^{1}H MRI landmarks provides a method of assessing the accuracy of gas MRI to CT registration with TRE analysis. Although high quality hyperpolarised gas MR images often contain structural detail that could potentially be used for TRE analysis (Ireland *et al.*, 2008), the advantage of the same breath-hold ^{1}H MRI method is that it allows for identification of spatially correlated anatomical landmarks that may not be seen on the hyperpolarised gas MR images due to ventilation defects and partial volume effects. This advantage is demonstrated in the simulation study, in which the indirect method using the ^{1}H MRI is independent of the severity of ventilation defect (TRE range 16.0 to 18.7mm) whereas all the direct registration methods failed when the moving image was set to only one or two lobes of the ^{3}He MR images (TRE>80mm).

For the group of 15 asthma patients investigated in this study, the indirect affine and diffeomorphic methods demonstrated statistically significant improvements in TRE compared to their corresponding direct methods. The diffeomorphic indirect method of image registration, using ^{1}H MRI, was more accurate than the other direct and indirect methods (p values ranging from 0.001 to 0.015). Due to the differences in breathing maneuver and physiological variations between inter-session CT and MRI scans, the diffeomorphic deformable algorithm was able to account better for large deformations than the global rigid and affine transformations. Similarly, the indirect affine method performs better than the rigid method due to its ability to account for scaling and shearing in addition to translations and rotations which is necessary to stretch the lungs, particularly at the bases, when acquired at different respiratory phases as in this study.

With the direct hyperpolarised gas MRI to CT image registration method, there was no statistically significant improvement in using the diffeomorphic transform for the direct registration. The direct affine and diffeomorphic registration broke down for one patient in the study (Figure 2.6) and yielded clinically unrealistic deformations of ^{3}He MRI for several patients (Figure 2.7). Hence, caution should be exercised when performing affine or deformable registration of ^{3}He MRI to CT if an intermediate ^{1}H MRI to CT step is not used.

The indirect method has the advantage that it is independent of ventilation defect as it does not rely on ^{3}He ventilation for the registration. For example, the TRE for patient 8 was better for the direct method than the indirect. This patient had near homogenous ventilation, possibly indicating that the direct method works well for patients with sufficient ventilation, while potentially the benefits of the indirect method are more apparent for those cases with greater ventilation defect.

The results of the patient study demonstrated large target registration error values (> 8mm) for both direct and indirect methods. Registration errors may be attributable to the differences in resolution between modalities. Although the resolution of ^{3}He MRI is superior to SPECT, it is still lower than that of CT.

In this study, the lower resolution ^{3}He MR images were registered to higher resolution CT thus requiring interpolation of the former to match its resolution. This would inadvertently generate data that may not be representative of ground truth. Furthermore, although this study demonstrated improvements in the indirect method for some patients, the in-plane resolution in the y direction of the same-breath ^{1}H MR images was twice that of ^{3}He MRI (6mm vs 3mm) and thus suffered from greater partial volume effects. This may have limited the potential improvements of incorporating ^{1}H MRI in the registration. As multi-nuclear MRI acquisition technology and the resolution of same-breath ^{1}H images improve, the indirect registration may show further improvements. For a fairer comparison, the ^{3}He MR images could be resampled to match that of the ^{1}H MRI.

Registration errors may also be attributable to differences between acquisition settings in terms of patent positioning and breathing manoeuvre. ^{3}He MRI was acquired at FRC+1 litre whereas inspiration CT was acquired at TLC. Visual assessment of corresponding slices for both modalities indicated large differences for some patients, especially at the base of the lungs where the largest amount of respiratory movement occurs. This was also demonstrated from visual evaluation of the warped ^{3}He MR images overlaid on anatomical CT where overlaps in the former were observed at the base. Registration accuracy may be enhanced by improving the image acquisition protocol. Ireland *et al* (2008) demonstrated significant improvements in rigid registration by reproducing the same breath-hold and body positions during image acquisition of CT and ^{3}He MRI. An improved image acquisition protocol to account for this limitation is proposed in chapter 5.

Another limitation of our study data is that there is a difference in resolution between the ^{1}H MRI and CT images especially in the z direction (10mm vs. 1mm). This may cause observer errors in landmark identification due to partial volume effects at low resolutions. The slice thickness of 10mm was chosen to provide high signal to noise and to ensure full volumetric lung coverage within a breath-hold time achievable by patients, important considerations when both ^{3}He and ^{1}H images are acquired within the same breath. However, this

limitation may be mitigated by recent improvements in MRI technology that provide superior resolution for both same-breath acquired nuclei (Horn *et al.*, 2014).

Furthermore, the landmark annotation strategy adopted in this study may have given rise to uncertainties in the validation. Firstly, only a limited number of landmarks were identified (median: 31) per patient due to the time constraints involved with manually delineating corresponding landmarks. Secondly, the locations selected were similar for each selected slice and included some points outside the lung such as the bifurcation of the trachea. Due to the low signal to noise ratio in the lungs for the ^{1}H MR image, high contrast structures were more difficult to observe than for CT. Therefore, the calculated TREs for the selected landmarks may not provide a complete representation of registration accuracy. Previous work has shown the distribution of landmarks to have significant effects on TRE values (Kabus *et al.*, 2009). Further work will increase the total number of landmarks and ensure they are well-distributed to improve the overall assessment of registration accuracy.

Although the TRE landmark validation method is the most popular validation method for lung registration, further insights may be provided by alternative validation techniques. In particular, subsequent investigations will use overlap measures such as the Dice and Jaccard coefficients to assess volumetric overlap and spatial alignment of ^{1}H MRI and CT lung segmentations. This will require accurate lung segmentations for both modalities using semi-automatic algorithms which allow manual intervention where segmentation errors exist. Although overlap measures do not provide information on the accuracy of alignment of structures within the lung, they provide a measure for the assessment of lung boundaries alignment and were one of the validation criteria employed in the EMPIRE10 challenge (Murphy *et al.*, 2011).

Limiting the registration to the voxels encompassed by these lung segmentations may improve multi-modal registration as has been shown for intra-modal CT registration (Murphy *et al.*, 2011). Subsequent experiments will investigate this hypothesis. Segmentations of ventilated and total lung

volumes derived from the ^{3}He and ^{1}H MR images, respectively, can be useful for calculating percentage ventilated volumes (Woodhouse *et al.*, 2005). As indicated by the simulation study results, these values may predict which patients could benefit from the indirect method where lower percentage ventilated volumes favour the indirect method. Further work is required to validate this in patient studies.

For this study, only the transform (rigid, affine and diffeomorphic) and the moving image (^{3}He MRI for direct and ^{1}H MRI for indirect) were varied for each patient while all other registration parameters such as similarity metrics, multiresolution stages and optimization remained constant. Due to inter-patient variations in ventilation heterogeneity and respiratory states, further improvements in registration may be gained by patient specific parameterization.

There are many potential clinical applications of improved hyperpolarised gas MR image registration since accurate registration of anatomical and functional images can enhance both image interpretation and quantification. For a variety of lung diseases, registration of hyperpolarised gas MRI to CT would enable the pulmonary ventilation to be assessed against the underlying anatomical CT structure, which serves as the gold standard. The feasibility of using the indirect registration technique for regional quantification of ventilation of specific pulmonary structures is demonstrated in Figure 2.8. In addition, registration to CT is critical in radiotherapy for the implementation of functionally weighted treatment planning (Ireland *et al.*, 2007a; Bates *et al.*, 2009; Partridge *et al.*, 2010).

2.6 Conclusion

This study demonstrates the benefit of a method of automatic image registration of hyperpolarised gas MRI to CT indirectly via a ^{1}H MRI that is acquired in the same breath-hold as gas MRI data. This study also shows that inclusion of same breath-hold ^{1}H MRI enables TRE quantification of hyperpolarised gas MRI to CT image registration. Evaluation on a simulation

study and in 15 clinical cases demonstrates that TRE analysis is practical and that image registration accuracy can be improved when the additional anatomical ^{1}H MRI information is incorporated. Accurate image registration is critical for quantification of regional ventilation using hyperpolarised gas MRI and CT.

Chapter 3
Comparison of CT-based lobar ventilation with ^{3}He MRI ventilation measurements

Purpose: To compare lobar lung ventilation, computed from expiratory and inspiratory CT, with direct measurements of ventilation from hyperpolarised ^{3}He MRI using the complementary anatomical information from same-breath ^{1}H MRI scans to co-register the multi-modality images.

Methods: The study was approved by the national research ethics committee and written patient consent was obtained. 30 asthma patients underwent breath-hold CT at total lung capacity (TLC) and functional residual capacity (FRC). Same breath-hold ^{3}He MRI and ^{1}H MRI were acquired at a lung volume of FRC+1 litre. Lobar segmentations, delineated by major fissures on both CT scans, were used to calculate the percentage ventilation per lobe from the change of inspiratory and expiratory lobar volumes. CT-based ventilation was compared with ^{3}He MRI ventilation using diffeomorphic image registration of ^{1}H MRI to CT, which enabled indirect registration of ^{3}He MRI to CT. Statistical analysis was performed using the Wilcoxon signed-rank test, Pearson correlation coefficient and Bland-Altman analysis.

Results: The mean absolute difference between CT and ^{3}He MRI percentage ventilation volumes across all lobes was 4.0% (mean ± SD for each lobe: RUL+RML=5.4±3.3%; RLL=3.7±3.9%; LUL=2.8±2.7%; LLL=3.9±2.6%, Wilcoxon signed-rank test: $p < 0.05$). The Pearson correlation coefficient between the two techniques across all lobes was 0.65 ($p < 0.001$). Greater percentage ventilation was seen in the upper lobes with ^{3}He MRI and in the lower lobes with the CT model. This was confirmed by Bland-Altman analysis, 95% limits of agreement: RUL+RML (-2.4, 12.7), RLL (-11.7, 4.6), LUL (-4.9, 8.7), LLL (-9.8, 2.8).

Conclusion: Percentage regional ventilation per lobe calculated from CT is comparable to a direct measurement of lung ventilation with hyperpolarised ^{3}He MRI. This work provides evidence for the validity of the CT model of ventilation and also demonstrates that same-breath ^{1}H MRI enables regional interpretation of ^{3}He ventilation MRI upon the underlying high-resolution lung anatomy from CT.

3.1 Preface

The majority of the material in this chapter was originally published as a full length article in the journal *Radiology*:

> Tahir BA, Van Holsbeke C, Ireland RH, Swift AJ, Horn FC, Marshall H, Parra-Robles J, Hartley R, Laurencin M, Kay R, Siddiqui S, Brightling CE, Vos W, Wild JM (2016). Comparison of CT-based Lobar Ventilation with Hyperpolarised ^{3}He MRI using Image Registration. Radiology 278(2):585-92

Additional material is presented here that was not included in the published article.

The work has also been presented at the following conferences:

> Tahir BA, Van Holsbeke C, Ireland RH, Swift AJ, Horn FC, Marshall H, Parra-Robles J, Hartley R, Laurencin M, Kay R, Siddiqui S, Brightling CE, Vos W, Wild JM. Comparison of CT-based lobar ventilation with hyperpolarised ^{3}He MRI using image registration. 6th International Workshop on Pulmonary Functional Imaging 2013, Madison, Wisconsin, USA
>
> Tahir BA, Van Holsbeke C, Ireland RH, Swift AJ, Horn FC, Marshall H, Parra-Robles J, Hartley R, Laurencin M, Kay R, Siddiqui S, Brightling CE, Vos W, Wild JM. Comparison of CT-based lobar ventilation models with ^{3}He MRI ventilation measurements in asthmatics. American Thoracic Society 2014, San Diego, USA
>
> Tahir BA, Van Holsbeke C, Ireland RH, Swift AJ, Horn FC, Marshall H, Parra-Robles J, Hartley R, Laurencin M, Kay R, Siddiqui S, Brightling CE, Vos W, Wild JM. Comparison of CT-based lobar ventilation models with ^{3}He MRI ventilation measurements in asthmatics. European Respiratory Society International Congress 2014, Munich, Germany

3.2 Introduction

Hyperpolarised gas (^{3}He and ^{129}Xe) ventilation-weighted MRI is a technique that is well suited to investigate regional ventilation patterns in obstructive airways diseases which has sensitivity to early signs of lung obstruction in a variety of pathologies (Kauczor *et al.*, 1996; Kirby *et al.*, 2011; Altes *et al.*, 2001; van Beek *et al.*, 2007). Images acquired at breath-hold give a static picture of distribution of inhaled gas across the whole lung volume (Wild *et al.*, 2004) and have a voxel intensity that is directly proportional to lung-ventilation. In asthmatics, ^{3}He MR images depict reduced ventilation and increased ventilation heterogeneity with increasing disease severity (Altes *et al.*, 2001; de Lange *et al.*, 2006), and are sensitive to regional ventilation changes in response to challenge such as methacholine inhalation or exercise (Samee *et al.*, 2003; Tzeng *et al.*, 2009) and bronchodilator treatment (Altes *et al.*, 2001). Combining the gas ventilation images with lung volume measurements made from anatomically registered ^{1}H images (Wild *et al.*, 2011) enables the calculation of indices such as percentage ventilated lung volume (Woodhouse *et al.*, 2005). Despite the exquisite sensitivity of hyperpolarised gas MRI, it has yet to achieve widespread clinical uptake and as such alternative techniques to image lung ventilation that utilize more clinically widespread modalities such as CT are of interest.

In previous work by De Backer et al. (De Backer *et al.*, 2010), it was shown that a CT model of ventilation computed from two breath-hold CT scans (expiratory and inspiratory) at a lobar level yields realistic information on regional ventilation patterns in mild asthmatic patients and can be used as a surrogate for ventilation. This ventilation model has previously been validated against SPECT (De Backer *et al.*, 2010). However, SPECT suffers from lower spatial-resolution when compared with competing ventilation modalities such as hyperpolarised-gas MRI and does not permit image acquisition in a single breath-hold.

Conversely, the fissures, which are needed to differentiate between pulmonary lobes, cannot be reliably identified on ^{3}He MR images. Furthermore, unlike

SPECT/CT, no multimodality CT-MRI scanner exists which allows simultaneous co-registered acquisition of the two modalities. Therefore, before a valid comparison of lobar ventilation with the two methods can be performed, ^{3}He MRI and CT first need to be mapped to the same coordinate frame via accurate anatomically guided image registration.

This study compares lobar lung ventilation, computed from expiratory and inspiratory CT, with direct measurements of ventilation from hyperpolarised ^{3}He MRI using the complementary anatomical information from same-breath ^{1}H MRI scans to co-register the multi-modality images.

3.3 Methods

3.3.1 Ethics & patient characteristics

The study was approved by the national research ethics committee and written patient consent was obtained (ClinicalTrials.gov: NCT01545726). Between March 2012 to February 2013, 30 asthmatics with sputum eosinophilia and moderate-to-severe asthma (GINA2-5) enrolled on the study. The inclusion criteria were greater than 18 years of age, physician diagnosis of asthma, currently on GINA step 2 to 5 asthma therapies, sputum eosinophil count greater than or equal to 2%. The exclusion criteria included other acute illnesses, recent or current lower respiratory tract infection, contra-indication to MRI, BMI <17 or >40 kg/m^2, women of child-bearing potential. The characteristics of these patients can be found in Table **3.1**. Out of the 30 patients, 16 were male and 14 were female. The mean±SD (range) age across all patients was 52.8±11.2 (21 to 65); male 51.9±14.0 (21 to 65) v. female 54±7.2 (41 to 64), t test: p = 0.6.

CT, MRI and pulmonary function tests (PFTs) were all performed after patients had taken their regular short-acting bronchodilator. PFTs and CT were performed on the same day. MRI was performed within 6 days of the PFTs and CT with a mean±SD interval of 1.5±0.8 days and range of 1 to 4 days.

Table 3.1 Summary of patient characteristics and lung function parameters.

	Age	Sex	FEV_1 (L)	Predicted FEV_1 (%)	FVC (L)	Predicted FVC (%)	FEV_1/FVC (%)	TLC (L)	FRC (L)
1	49	F	1.0	39.3	2.1	73.7	45.5	4.7	3.1
2	53	M	1.6	42.6	3.9	83.6	40.6	7.4	4.3
3	63	M	3.2	106.3	4.5	115.5	72.3	7.4	3.2
4	53	F	0.6	27.7	1.3	46.4	50.0	5.5	3.8
5	65	M	1.7	57.4	3.8	98.4	45.5	6.9	5.1
6	56	F	2.1	98.6	3.1	123.8	66.8	4.9	2.4
7	63	F	1.5	69.8	2.1	83.6	70.1	3.9	2.4
8	53	F	2.0	74.4	2.7	85.8	73.6	5.0	2.7
9	53	F	1.5	60.7	2.9	99.0	52.1	6.3	4.1
10	41	F	1.5	53.8	2.0	62.9	73.5	3.9	2.9
11	41	M	3.6	95.7	5.2	114.0	69.2	7.1	3.5
12	51	F	0.9	35.9	1.9	66.5	45.9	5.6	4.6
13	59	F	2.1	95.0	3.1	118.3	67.7	5.1	3.3
14	62	M	1.4	43.9	3.9	94.6	36.4	9.0	6.6
15	61	F	2.2	105.0	3.0	123.5	71.0	5.7	2.8
16	45	M	2.7	71.6	4.5	99.3	58.9	7.4	4.7
17	21	M	4.4	95.4	4.7	87.5	92.6	6.9	3.6
18	64	F	2.1	105.1	2.9	122.9	71.0	5.0	2.6
19	73	M	1.1	41.7	2.3	68.4	46.7	8.2	6.6
20	41	F	2.5	86.9	3.7	109.0	68.8	5.9	3.3
21	36	M	3.7	100.0	4.6	104.8	124.7	7.3	3.2
22	63	M	0.9	27.0	3.0	68.7	30.4	8.1	5.6
23	60	F	2.6	121.4	3.1	123.5	82.3	5.7	3.5
24	61	M	2.3	69.3	4.6	107.1	50.6	8.7	4.7
25	54	M	2.7	76.6	3.3	77.9	81.0	5.2	2.6
26	52	F	2.1	100.0	2.9	114.5	73.7	4.3	2.5
27	42	M	3.2	108.4	4.3	120.8	74.9	6.2	3.1
28	57	M	1.9	55.4	3.7	89.9	50.7	8.8	4.8
29	34	M	2.1	51.8	3.8	79.1	54.7	6.8	3.4
30	60	M	1.4	47.5	3.1	82.0	45.9	7.2	4.8
Mean	52.9	N/A	2.1	72.1	3.3	94.8	62.9	6.3	3.8
SD	11.2	N/A	0.9	27.7	1.0	21.4	19.2	1.5	1.2

Note: M = male, F = female, FEV_1 = forced expiratory volume in the first second of expiration, FVC = forced vital capacity, FRC = functional residual capacity, TLC = total lung capacity, L = litres. Predicted FEV_1 and FVC were calculated by dividing the FEV_1 and FVC values by their respective mean value for any person of similar age, sex and body composition.

3.4 Image acquisition

3.4.1 CT examination

All patients underwent breath-hold CT scans at total lung capacity (TLC) and functional residual capacity (FRC) on a Sensation 16 scanner (Siemens, Forchheim, Germany). The following CT settings were used: tube voltage, 120kV; tube current, 120mAs; rotation time, 0.5s; pitch, 1.5. Where available, a B30f reconstruction kernel was used or the next kernel closest to it (e.g. B35f, B60 etc.). CT in-plane resolution was approximately 0.86×0.86mm with a pixel matrix of 512×512. CT slice thickness was 1 mm with approximately 600 slices for each patient.

3.4.2 MRI examination

Hyperpolarised ^{3}He MRI was acquired in the coronal plane during FRC+1litre. FRC+1litre was selected because this is the respiratory level typically used for ^{3}He ventilation imaging. In the same breath-hold as the ^{3}He MRI, ^{1}H MR images were also acquired using methods developed for same-breath imaging of two nuclei on a GE HDx 1.5T MR scanner (GE Healthcare, Princeton, NJ, USA) (Wild *et al.*, 2011).

Helium was polarised on-site to approximately 25% using a rubidium spin exchange polariser (GE Healthcare, Amersham, UK). Patients exhaled to FRC and then inhaled 350ml of ^{3}He and 650ml of N_2. A ^{3}He transmit-receive quadrature vest coil (Clinical MR Solutions, Brookfield, WI, USA) was used to acquire ^{3}He-images with the following sequence; 2D spoiled gradient-echo, 3x3mm in-plane resolution, 10mm slice thickness, 38.4cm field of view, 1.1ms echo time, 3.6ms repetition time, 8º flip angle, 62.5kHz bandwidth and full lung coverage (20 to 24 slices). Same-breath ^{1}H images (Wild *et al.*, 2011) with the same slice thickness were acquired using the ^{1}H transmit-receive body coil of the scanner with the following sequence; 2D steady state free precession, 3x6mm in-plane resolution, 38.4cm field of view, 0.7ms echo time, 2.4ms repetition time, 50º flip angle, and 167kHz bandwidth. One patient was

excluded from the study analysis due to incomplete inhalation of ^{3}He during image acquisition. Coronal slices for same-breath ^{3}He and ^{1}H MRI and inspiration and expiration CT for an example patient are shown in Figure 3.1.

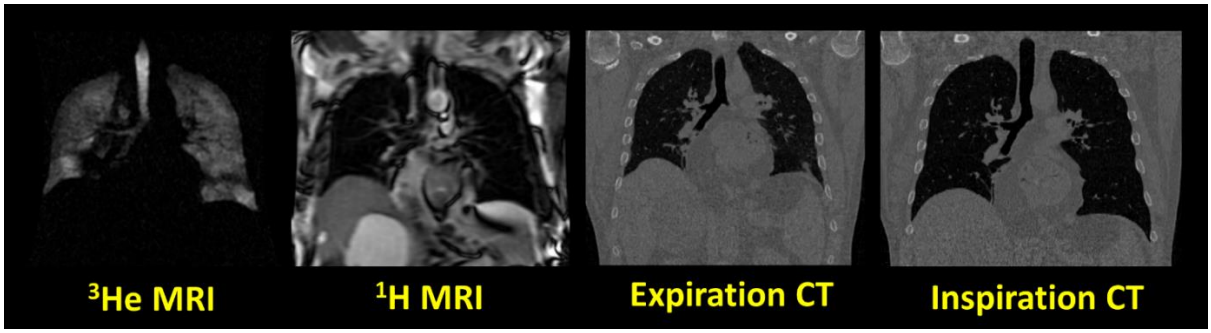

Figure 3.1 Coronal slices for same-breath ^{3}He and ^{1}H MRI and inspiration and expiration CT.

3.4.3 Lobar segmentation and volume expansion

Medical image segmentation software (Mimics; Materialise, Leuven, Belgium) was used to segment the lobes of the FRC- and TLC-CT scans by identification of major fissures in both lungs. Previous experience with the software has shown a 90% success rate for automated segmentation of the left and right oblique fissures. Although the right horizontal fissure is mostly detected, 30-50% manual modification is needed before the segmentation is correct. The right upper and middle lobes were joined due to the difficulty in identifying the minor fissures for some patients in the study. Lobar segmentations were manually adjusted in lung-regions where the automatic algorithm failed to identify the fissures. Figure 3.2 shows example axial, coronal and sagittal slices of the segmentation accuracy for a representative patient.

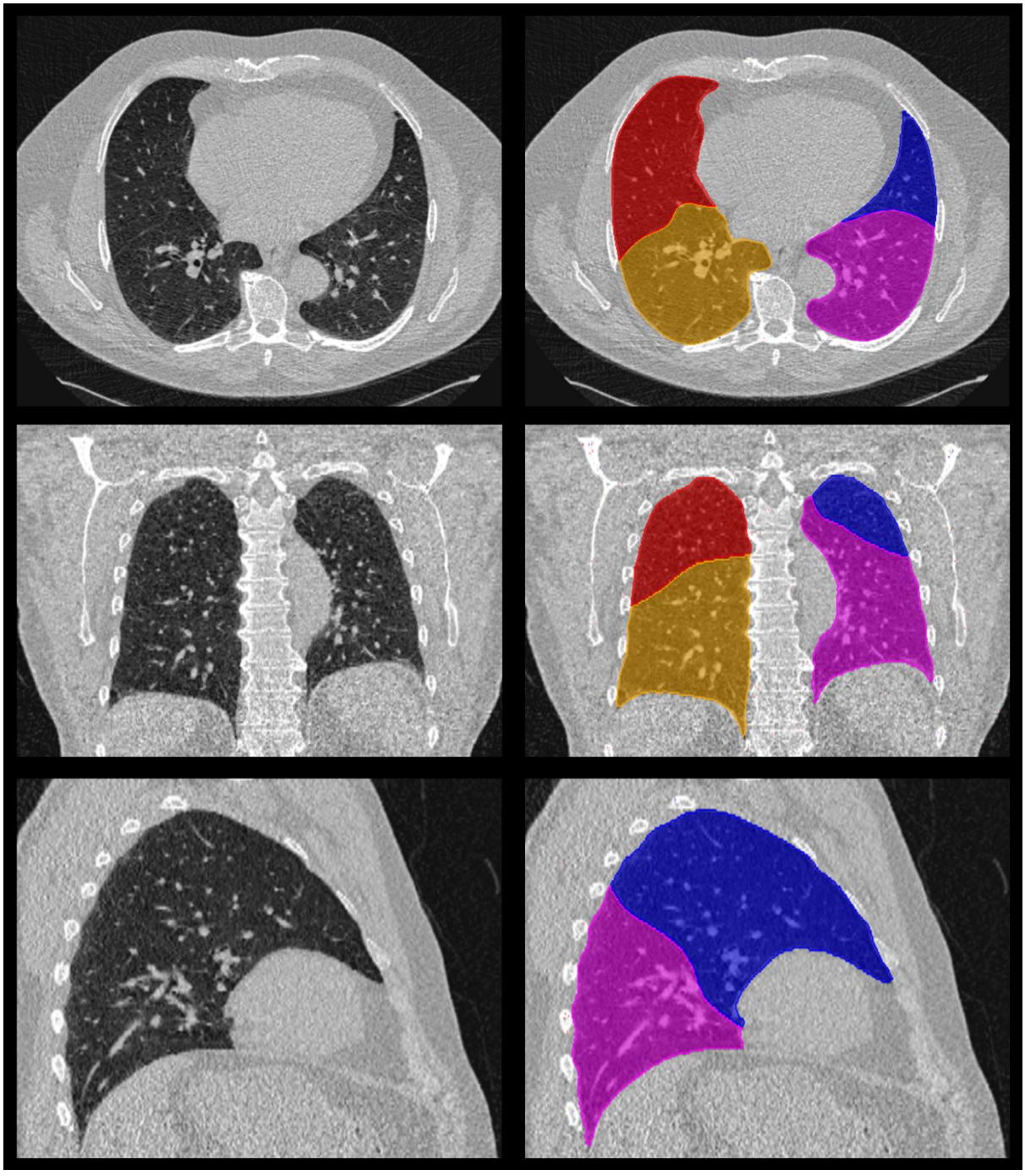

Figure 3.2 Example axial, coronal and sagittal slices demonstrating segmentation accuracy for a representative patient in the study.

These lobar-masks were used to calculate percentage regional ventilation per lobe (%$Vent_{lobe}$), expressed as the fraction of air volume (V_{lobe}) entering the lobes over the volume of air entering the whole lung (V_{lungs}) by assessing lobar volume expansion of the segmented lobar- and lung-volumes between inspiration and expiration CT data (De Backer *et al.*, 2010) as per the following equation and visually shown in Figure 3.3.

$$\%Vent_{lobe} = \frac{V_{lobe}^{TLC} - V_{lobe}^{FLC}}{V_{lungs}^{TLC} - V_{lungs}^{FLC}}$$

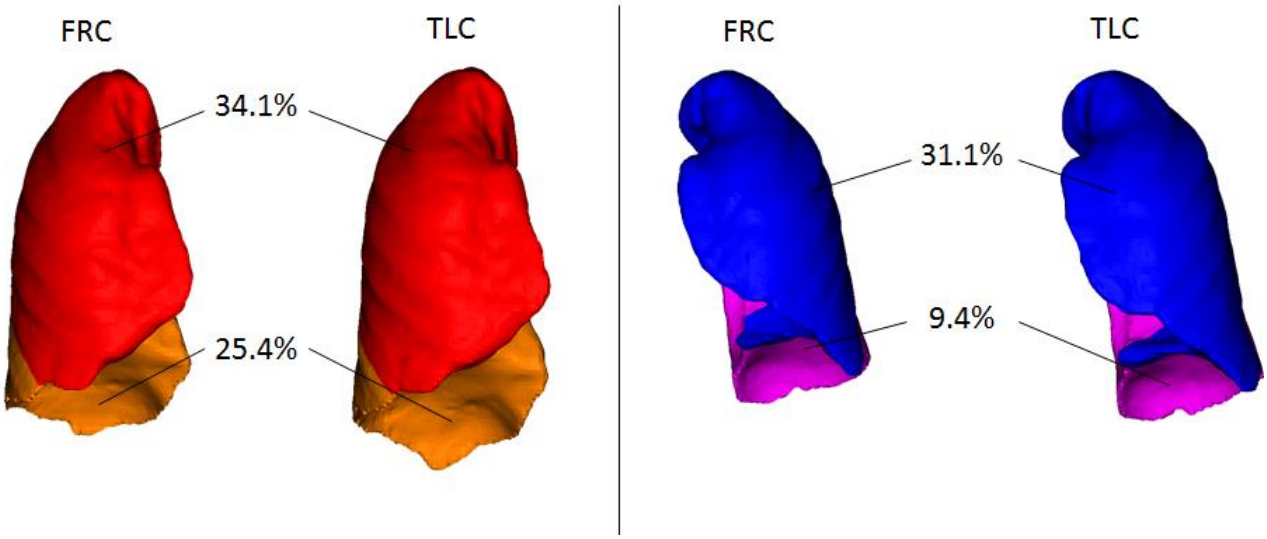

Figure 3.3 Example of percentage lobar volume expansion calculation from FRC to TLC for the right and left lungs.

3.4.4 ^{3}He MRI to CT image registration

^{3}He MR images were registered to inspiratory CT using the `antsRegistration` tool incorporated as part of the Advanced Normalization Tools (ANTs) (Avants *et al.*, 2011; Avants *et al.*, 2012). CT images were resampled to a matrix of 512×512×160 to reduce the computational times in performing registrations. For each patient, ^{3}He MRI was registered indirectly to CT via the same-breath ^{1}H MRI (Tahir *et al.*, 2014b) as discussed in the previous chapter via an initial coarse pre-alignment rigid transform followed by an affine stage. Due to the multimodal nature of the problem, the mutual information similarity metric was used with 32 histogram bins optimized via the gradient descent algorithm with a step size of 0.1. A multi-resolution Gaussian pyramid with 5 levels was used with down-sampling factors 8×6×4×2×1 and corresponding Gaussian smoothing sigmas of 4×3×2×1×0 voxels. A maximum of 10,000 iterations were set for each resolution level to ensure convergence. A diffeomorphic transformation (Avants *et al.*, 2008) was then applied to the

result of the affine transform with the same parameters for the multi-resolution Gaussian pyramid and similarity metric. A step size of 0.2 was selected for the gradient descent optimization algorithm. The registration pipeline has been detailed in Tahir *et al.* (2014b).

To reduce the computational times, 8 cores via two Intel Xeon E5-2670 eight-core processors @ 2.60 GHz were run in parallel on a 64-bit high performance Linux server using the multi-threading options available in ITK[4]. Computational times ranged from 90 to 180 minutes, including the rigid pre-alignment and affine stages.

As the ^{1}H- and ^{3}He MR images were acquired in the same breath-hold and spatially co-registered (Wild *et al.*, 2011), the output transform of the indirect registration was applied to ^{3}He MR intensity image with linear interpolation using the `antsApplyTransform` tool available in ANTs to warp it to the spatial domain of TLC-CT.

3.4.5 ^{3}He lobar ventilation

For lobar ventilation analysis, the ^{3}He MR lobar ventilation was calculated by taking the ratio of the ventilated lobar volume to the total ventilated lung-volume and required accurate segmentation of ^{3}He MRI. The ^{3}He MR images were segmented in Slicer 4 (Fedorov *et al.*, 2012) by defining a manual-threshold value in a patient specific way by visual inspection and manually removing the large airways including the trachea. An example of the resulting segmentation for a representative patient is shown in Figure 3.4. Similar to the ^{3}He MR intensity images, the `antsApplyTransform` tool was used to warp the ^{3}He MR binary segmentations to the spatial domain of TLC-CT with nearest neighbour interpolation.

The workflow used for ^{3}He MRI lobar ventilation calculation and comparison against CT-based calculations is shown in Figure 3.5.

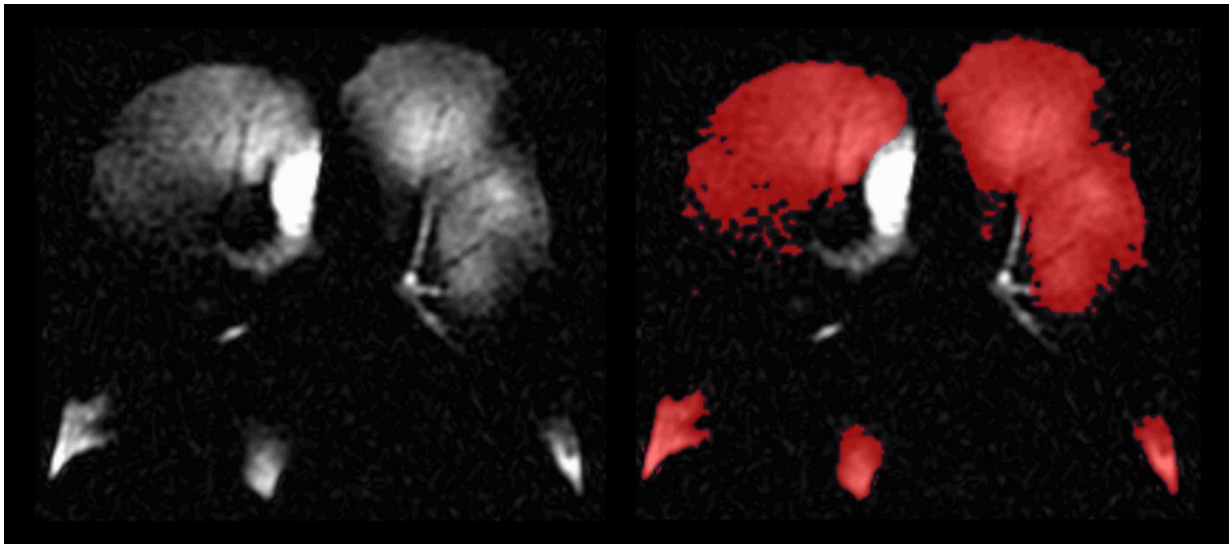

Figure 3.4 A coronal slice of a ^{3}He MRI intensity (left) along with a fused binary segmentation (right) which was manually edited to exclude the trachea and large airways.

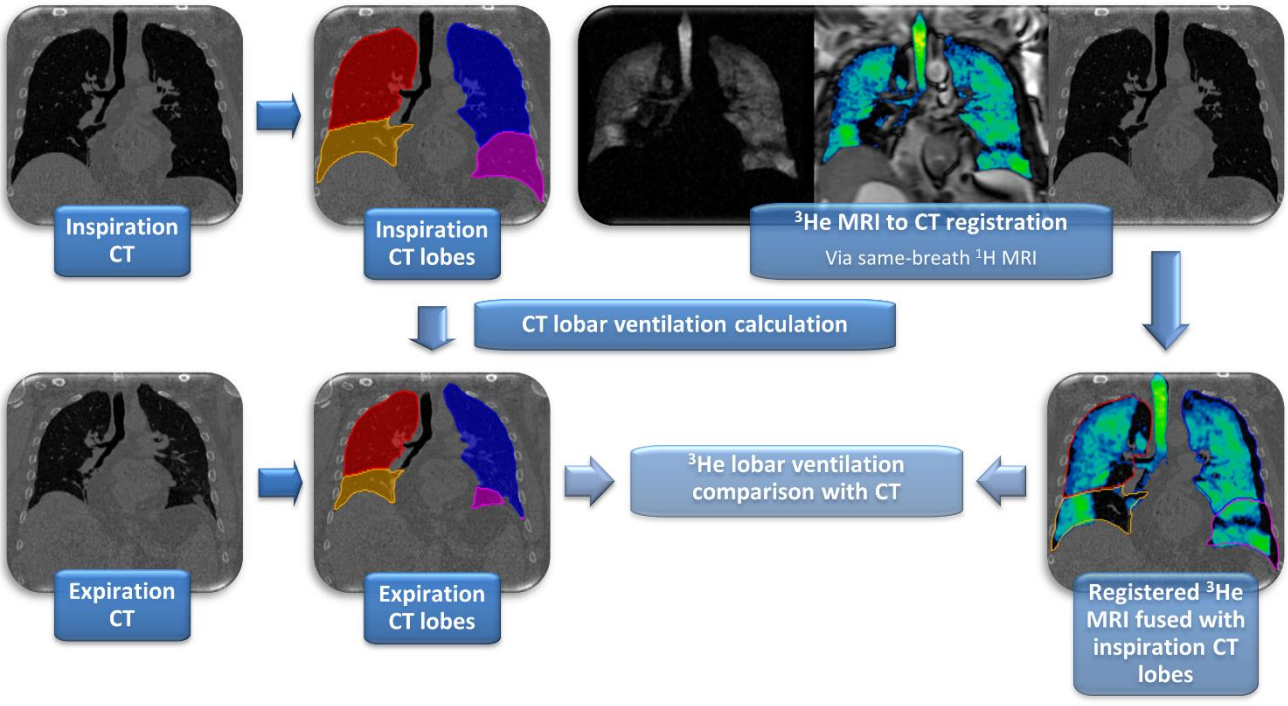

Figure 3.5 Workflow of proposed method for ^{3}He MRI lobar ventilation calculation and comparison against CT-based calculations.

3.4.6 Statistical analysis

Statistical analysis was performed by using IBM SPSS software (version 20.0; Chicago, Il, USA). A p value less than 0.05 was considered statistically significant. The independent samples t-test was used to test statistical significance in differences in age between males and females. The paired t-test was used to test statistical significance in the absolute differences in percentage lobar ventilation between CT and ^{3}He MRI. In cases in which the equal variance test and/or the normality test failed, the nonparametric Wilcoxon signed-rank test was applied. An absolute difference of less than 10% was not considered clinically significant. The Pearson correlation coefficient was used to correlate the CT and ^{3}He MRI methods across all lobes. Bland-Altman analysis was used to assess agreement between the two measurement methods for each lobe separately and across all lobes.

3.5 Results

The mean absolute difference between CT and ^{3}He MRI ventilation across lobes was 4.0% (mean±SD for each lobe: RUL+RML=5.4±3.3%; RLL=3.7±3.9%; LUL=2.8±2.7%; LLL=3.9±2.6%) with statistical significant differences for each lobe. 95% confidence intervals of absolute differences for each lobe were: RUL+RML(-1.0,11.9), RLL(-4.0,11.4), LUL(-2.4,8.1), LLL(-1.1,8.9). Absolute percentage differences are displayed in Table **3.2** and shown graphically in Figure 3.6 along with the Pearson correlation coefficient between percentage ventilation measurements in the two techniques across all lobes, which was calculated to be 0.65 ($p < 0.001$).

Table 3.2 Absolute percentage differences between CT and ^{3}He MRI lobar-ventilation measurements.

Patient	RUL+RML	RLL	LUL	LLL
1	1.80	1.13	2.55	0.38
2	3.59	0.63	0.17	2.79
3	1.96	0.17	2.67	4.80
4	8.53	0.05	1.59	6.88
5	3.25	4.34	3.48	2.40
6	6.91	6.23	5.18	5.87
7	3.14	2.10	0.26	1.31
8	5.09	0.19	0.36	5.26
9	3.63	2.66	1.28	2.26
10	7.10	2.47	0.35	4.29
11	15.20	20.15	13.84	8.89
12	6.77	5.62	4.27	5.42
13	2.34	1.20	1.96	1.58
14	2.45	3.69	2.31	1.06
15	7.52	2.54	4.04	9.01
16	7.01	4.58	4.09	6.51
17	5.33	2.97	1.54	3.90
18	1.21	2.18	4.51	3.54
19	6.63	5.56	2.62	3.69
20	5.84	3.43	1.62	0.78
21	13.96	10.42	1.90	5.43
22	5.37	1.06	2.84	3.58
23	9.02	6.53	7.45	9.95
24	5.83	3.15	1.30	3.99
25	3.55	2.42	1.38	2.51
26	2.19	2.27	2.69	2.61
27	3.23	0.27	1.58	1.37
28	4.48	4.34	1.20	1.34
29	4.91	5.21	2.50	2.20
Mean	5.44	3.71	2.81	3.92
SD	3.30	3.94	2.67	2.55

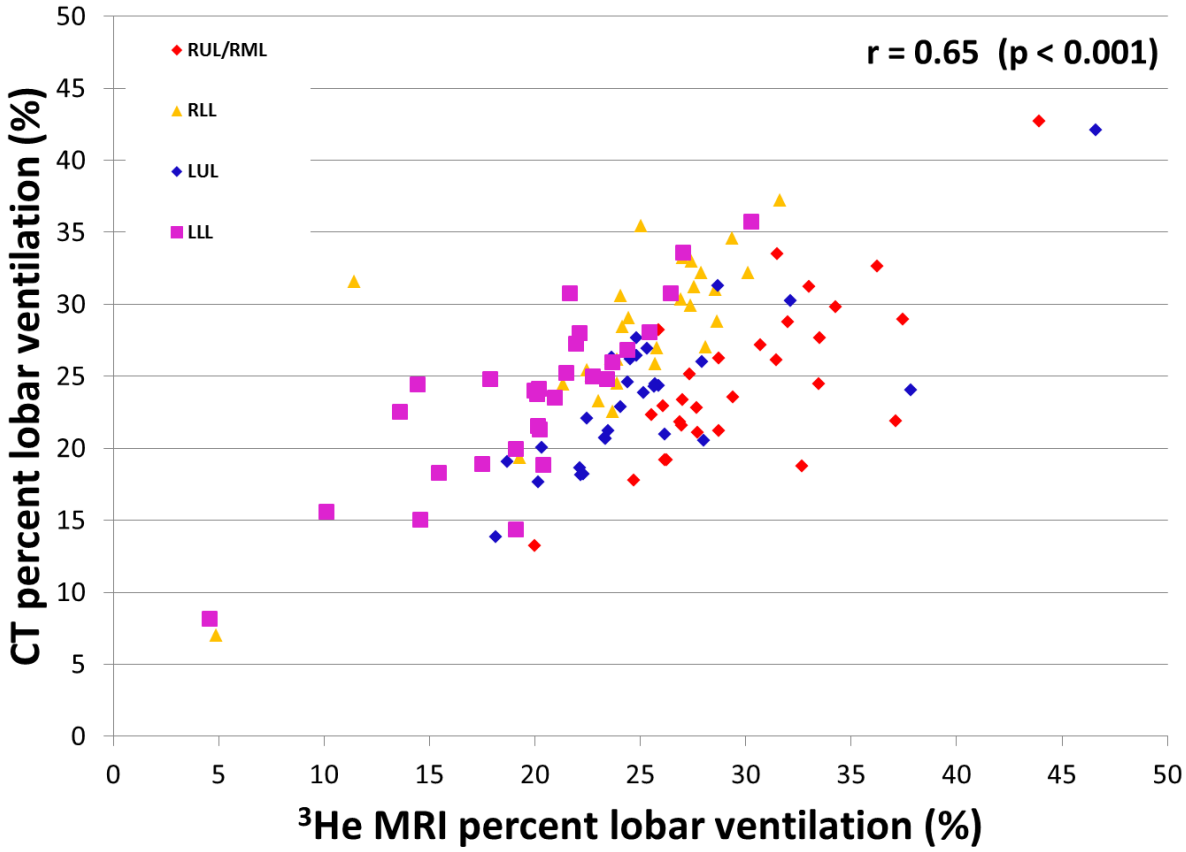

Figure 3.6 Scatter comparison of CT lobar volume expansion measurements against ^{3}He MRI lobar ventilation.

Figure 3.6 shows a trend of greater ventilation in the upper lobes with ^{3}He whilst the lower lobes show greater ventilation with the CT model. This is confirmed by Bland-Altman analysis whereby the 95% limits of agreement for each lobe were: RUL+RML(-2.4,12.7), RLL(-11.7,4.6), LUL(-4.9,8.7), LLL(-9.8,2.8). The mean bias for each lobe was: RUL+RML(5.1), RLL(-3.6), LUL(1.9), LLL(-3.5). The 95% limits of agreement and mean bias across all lobes were -10.10 to 10.10 and 0, respectively. Bland-Altman plots for each lobe separately and across all lobes are shown in Figure 3.7 and Figure 3.8, respectively.

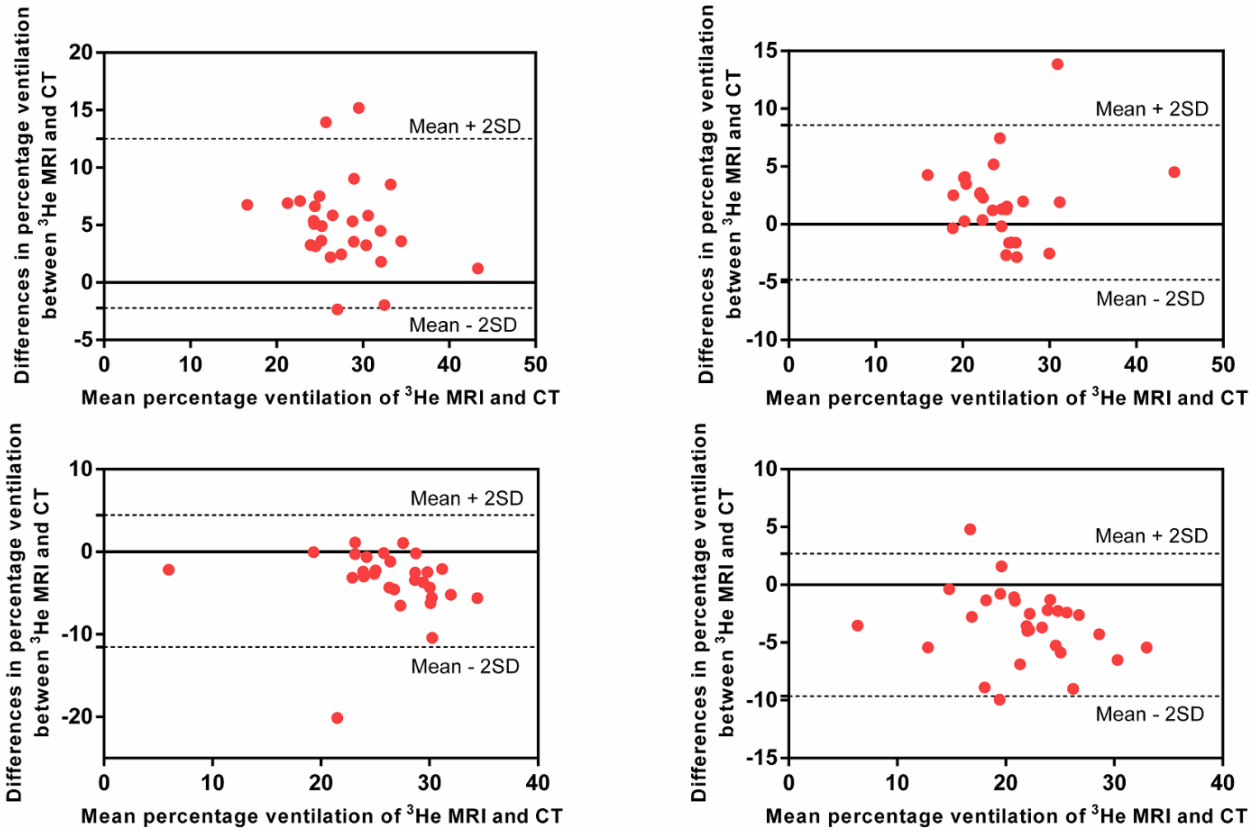

Figure 3.7 Bland-Altman plots depicting absolute percentage differences between ^{3}He MRI and CT against mean difference for RUL+RML (top left), RLL (bottom left), LUL (top right) and LLL (bottom right) with 95% limits of agreement (dashed lines).

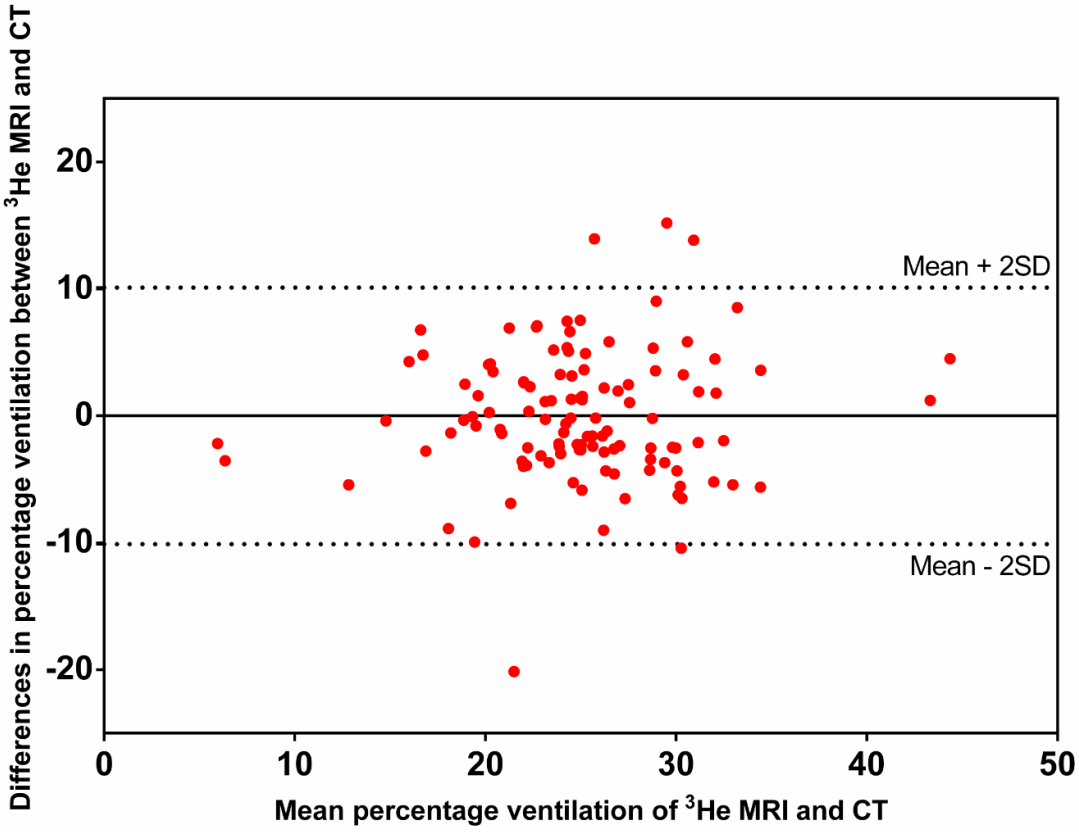

Figure 3.8 Bland-Altman plots depicting absolute percentage differences between ^{3}He MRI and CT against mean difference across all lobes with 95% limits of agreement (dashed lines).

3.6 Discussion

Voxel-based ventilation CT measures that equate changes in HU values in images acquired at inspiration and expiration to lung ventilation are highly susceptible to registration errors (Yamamoto *et al.*, 2011b; Latifi *et al.*, 2013b) and noise in HU values associated with imaging parameters such as the reconstruction algorithm (Boedeker *et al.*, 2004; Hochhegger *et al.*, 2011). In light of this, it may be more useful and accurate to quantify ventilation in CT images at a regional-level defined by the underlying lobar anatomy of the lungs. The method used here provides a surrogate for ventilation at the lobar level by assessing expansion of segmented lobes from expiration to inspiration (De Backer *et al.*, 2010). We compared the method against a more direct imaging measurement of lung ventilation, namely, hyperpolarised gas MRI,

which provides improved spatial-resolution of ventilation distribution when compared to SPECT ventilation imaging in addition to single-breath temporal resolution which matches that of the CT model. Due to the requirement of identification of fissures for lobar segmentation, pulmonary CT scans will always be required for ^{3}He MRI and SPECT lobar ventilation assessment. However, if lobar ventilation CT is seen as a valid technique, these additional functional imaging modalities may not be routinely required making the technique an attractive means of adding functionality to CT.

The ability of the CT model to measure lung ventilation makes its application quite clinically scalable in that inspiratory and expiratory CT are routinely used in multiple lung diseases to assess air trapping. For asthmatics, bronchial thermoplasty is a potential field which may benefit from the quantitative information yielded by the technique from treatment planning to the assessment of regional pathophysiology response to treatment. The technique may also have wider applications for assessment of baseline lobar ventilation and change in response to treatment in other pulmonary pathologies. In emphysema, lobar interventions such as lung volume reduction surgery and endo-bronchial valve placement may benefit from these techniques for assessment of lobar ventilation and also in lung cancer as a means of assessing regional-lung function pre- and post-lobectomy. Despite the correlations observed here, these findings do not make the technique of hyperpolarised gas MRI redundant; its exquisite direct visualisation of ventilation at high resolution and its non-ionizing nature make it a highly repeatable tool for addressing research questions in pulmonary physiology, and recent developments with the clinically scalable technique of ^{129}Xe MRI have helped develop its progression into clinical practice (Stewart *et al.*, 2015).

The mean absolute percentage difference of 4.0±3.3% observed in this study is larger than the 2.1% value reported previously in a smaller cohort of mild asthmatics when lobar ventilation CT was compared against SPECT (De Backer *et al.*, 2010). The larger difference here may be due to increased asthma severity (GINA 2-5 as compared to GINA 1). Although differences

were statistically significant, their low values are unlikely to be of clinical significance.

Differences in ventilation values may, however, also be attributable to several limitations in this study. Firstly, the CT model assumes lung expansion between inspiratory and expiratory states equates to ventilation whilst the ^{3}He MRI method is a more direct measure of lung-ventilation with image intensity of the ^{3}He signal being directly proportional to inhaled gas concentration in a given voxel. Secondly, despite the improvements in ^{3}He MRI to CT registration via same-breath ^{1}H MRI demonstrated here, spatial errors in registration may remain due to differences between acquisition settings in terms of patient positioning and breathing manoeuvre. ^{3}He MRI was acquired at FRC+1litre whereas inspiration-CT was acquired at TLC. Visual assessment of corresponding slices for both modalities prior to registration indicated large differences for some patients, especially at the base of the lungs where the largest amount of respiratory movement occurs. This was also demonstrated from visual evaluation of the warped ^{3}He MR images fused with anatomical-CT where overlaps in the former were observed at the base. As these regions were outside the lobar-CT masks, they were excluded from the analysis. This is consistent with quantitative results for the right and left lower lobes as shown in Figure 3.6 which demonstrates slightly less percentage lobar ventilation for ^{3}He MRI compared with CT. Furthermore, it is confirmed by the mean bias results of the Bland-Altman analysis whereby the lower and upper lobes showed negative and positive biases, respectively. Conversely, a zero bias was observed when the analysis was performed across all lobes.

Further discrepancies may also be due to transient ventilation defects (actually observed in the ^{3}He MRI in these asthmatics when repeat scanned at monthly intervals), which can be caused by a number of factors including airways opening between breath-holds; two different image modality scans were acquired on different occasions, which were typically a few days apart (Woodhouse *et al.*, 2009). This may explain some of the lobar ventilation differences seen between the CT and ^{3}He MRI; whilst patients were stable

(not scanned during exacerbation) there could be day-to-day baseline variability and time-related physiological changes.

A further limitation is that high contrast structures such as blood vessels were included in the lobar masks. Only lung parenchymal tissue contributes to ventilation and thus it is ideal for vascular structures to be segmented. Several attempts have been made to exclude vasculature from the lungs to improve voxel-based ventilation CT (Castillo *et al.*, 2010; Yamamoto *et al.*, 2011a). Pulmonary CT vessel segmentation is an active area of research and was the subject of a recent MICCAI grand challenge (VESSEL12, http://vessel12.grand-challenge.org). The results of this challenge demonstrated that when pathological abnormalities are present, even the top performing algorithms fail (van Rikxoort and van Ginneken, 2013). Similarly, vasculature regions in ^{3}He MR images due to partial volume effects were not explicitly removed in this study. These structures can be identified from ^{1}H MRI and by employing same-breath ^{3}He and ^{1}H MR acquisition techniques, vasculature can be removed directly from ^{3}He images.

Although automatic lung CT segmentation algorithms have improved significantly in recent years, the robust segmentation of the lobes still remains an open challenge. One of the challenges is delineating the lobes for patients with incomplete fissures. This has been shown to occur for a significant fraction of patients on both CT and surgical resections (24). Segmentation of the lobes was the subject of the recent LOLA11 grand challenge (www.lola11.com) and demonstrated unsatisfactory performance of participating algorithms for patients with abnormal pathologies. For our study, although commercial software was employed (Mimics; Materialise, Leuven, Belgium), manual intervention was still necessary but did not pose a significant time constraint (it took less than 5 minutes per patient to identify lobes).

3.7 Conclusion

In conclusion, this study compares percentage regional ventilation per lobe calculated with a CT model against a more direct measure of gas ventilation provided by hyperpolarised ^{3}He MRI, which although sensitive, is less clinically widespread. In so doing, we validate the CT model of ventilation which is currently clinically practicable and also demonstrate that co-registered ^{1}H MRI can be used to improve multi-modality image registration and fusion allowing the regional interpretation of ^{3}He MR images upon the underlying anatomy of the pulmonary lobes from CT.

Chapter 4
Comparison of ventilation CT and HP Gas MRI: Effects of breathing manoeuvre

Background: Image registration of lung CT images acquired at different inflation levels has been proposed as a surrogate method to map lung 'ventilation'. However, this technique requires validation against established ventilation modalities such as hyperpolarised gas MRI. Ideally, both MRI and CT would be acquired at the same inflation state. However, in practice, this is not always possible and variations in lung inflation may affect regional lung function as imaged with the two modalities.

Purpose: To evaluate the impact of lung inflation levels when comparing gas MRI and ventilation CT.

Methods: 7 asthma patients underwent breath-hold CT at total lung capacity (TLC) and functional residual capacity (FRC). In addition, two sets of ^{3}He MRI were acquired; at FRC+1L and TLC. In the same breath as ^{3}He MRI, ^{1}H MRI was also acquired. For the ventilation CT calculation, FRC-CT was registered to TLC-CT. Next, TLC and registered FRC-CT was used to compute a surrogate ventilation image from voxel-wise intensity differences in Hounsfield unit values. The ventilation surrogate was then thresholded to 10-100% percentiles and 20-100% percentiles which were assumed to be ventilated. For direct comparison of CT and ^{3}He MRI ventilation, FRC+1L and TLC ^{3}He MRI were registered to TLC-CT indirectly via the corresponding same-breath ^{1}H MRI data. To test for variations in FRC+1 and TLC ^{3}He MRI, the percentage ventilated volume was calculated for each patient by taking the ratio of binary segmented ^{3}He MRI and TLC-CT volumes. For ^{3}He MRI and CT ventilation comparison, Dice overlap coefficients were computed separately for the binary segmentation of ventilation CT with that of FRC+1L and TLC ^{3}He MRI. Statistical significance of differences was tested using the Wilcoxon signed-ranks.

Results: The median (range) of percentage ventilation volumes for FRC+1 and TLC ^{3}He MRI were 0.81 (0.47-0.91) and 0.89 (0.72-0.92) respectively, p=0.042. For MRI versus CT ventilation comparison, statistically significant improvements in Dice coefficients were observed for TLC ^{3}He MRI compared with FRC+1 with median (range) values of 0.93 (0.86-0.93) and 0.86 (0.68-0.92) respectively, p=0.017, for the 10-100th percentile and 0.87 (0.83-0.88) and 0.81 (0.66-0.87) respectively, p=0.027, for the 20-100th percentile. Statically significant

improvements in Dice coefficients were overserved with the 10-100th percentile ventilation CT masks for both FRC+1L ^{3}He MRI ($p = 0.026$) and TLC ^{3}He MRI ($p = 0.017$) compared with the 20-100th percentile.
Discussion: Both visual evaluation and quantitative analysis of ^{3}He MRI demonstrated increased ventilation at TLC compared with FRC+1L. In several cases, ventilation defects depicting airway closures at FRC+1 were opened at TLC. Inflation related induced variations in ventilation led to improved spatial agreement of CT ventilated volumes at TLC.
Conclusion: This study demonstrates that comparison of ventilation CT and HP gas MRI varies with HP gas inflation state. If CT is acquired at FRC and TLC, a higher correlation with HP gas ventilation imaging can be achieved if the latter is acquired at TLC.

4.1 Preface

The material in this chapter was originally presented at the 7th International Workshop in Pulmonary Functional Imaging. Additional material is also included here which could not be included in the proffered presentation.

> Tahir BA, Marshall H, Vos W, Hartley R, Siddiqui S, Brightling CE, Ireland RH, Wild JM. Comparison of ventilation CT and HP Gas MRI: Effects of breathing manoeuvre. 7th International Workshop on Pulmonary Functional Imaging (IWPFI), Edinburgh, Scotland (2015)

4.2 Introduction

The primary function of the mammalian respiratory system is gas exchange of which ventilation is an essential component. Although normal lungs exhibit a degree of ventilation heterogeneity (Crawford *et al.*, 1985), a marked increase has been shown in patients with respiratory diseases (Mugler *et al.*, 2010). In current clinical practice, ventilation is normally evaluated using global measures of lung function. The regional nature of respiratory diseases, however, requires imaging techniques which are able to visualise and quantify the spatially varying extent of ventilation. Image registration of non-contrast CT images acquired at just two different inflation levels has been proposed as a surrogate method to map lung 'ventilation', based on the assumption that lung expansion and change in lung signal intensity of a given unit equates to ventilation (Guerrero *et al.*, 2005). However, this technique requires validation against established ventilation modalities. Initial work has indicated the potential for clinically validating ventilation CT against a more direct measure of gas ventilation such as hyperpolarised gas MRI (Mathew *et al.*, 2012). However, hyperpolarised gas MRI has been shown to be sensitive to inflation state (Halaweish *et al.*, 2013). In one study, marked decreases in the ventilation of elite divers were demonstrated at subresidual volumes (Muradyan *et al.*, 2010).

CT-based surrogates of ventilation have been shown to be sensitive to a range of factors including image registration parameters (Yamamoto *et al.*, 2011b) and ventilation metric (Castillo *et al.*, 2010). Previously, Mistry *et al.* (2013) evaluated the effects of different breathing manoeuvres during CT imaging and observed marked differences in the distribution of the computed CT ventilation images. However, to date, CT-based surrogates of ventilation have never been compared against an established ventilation imaging modality acquired at different inflation states.

The primary aim of this study was to evaluate the impact of inflation levels when CT based surrogates of ventilation are compared against an established measure of regional ventilation. To this end, we employed ^{3}He hyperpolarised

MR static ventilation imaging acquired at two lung volumes, namely, FRC+1L and TLC, and performed spatial overlap comparison between each inflation state and the CT ventilation surrogate. A secondary aim was to evaluate the differences in ^{3}He ventilation with inflation state.

4.3 Methods

4.3.1 Asthma subjects

7 asthma patients with sputum eosinophilia and moderate-to-severe asthma were recruited to this study. The inclusion criteria were greater than 18 years of age, physician diagnosis of asthma, currently on GINA step 2 to 5 asthma therapies, sputum eosinophil count greater than or equal to 2%. The exclusion criteria included other acute illnesses, recent or current lower respiratory tract infection, contra-indication to MRI, BMI <17 or >40 kg/m^2, women of child-bearing potential. The characteristics of these patients can be found in Table **4.1**.

Table 4.1 Summary of patient characteristics and lung function parameters.

	Age	Sex	FEV_1 (L)	Predicted FEV_1 (%)	FVC (L)	Predicted FVC (%)	FEV_1/FVC (%)
1	41	Male	3.35	89.10	4.88	107.05	68.65
2	51	Female	0.80	33.81	1.75	62.87	45.71
3	45	Male	3.85	104.42	5.70	126.32	67.54
4	64	Female	2.10	107.03	2.90	123.05	72.41
5	62	Male	2.30	69.21	4.60	108.41	50.00
6	52	Female	2.10	99.81	2.81	112.78	74.73
7	42	Male	3.30	99.97	4.25	107.41	77.65
Mean	51	N/A	2.54	86.19	3.84	106.84	65.24
SD	9.20	N/A	1.03	26.40	1.39	20.87	12.42

Note: FEV_1 = forced expiratory volume in the first second of expiration, FVC = forced vital capacity, L = litres. Predicted FEV_1 and FVC were calculated by dividing the FEV_1 and FVC values by their respective mean value for any person of similar age, sex and body composition.

4.3.2 Image acquisition

All patients underwent CT, MRI and pulmonary function tests (PFTs). PFTs and CT were performed on the same day. MRI was performed within 6 days of the PFTs and CT with a mean±SD interval of 1.5±0.8 days and range of 1 to 4 days.

Breath-hold CT scans were acquired at total lung capacity (TLC) and functional residual capacity (FRC) on a Sensation 16 scanner (Siemens, Forchheim, Germany). The following CT settings were used: tube voltage, 120kV; tube current, 120mAs; rotation time, 0.5s; pitch, 1.5. Where available, a B30f reconstruction kernel was used or the next kernel closest to it (e.g. B35f, B60 etc.). CT in-plane resolution was approximately 0.86×0.86mm with a pixel matrix of 512×512. CT slice thickness was 1 mm with approximately 600 slices for each patient.

^{3}He MR ventilation images were acquired at two inflation states, FRC+1L and TLC. In the same breath-hold as ^{3}He MRI, anatomical ^{1}H MR images were also acquired using methods developed for same-breath imaging of two nuclei on a GE HDx 1.5T whole body MRI system (GE Healthcare, Princeton, NJ, USA) (Wild *et al.*, 2011). For the ^{3}He MR ventilation images acquired at FRC+1L, patients exhaled to FRC and then inhaled a mixture of 350ml ^{3}He and 650ml N_2. For the ^{3}He MR ventilation images acquired at TLC, patients exhaled to FRC and then inhaled a mixture of 400ml ^{3}He and 600ml N_2 followed by inhalation of room air until TLC was reached. The increase in ^{3}He dose was to account for the gas dilution with increase in lung volume at TLC. Ventilation images at TLC were acquired within six minutes of that of FRC+1L.

Helium was polarised on-site to approximately 25% using a rubidium spin exchange polariser (GE Healthcare, Amersham, UK). A transmit-receive quadrature ^{3}He vest coil (Clinical MR Solutions, Brookfield, WI, USA) was used to acquire ^{3}He-images with the following sequence; 2D spoiled gradient-echo, 3x3mm in-plane resolution, 10mm slice thickness, 38.4cm field of view, 1.1ms echo time, 3.6ms repetition time, 8º flip angle, 62.5kHz bandwidth and

full lung coverage (20 to 24 slices). Same-breath ^{1}H images (Wild *et al.*, 2011) with the same slice thickness were acquired using the ^{1}H transmit-receive body coil of the scanner with the following sequence; 2D steady state free precession, 3x6mm in-plane resolution, 38.4cm field of view, 0.7ms echo time, 2.4ms repetition time, 50º flip angle, and 167kHz bandwidth.

4.3.3 Image segmentation

Medical image segmentation software (Mimics; Materialise, Leuven, Belgium) was used to segment the lungs of the inspiratory and expiratory CT scans. The ^{3}He MR images were segmented in Slicer 4 (Fedorov *et al.*, 2012) by defining a manual-threshold value in a patient specific way by visual inspection and manually removing the large airways including the trachea.

4.3.4 Ventilation CT computation

For the ventilation CT calculation, FRC-CT was registered to TLC-CT using the optimised script detailed in Appendix A. Next, TLC and registered FRC-CT was used to compute a surrogate ventilation image from voxel-wise intensity differences in Hounsfield unit values based on a modified version of the original formulation of Guerrero *et al.* (2005) to account for the computation being performed in the inhalation CT spatial domain:

$$\frac{\Delta V}{V_{exp}} = 1000 \frac{HU_{ins} - \overline{HU}_{exp}}{\overline{HU}_{exp}(1000 + HU_{ins})}$$

where $\overline{HU}_{exp}$ is the average HU of the voxels in the moving deformed expiration image which spatially correspond to the voxels in the fixed inspiration image and HU_{insp} is the HU of the inspiratory voxel. The metric purports to be a measure of change in fractional content of air per voxel between respiratory phases.

4.3.5 Spatial overlap comparison

For direct comparison of CT and ^{3}He MRI ventilation, FRC+1L and TLC ^{3}He MRI were registered to TLC-CT indirectly via the corresponding same-breath ^{1}H MRI using the indirect diffeomorphic method described in Chapter 2. To test for variations in FRC+1 and TLC ^{3}He MRI, the percentage ventilated volume was calculated for each patient by taking the ratio of the binary lung segmentations of ^{3}He MRI and TLC-CT.

For the ^{3}He MRI and CT ventilation spatial overlap analysis, the ventilation CT surrogate image needed to be segmented. Here, we employed the percentile threshold technique used in several seminal studies (Castillo *et al.*, 2010; Castillo *et al.*, 2012) to discern ventilated from non-ventilated lung. To assess the effect of using different percentile values, we thresholded the ventilation CT surrogated to the 10-100th and 20-100th percentile ranges which were assumed to be ventilated. Dice overlap coefficients were computed separately for the binary segmentations of both ventilation CT percentiles with that of FRC+1L and TLC ^{3}He MRI. The workflow for the comparison method of FRC+1 and TLC ^{3}He MRI with ventilation CT is shown in Figure 4.1.

4.3.6 Statistical analysis

Statistical analysis was performed by using IBM SPSS software (version 20.0; Chicago, Il, USA). A p value less than 0.05 was considered statistically significant. The Wilcoxon signed-ranks test was used to test statistical significance in differences.

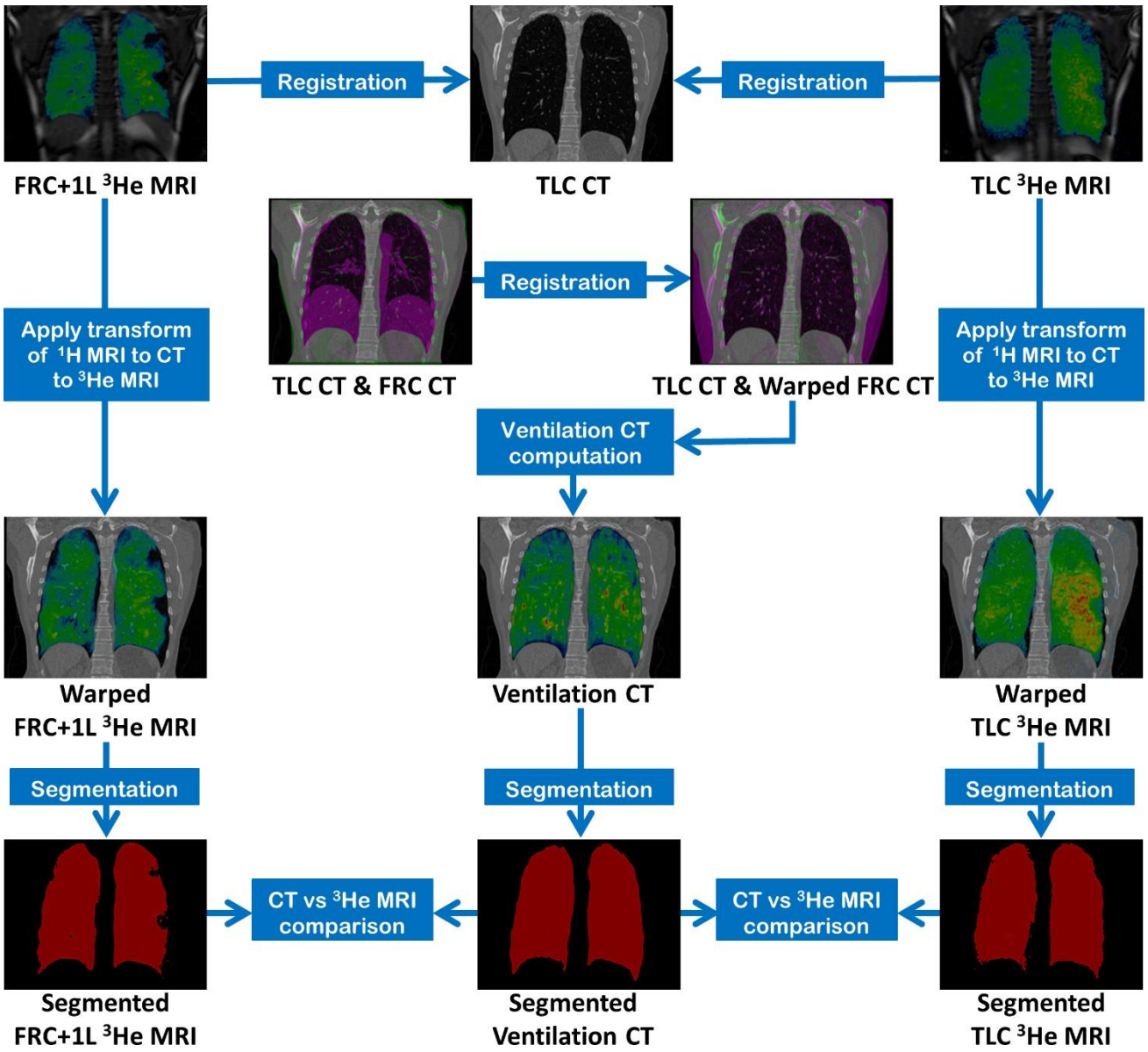

Figure 4.1 Workflow for comparison of FRC+1 and TLC ^{3}He MRI with Ventilation CT.

4.4 Results

4.4.1 FRC+1L versus TLC ^{3}He MRI

All patients complied with the imaging procedures and were able to perform breath-holds at both FRC+1L and TLC. TLC ^{3}He MRI exhibited increased and more homogenous ventilation than FRC+1L ^{3}He MRI. Frequently, defects observed at FRC+1L would either partially or completely resolve at TLC. The spatial extent and location of these ventilation defects were confirmed by same-breath anatomical ^{1}H MRI as shown in Figure 4.2. As can be seen from the figure, ^{3}He MRI acquired at TLC also exhibited reduced trachea gas depositions of ^{3}He consistent with the opening of airways at the higher inflation state. The median (range) of percentage ventilation volumes for FRC+1L and TLC ^{3}He MRI were 0.81 (0.47-0.91) and 0.89 (0.72-0.92) respectively, p=0.042. This is also displayed graphically as a box plot in Figure 4.3.

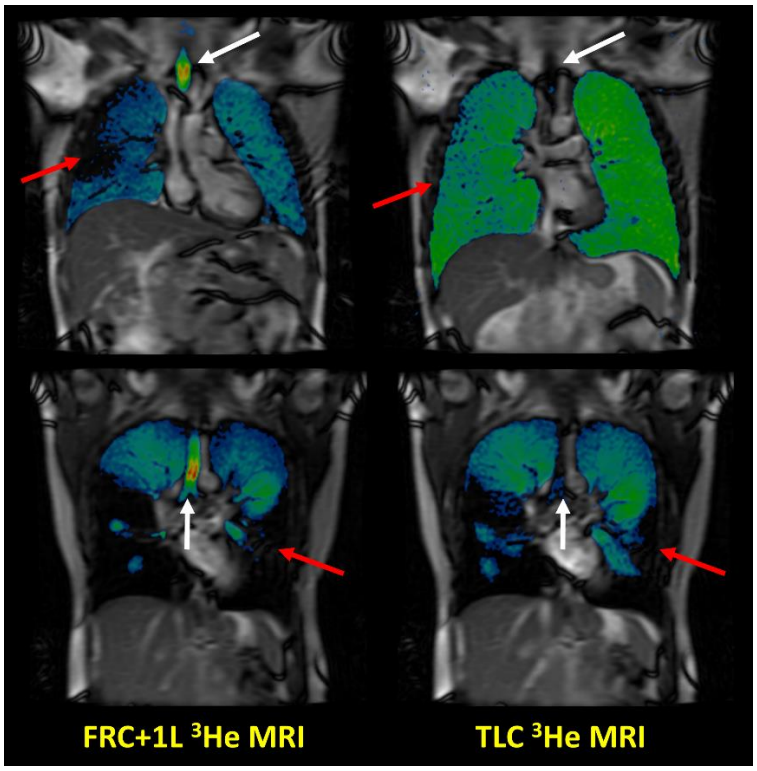

Figure 4.2 Corresponding coronal slices of patient 1 (top) and 2 (bottom) showing ^{3}He MRI acquired at FRC+1L (left) and TLC (right) fused with same-breath anatomical ^{1}H MRI. Several ventilation defects observed at FRC+1L resolve at TLC (red arrows). Similarly, a marked reduction in trachea gas depositions of ^{3}He can be observed at TLC (white arrows), indicating increased airway opening at the higher inflation state.

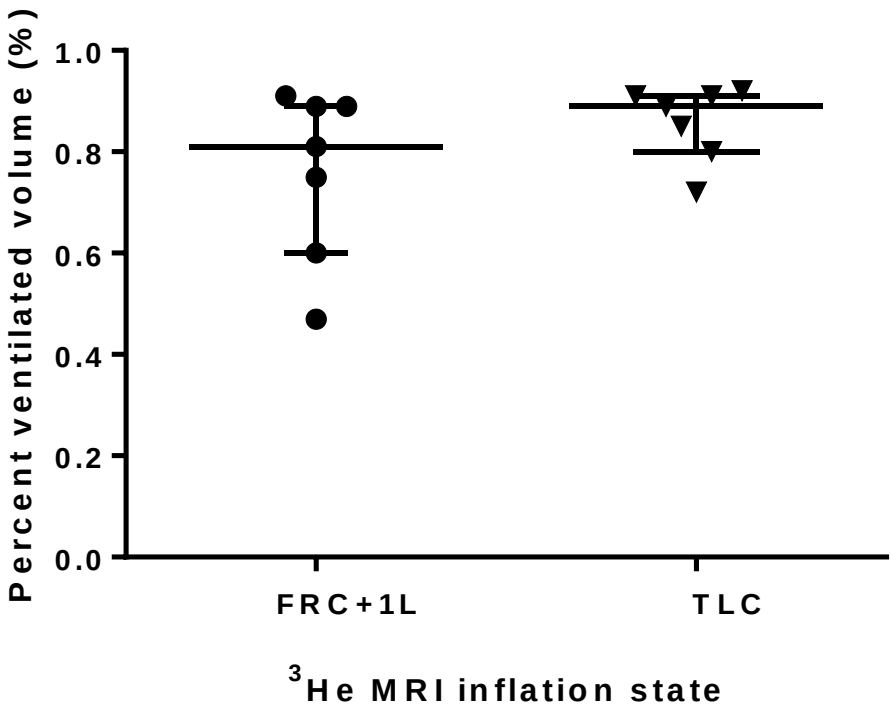

Figure 4.3 Box plot of dice coefficients of ventilation CT with ^{3}He MRI acquired at FRC+1 and TLC. Individual data points are shown for all patients along with the median and interquartile range across inflation state.

4.4.2 Ventilation CT vs FRC+1L and TLC ^{3}He MRI

Figure 4.4 shows corresponding coronal slices of registered FRC+1L and TLC ^{3}He MRI and ventilation CT for a representative patient. The ventilation CT image is visually more similar to that of TLC ^{3}He MRI. This was confirmed by quantitative spatial overlap results whereby statistically significant improvements in Dice correlation coefficients were observed for TLC ^{3}He MRI compared with FRC+1L with median (range) values of 0.93 (0.86-0.93) and 0.86 (0.68-0.92) respectively, p=0.017, for the 10-100th percentile and 0.87 (0.83-0.88) and 0.81 (0.66-0.87) respectively, p=0.027, for the 20-100th percentile. Statically significant improvements in Dice coefficients were observed with the 10-100th compared with the 20-100th percentile ventilation CT masks for both FRC+1L (p = 0.026) and TLC ^{3}He MRI (p = 0.017). The results for each patient are displayed in **Table 4.2** and shown in graphically in Figure 4.5.

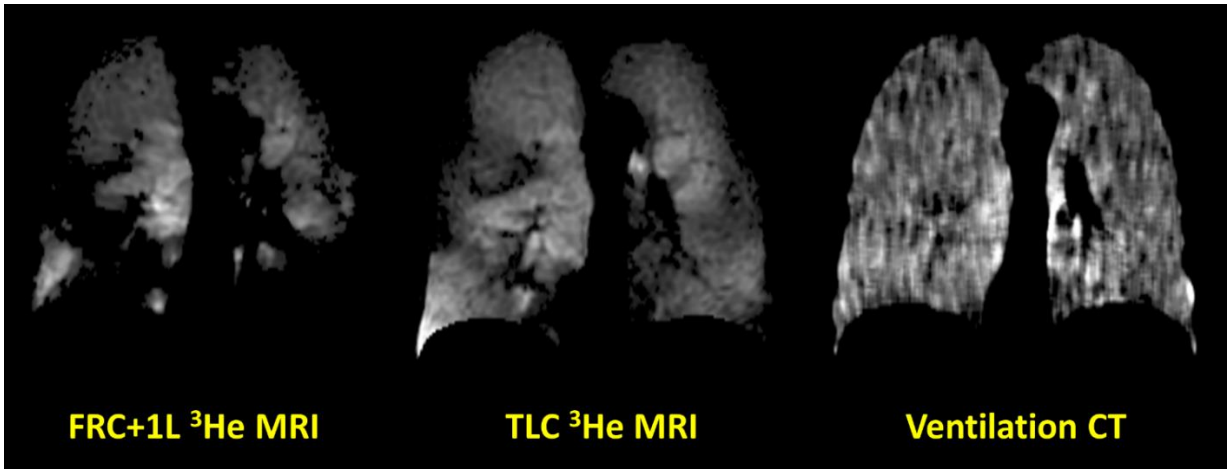

Figure 4.4 Corresponding coronal slices for a representative patient of registered FRC+1L and TLC ^{3}He MRI and ventilation CT.

Table 4.2 Dice correlation coefficients for ventilation CT thresholded at two different percentile ranges with FRC+1L and TLC ^{3}He MRI.

	10 to 100% percentile		20 to 100% percentile	
Patients	FRC+1L	TLC	FRC+1L	TLC
1	0.86	0.93	0.81	0.87
2	0.78	0.86	0.78	0.84
3	0.92	0.93	0.87	0.88
4	0.92	0.93	0.87	0.87
5	0.68	0.87	0.66	0.83
6	0.92	0.93	0.86	0.87
7	0.85	0.91	0.81	0.86
Mean±SD	0.85±0.09	0.91±0.03	0.81±0.07	0.86±0.02
Median (range)	0.86 (0.68-0.92)	0.93 (0.86-0.93)	0.81 (0.66-0.87)	0.87 (0.83-0.88)
P value	0.017		0.027	

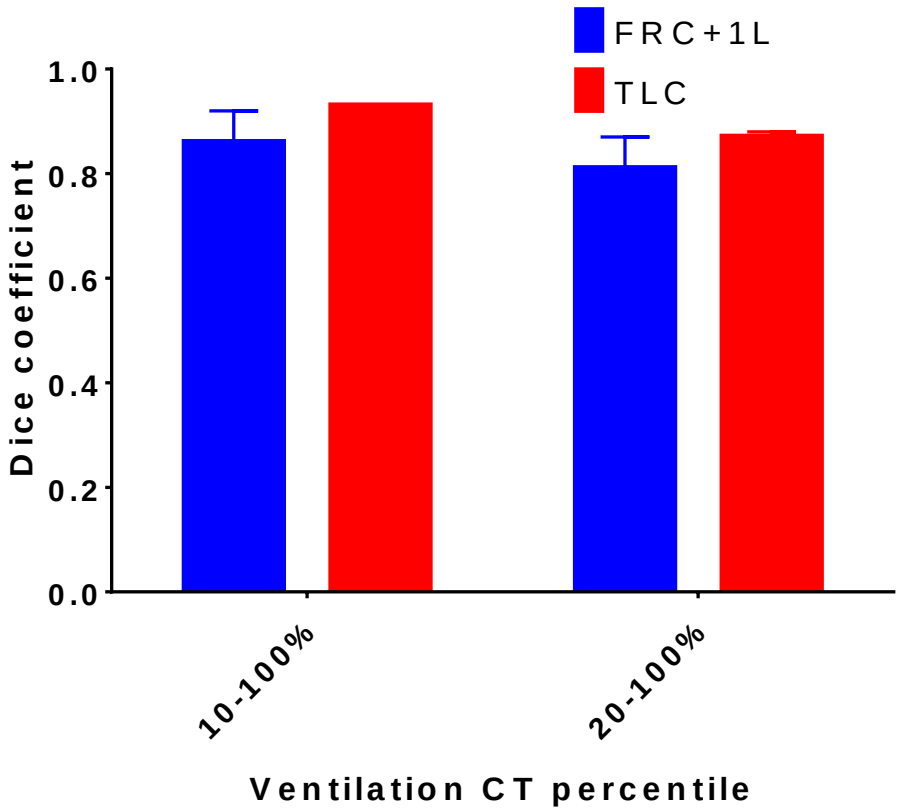

Figure 4.5 Bar graph of Dice coefficients of ventilation CT thresholded at the 10-100th and 20-100th percentiles against ^{3}He MRI acquired at FRC+1L and TLC. The data is summarised with median and upper limit of the range (small bar). The median is equivalent to the upper limit of the range for the Dice coefficients of the 10-100th ventilation CT percentile and TLC ^{3}He MRI.

4.5 Discussion

Seven adults with asthma were evaluated in the first study to assess the impact of comparing CT-based surrogates of ventilation with an established ventilation modality acquired at multiple inflation levels. To this end, we acquired ^{3}He ventilated weighted images at FRC+1L and TLC and CT at FRC and TLC and observed the following findings:

a. ^{3}He MRI exhibited increased and more homogenous ventilation at TLC;
b. several ventilation defects observed at FRC+1L either completely or partially resolved at TLC;
c. higher correlation of CT ventilation with HP gas ventilation imaging acquired at TLC.

4.5.1 Effect of lung inflation state on distribution of ventilation

Both visual evaluation and quantitative analysis of ventilation-weighted ^{3}He MRI demonstrated more homogenous ventilation at TLC compared with FRC+1L. In several cases, ventilation defects observed at FRC+1L resolved completely at TLC. This was confirmed by quantitative results where we observed statistically significant improvements in percent ventilated volumes at the higher inflation state. Several mechanisms may account for these observations. As lung inflation increases, the increased ventilation homogeneity observed may be attributable to increases in airway diameter. Brown and Mitzner (1996) used high resolution CT to quantify the effect of lung inflation on airway diameter in canine subjects and observed significant increases in airway diameter at increased inflation levels. Thus, airways that were narrowed or closed at FRC+1L could have opened at the higher inflation state, inducing some of the resolved ventilation defects observed in this study. The increased dilation of airways at the higher inflation state could have increased the volume of aerated parenchyma, and thus ventilated volume. The marked increase in retention of ^{3}He gas in the trachea at the lower inflation state observed in the subjects in this study supports this finding.

The results of this study are consistent with other findings suggesting potential bronchodilatory effects of deep inspiration (Scichilone and Togias, 2004). Deep inspirations may enable distribution of gas to hypoventilated regions affected by narrowed or closed airways. Although a degree of ventilation heterogeneity is observed in normal subjects in the form of a vertical gradient due to gravity and other effects, these effects are significantly reduced at TLC where homogenous ventilation is observed (Milic-Emili, 2011). Such improvements in ventilation were not observed in this study for all ventilation defects, demonstrated by the fact that the percent ventilated volume at TLC was still lower than 100%, despite exhibiting statistically significant improvements from FRC+1L. As such, numerous defects observed at FRC+1L persisted at TLC. Thus, other factors may have a greater impact on the formation of ventilation defects in asthma including small and large airway closure due to airway inflammation, obstruction and remodelling (Brightling *et al.*, 2012). Importantly, inflammation in the airway smooth muscle bundles has been shown to be a key factor contributing to impaired airway dilation of asthmatics during deep inspiration (Slats *et al.*, 2007).

4.5.2 Impact of ^{3}He MR inflation level on correlation with CT ventilation

Acquisition of CT at multiple inflation levels and computation of density differences of the deformably registered images have been proposed as a surrogate method for generating regional ventilation (Guerrero *et al.*, 2005). This study sought to quantify the spatial overlap of these surrogates with that of an established ventilation modality, namely, hyperpolarised ^{3}He MRI, acquired at two different lung inflation levels. Using the Dice coefficient, statistically significant improvements in overlap for ^{3}He MRI acquired at the higher inflation level were observed. A possible explanation for this result might be attributable to the CT acquisition protocol for this study. The CT-based surrogates of ventilation purport to be measures of the local change in air volume between two lung inflation states whilst static ventilation-weighted ^{3}He MR images represent a snapshot of the distribution of ^{3}He from FRC up to a given inflation level. Accordingly, the CT-based surrogates were derived from breath-hold CT acquired at FRC and TLC and thus represent local

volume change between these two inflation levels which would more closely depict the distribution of ^{3}He gas at TLC.

The findings of this study not only imply the importance of careful volumetric control of lung inflation for ventilation CT validation studies but also for longitudinal studies to monitor disease progression and treatment response. It is essential, therefore, that consistent breathing manoeuvres are employed as variations can alter the ventilation distributions.

4.5.3 Study limitations

This study has several limitations. Firstly, a relatively small number of patients were studied. Furthermore, this study only included patients with asthma. Thus, caution must be exercised when extending these results to other respiratory diseases. For example, although improved airway distention has been observed in asthma, albeit to a lower degree than normal subjects (Jensen *et al.*, 2001), comparisons of the effect of deep-inspiration induced changes in airway response between asthma and COPD patients indicate that bronchodilatory effects are impaired in the latter disease (Slats *et al.*, 2007). Therefore, a larger scale study of the effect of inflation level as measured by ^{3}He MRI and its impact on spatial correlation with CT-based ventilation in other respiratory diseases is warranted.

For determination of CT ventilated volume, there exists some possibility for erroneous segmentation. Here, we employed two percentile ranges and observed that the 10-100th functional percentile range exhibits greater correlation than that of the 20-100th range. This indicates that a larger number of voxels representing ventilation defects occupy the lower percentile band, thus leading to greater correlation for the 10-100th range. Nonetheless, our results suggest that spatial correlation is sensitive to CT ventilation segmentation technique.

The Dice coefficient also provides a measure of overlap between two binary segmentations and does not account for subtler differences in the intensity

distributions within the boundaries of these segmentations. A more robust method of comparing the images would be to perform voxel wise spatial correlations as has been performed for Galligas PET and CT ventilation which are acquired on the same scanner (Kipritidis *et al.*, 2014). However, significant differences in acquisition settings discussed in Chapter 2 precluded us from performing a meaningful voxel wise or regional correlation. As will be demonstrated in the following chapter, an improved acquisition strategy can mitigate these limitations.

For ^{3}He MRI, patients inhaled the noble gas from a starting point of FRC until they reached the desired inflation level. Inhalation from residual volume has been shown to provide different gas distributions and may provide different correlation results (Milic-Emili *et al.*, 1966). Similarly, CT breathing manoeuvre has been shown to alter the resulting ventilation distribution (Mistry *et al.*, 2013). In this study, we did not acquire CT at FRC+1L. Given our findings, we hypothesise that CT acquired at FRC and FRC+1L will lead to ventilation surrogates more closely matched with that of ^{3}He acquired at FRC+1L compared with ventilation computed from CT acquired at FRC and TLC.

4.6 Conclusion

This study demonstrates that comparison of ventilation CT and HP gas MRI varies with HP gas inflation state. If CT is acquired at FRC and TLC, a higher correlation with HP gas ventilation imaging can be achieved if the latter is acquired at TLC.

Chapter 5
An image acquisition and analysis strategy for spatial comparison of ventilation CT with ^{3}He and ^{129}Xe MRI

Introduction: Previous ventilation CT versus HP Gas MRI work has compared the spatial overlap of binary thresholded images from both modalities by the dice overlap coefficient. Such overlap measures provide a global comparison and thus voxel-wise or region of interest (ROI) analysis may improve the comparison by assessing the correlation of the intensity distribution of corresponding regions within the binary segmentations. Although hyperpolarised gas imaging with ^{3}He has demonstrated superb visualisation of pulmonary airspaces, due to the limited and unpredictable global supplies of ^{3}He, ^{129}Xe has begun to play a more important role in recent years. To date, no published study has investigated the spatial correlation of ventilation CT against ^{129}Xe MRI.

Purpose: To develop an image acquisition and analysis strategy to facilitate direct spatial correlation of ventilation CT with both hyperpolarised ^{3}He and ^{129}Xe MRI. The method was tested with a cohort of lung cancer patients.

Methods: 5 patients underwent expiratory and inspiratory breath-hold CT. ^{129}Xe and ^{1}H MRI were also acquired at the same inflation state as inspiratory CT. This was followed immediately by acquisition of ^{3}He & ^{1}H MRI in the same breath and at the same inflation state as inspiratory CT. Expiration CT was deformably registered to inspiration CT for calculation of ventilation CT from three ventilation metrics. Inspiration CT and the ^{129}Xe MRI's corresponding anatomical ^{1}H MRI were registered to ^{3}He MRI via the same-breath anatomical ^{1}H MRI. Spatial correlation was assessed by computing the voxel-wise Spearman correlation coefficients between each ventilation CT image and its corresponding ^{3}He/^{129}Xe MR image and for the median values in corresponding regions of interest (ROIs), ranging from finer to coarser in-plane dimensions of 5x5, 10x10, 15x15 and 20x20, located within the lungs as defined by the same-breath ^{1}H MRI lung mask. As a secondary analysis in order to establish scan-to-scan similarity between ^{3}He and ^{129}Xe MRI, Spearman coefficients were assessed at the voxel-level and for the same ROIs detailed above.

Results: Several interesting results were observed from the data; the spatial correlations between all ventilation CT metrics, ^{3}He and ^{129}Xe MRI increase with more coarsely defined ROIs and start to reach a plateau for ROIs of 15x15 voxels. Furthermore, a marked increase in Spearman correlation was observed for ^{3}He and ^{129}Xe MRI in contrast to when ventilation CT was compared with either ^{3}He and ^{129}Xe MRI.
Conclusion: This work demonstrates direct spatial comparison of ventilation from CT and hyperpolarised gas MRI (^{3}He and ^{129}Xe MRI). Initial results exhibit moderate correlation between ventilation CT and hyperpolarised gas MRI, which improves for coarser regions. Discrepancies could be attributable to a number of factors including non-ventilatory effects due to blood volume changes between inflation states which are not accounted for in the model, the inherent noise in CT intensity, and registration errors at the voxel-level. Thus, it may be more beneficial to quantify ventilation at a more regional level.

5.1 Preface

The material in this chapter was originally presented at several conferences. Additional material is also included here that could not be included in the proffered presentations.

Tahir BA, Marshall H, Hart KA, Swinscoe JA, Hatton MQ, Wild JM and Ireland RH. Ventilation CT: Voxel-level comparison with hyperpolarised Helium-3 & Xenon-129 MRI. American Association of Physicists in Medicine Annual Meeting, Washington DC, USA (2016)

Tahir BA, Marshall H, Hart KA, Swinscoe JA, Wild JM, Ireland RH and Hatton MQ. CT-based surrogates of pulmonary ventilation in lung cancer: A voxel-level comparison with HP gas MRI. World Conference on Lung Cancer, Vienna, Austria (2016)

Tahir BA, Marshall H, Hart KA, Swinscoe JA, Hatton MQ, Wild JM and Ireland RH. Ventilation CT: Voxel-level comparison with HP gas MRI. European Respiratory Society International Congress, London, UK (2016)

Tahir BA, Marshall H, Hart KA, Swinscoe JA, Hatton MQ, Wild JM and Ireland RH. An image acquisition and analysis strategy for comparison of ventilation CT and HP gas MRI. 7th International Workshop on Pulmonary Functional Imaging, Edinburgh, Scotland (2015)

5.2 Introduction

Image registration of pulmonary CT images acquired at different inflation levels has been proposed as a potential method of mapping regional ventilation without the use of a contrast agent. It is based on the assumption that lung expansion and density changes of corresponding parenchymal voxels equate to ventilation (Guerrero *et al.*, 2005). However, its physiological accuracy has yet to be validated prior to widespread clinical use. Thus, a central focus of enquiry in the field of CT-based ventilation investigations has been the validation of the modality against more established measures of pulmonary function. Comparing CT ventilation-derived metrics such as defective lung volumes and coefficients of variation with global measurements of spirometry, moderate correlations between FEV_1 and FEV/FVC, ranging from 0.43 to 0.73 and 0.38 to 0.73 for the intensity and Jacobian metrics have been reported, respectively (Brennan *et al.*, 2015; Yamamoto *et al.*, 2014). In animal experiments, CT-based ventilatory surrogates have demonstrated both a reasonably high level (Jacobian metric, linear regression = 0.73, Reinhardt *et al.* 2008; intensity metric, correlation coefficient = 0.66, Fuld *et al.* 2008; hybrid metric, correlation coefficient = 0.82, Ding *et al.* 2012) and relatively low level (geometric metric, Spearmans coefficient = 0.44, Zhang *et al.* 2016) of correlation with contrast enhanced xenon CT. However, the subjects were mechanically ventilated and the Xenon-CT used had limited axial coverage thus limiting its ability to provide a validation over the full lung volume. Recently, a high correlation of 0.89 ($p<0.0001$) has been observed in rats against Cryomicrotome imaging after exposure to aerosols of 1μm fluorescent microspheres (FMS) (Jacob *et al.*, 2015). However, the ground truth image requires ex-vivo dissection of the lung prohibiting its use in human subjects.

In light of these difficulties, the vast majority of validation studies in humans have compared the technique against nuclear medicine-based imaging using both planar and tomographic configurations, with conflicting results reported in the literature (dice coefficient = 0.35, Castillo *et al.* 2010; dice coefficient = 0.39, Yamamoto *et al.* 2014; correlation coefficient = 0.66, Vinogradskiy et al. 2014). Although regional lung function has traditionally been assessed by

nuclear imaging, it suffers from poor accuracy, spatial and temporal resolution and aerosol depositions in defect regions (Petersson *et al.*, 2007) and is thus not the optimal modality for a valid comparison.

The efficacy of ventilation-based nuclear imaging can be improved by position emission tomography (PET) by inhalation of Gallium-68 carbon nanoparticles, commonly referred to as Galligas, and has shown moderate correlations with 4D-CT (Kipritidis *et al.*, 2016; Kipritidis *et al.*, 2014). However, although the image data of these studies were acquired to enable improvements over ventilation CT vs SPECT studies with 4D-CT acquired at the same session and couch as PET, inherent discrepancies in image acquisition settings still remained. In general, the PET Galligas ventilation images in those studies were acquired over a minimum time scale of 10 minutes to ensure sufficient accumulation of the tracer, increasing for poor inhalations or low administered doses (Callahan *et al.*, 2014). By contrast, 4D-CT is acquired over a single tidal breath. Such differences may reduce spatial correlations between the two modalities.

Hyperpolarised gas MR imaging is an alternative technique to nuclear imaging that can provide exquisite images of ventilation with superior spatial resolution, without the use of ionising radiation. Furthermore, it possesses improved temporal resolution to enable image acquisition in a single breath-hold. Gas MRI has been applied to the study of many respiratory diseases including lung cancer (Ireland *et al.*, 2007a) and is a viable candidate as a reference modality.

Previously, Mathew *et al.* (2012) evaluated the spatial correspondence of 4D-CT ventilation derived from the intensity based metric with ^{3}He MRI for eleven lung cancer patients. However, this work had several methodological limitations. Firstly, the image acquisition protocol was not optimised to minimise potential discrepancies between the two modalities; the two different scans were acquired at a mean interval of 1.5 weeks for each patient and thus some of the regional ventilation differences in their study could be attributable to disease progression and time-related physiological differences. Furthermore, differences in patient positioning (treatment planning couch vs

diagnostic MRI couch) and breathing manoeuvre (inspiratory breath-hold vs tidal breathing) were not explicitly accounted for, potentially leading to differences in the imaged physiologic states and registration errors. Ireland *et al.* (2008) demonstrated significant improvements in rigid registration by reproducing the same breath-hold and body positions during image acquisition of CT and ^{3}He MRI. Secondly, only fiducial anatomical landmark affine registration was used to ensure the CT ventilation and HP gas images were in the same spatial domain without accounting for deformable differences between the two images, owing to postural differences. Thirdly, only ventilation derived from an intensity metric was evaluated in this study with no reference to other prominent metrics such as the determinant of the Jacobian which provides a measure of local lung expansion. Fourthly, the assessment of spatial correlation was limited to comparing the spatial overlap of binary thresholded images from both modalities by the dice overlap coefficient. Such overlap measures provide a more global comparison and thus voxel-wise and region of interest (ROI) analysis may improve the comparison by assessing the correlation of the intensity distribution of corresponding regions within the binary segmentations.

Although hyperpolarised gas imaging with ^{3}He has demonstrated superb visualisation of pulmonary airspaces, due to the limited and unpredictable global supplies of ^{3}He, ^{129}Xe has begun to play a more important role in recent years (Patz *et al.*, 2007). To date, no published study has investigated the spatial correlation of the CT-based ventilation technique against ^{129}Xe MRI. Similarly, although a number of studies have emerged in the past few years comparing ^{3}He and ^{129}Xe MR techniques for imaging ventilation (Svenningsen *et al.*, 2013) and microstructure (Kirby *et al.*, 2013), only global means of comparison such as the percent ventilated volume have been used and voxel-wise and more regional forms of analysis are yet to be performed.

The aim of this study was to develop and apply a novel image acquisition and analysis strategy to facilitate direct spatial correlation of ventilation CT with hyperpolarised gas imaging. A secondary aim of the study was to assess the effect of the hyperpolarised gas on the spatial correlation and thus both

hyperpolarised ^{3}He & ^{129}Xe MRI were compared to ventilation CT. The image acquisition and analysis strategy developed was tested in a cohort of lung cancer patients.

The key novel aspects of this work are:

(i) It is the first validation of ventilation CT generated from breath-hold (rather than 4D-CT) inspiratory and expiratory CT against hyperpolarised gas MRI.
(ii) It is the first such study to include validation data from both of the two key hyperpolarised noble gases for pulmonary ventilation imaging, namely, ^{3}He and ^{129}Xe.
(iii) It presents a novel imaging protocol for acquiring pulmonary CT, ^{1}H, ^{3}He and ^{129}Xe MRI with similar breath-holds and posture such that registered data can be used to facilitate direct spatial comparison of CT ventilation and HP gas ventilation maps via deformable image registration.
(iv) It presents the first voxel-wise and ROI based (rather than binary segmentation based overlap) comparison of ventilation CT and HP gas MRI.

5.3 Methods

5.3.1 Patients

Seven patients provided written consent to enrol on this prospective, single-arm, single-institutional clinical study, approved by the institutional review board (Lung HeXeRT, ClinicalTrials.gov: NCT01859650). Patients were eligible for participation if they had a multidisciplinary team diagnosis of non-small cell lung cancer (NSCLC) based on findings of positive histology, positive PET scan or growth on serial CT scan requiring CT planning for radiotherapy treatment. Ineligibility criteria included an age less than 18 years, inability to undergo MRI and co-morbid conditions that exclude radiotherapy treatment.

5.3.2 CT image acquisition

In addition to their routine free breathing treatment planning scan, all patients underwent expiration and inspiration breath-hold CT at functional residual capacity (FRC) and FRC+1L, respectively, on a 16-slice Lightspeed CT (GE Healthcare, Princeton, NJ, USA). Inspiratory and expiratory CT were acquired with patients immobilised on a radiotherapy palette in the conventional supine treatment planning position with arms raised above the head. The inspiratory breath-hold was performed by inhaling 1L from a Tedlar bag filled with room air. The following CT settings were used: tube voltage, 120 kV; tube current, 315 mA. CT in-plane resolution was approximately 0.98×0.98 mm with a pixel matrix of 512×512. CT slice thickness was 2.5 mm.

5.3.3 MR image acquisition

On the same day, patients underwent MRI in the conventional treatment planning position using a custom built radiotherapy palette to mimic CT positioning on a 1.5 T MR scanner (GE HDx, GE Healthcare, Milwaukee, WI). Hyperpolarised gas MRI was performed with two nuclei, ^{3}He (prepared in a dose of 200 mL ^{3}He gas and 800 mL N_2) and ^{129}Xe (600 mL of 129-enriched Xe gas and 400 mL N_2), which were polarised to approximately 25% using a prototype commercial spin exchange optical pumping polariser (GE Healthcare, Amersham, UK), and a home-built system (Norquay *et al.*, 2013), respectively. Firstly, ^{129}Xe and corresponding anatomical ^{1}H images of the chest were acquired in separate breath-holds at the same inflation state as inspiratory CT. Immediately afterwards, ^{3}He & ^{1}H MR images were acquired, also at the same inflation state as inspiratory CT but in a single breath-hold using methods developed for same breath imaging of two nuclei on this scanner (Wild *et al.*, 2011; Wild *et al.*, 2013; Horn *et al.*, 2014).

The following sequence parameters were used for ^{129}Xe MRI: 3D steady-state free precession pulse sequence, 4x4mm^2 in-plane resolution, 10mm slice thickness, 40cm field of view, 2.2ms echo time, 6.7ms repetition time, 10º flip angle, ±8kHz bandwidth and full lung coverage (20 to 24 slices). The following

sequence parameters were used for ^{3}He MRI: 3D steady-state free precession pulse sequence, 4x4mm^{2} in-plane resolution, 5mm slice thickness, 40cm field of view, 0.6ms echo time, 1.9ms repetition time, 10º flip angle, ±83.3kHz bandwidth and full lung coverage (40 to 48 slices).

Corresponding separate and same-breath anatomical ^{1}H images (Wild *et al.*, 2011) were acquired with equivalent spatial resolution as ^{3}He and ^{129}Xe images using the ^{1}H transmit-receive body coil of the scanner with the following settings; 3D spoiled gradient echo sequence, 0.6ms echo time, 1.9ms repetition time, 5º flip angle, and ±83kHz bandwidth. Coronal slices from inspiration and expiration CT, separate breath ^{129}Xe and ^{1}H, and same breath ^{3}He and ^{1}H MRI for an example patient are shown in Figure 5.1. Coronal slices from ^{129}Xe and ^{3}He fused with their corresponding anatomical ^{1}H MR images are shown for an example patient in Figure 5.2.

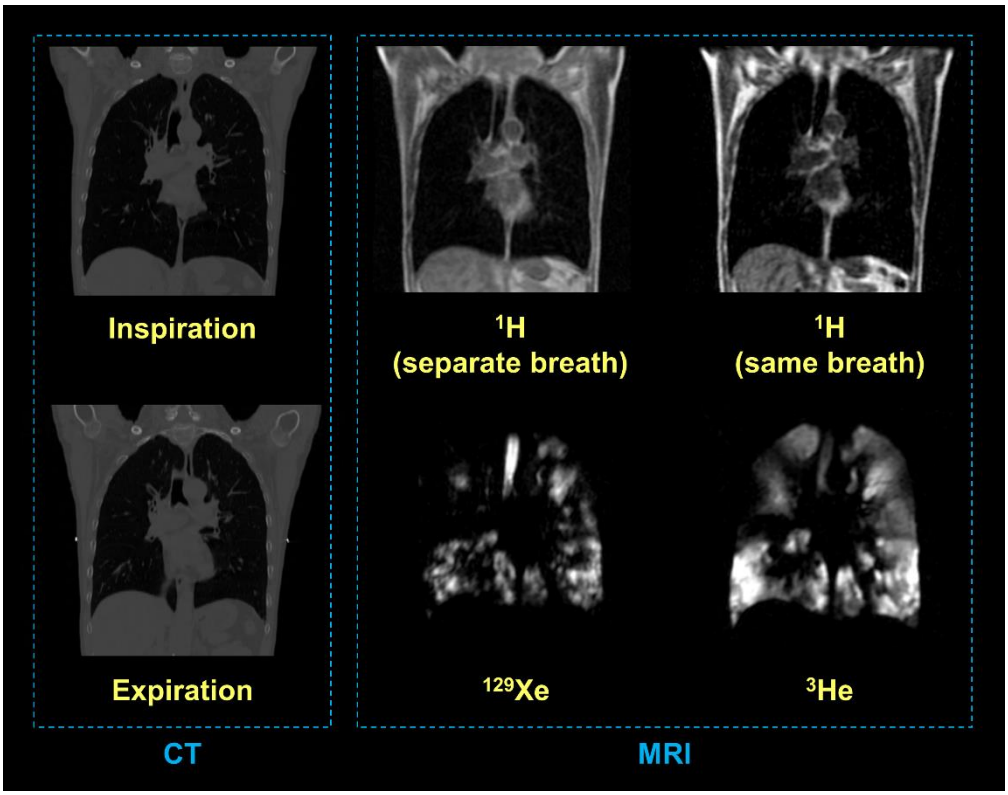

Figure 5.1 Example coronal slices of CT (left) and MR (right) images acquired. Inspiratory CT was acquired at the same inflation state of FRC+1L as for all MR images. Separate and same breath anatomic ^{1}H MRI were acquired for ^{129}Xe and ^{3}He, respectively.

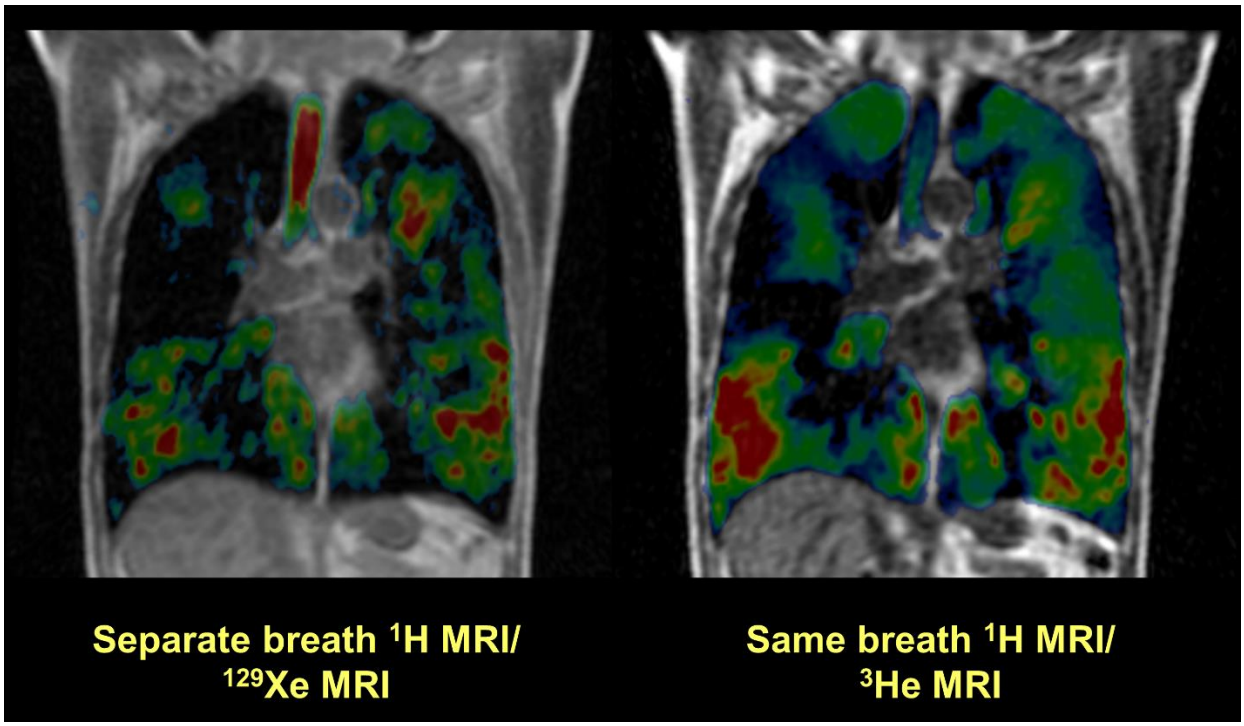

Figure 5.2 Coronal slices for ^{129}Xe and ^{3}He fused with their corresponding same breath and separate breath anatomical ^{1}H MR images, respectively.

5.3.4 Image segmentation

For subsequent processing steps including image registration, the lungs in CT and MRI images needed to be segmented. CT lung parenchyma was segmented using the Eclipse treatment planning system (Varian Medical Systems, Palo Alto, CA, USA). Segmentation errors were manually corrected.

^{1}H MR lung parenchyma was segmented according to the following pipeline. Prior to segmentation, images were pre-processed using a bilateral filter (Tomasi and Manduchi, 1998). Application of this filter maintains edges by combining, in a nonlinear way, range and domain filtering. For segmentation, a modified version of the Spatial Fuzzy C-means (FCM) algorithm presented by Chuang *et al.* (2006) was used. This methodology is based on the classic FCM clustering algorithm (Bezdek, 1981). This method assigns N pixels to C clusters via fuzzy memberships, based on histogram information only. Chuang

et al. (2006) modified this standard approach by implementing a spatial constraint in the membership function, which will modify the membership of a voxel only if it would be incorrectly classified using the standard FCM method, for example, if it was corrupted by noise. The spatial information modifies the membership function used in the cost function minimisation by incorporating the membership of pixels from a 5x5 window. The assumption being that pixels geometrically close should belong to the same cluster. For this work, the values for the bilateral filter, and threshold of membership function for inclusion in the binary masks, were empirically derived from data separate from that presented here.

5.3.5 Image registration

Image registration was performed using the `antsRegistration` tool incorporated as part of the Advanced Normalization Tools (ANTs) (Avants *et al.*, 2011; Avants *et al.*, 2012).

For each patient, three image registrations using rigid, affine and diffeomorphic stages were performed as follows:

1) Expiratory CT to inspiratory CT
2) Inspiratory CT to ^{3}He MRI's same breath ^{1}H MRI
3) ^{129}Xe MRI's separate breath ^{1}H MRI to ^{3}He MRI's same breath ^{1}H MRI

All fixed and moving images were initially pre-processed by masking all regions outside the lungs. A coarse pre-alignment rigid transform was applied to align the centers of mass of the fixed and moving image intensities. The resulting transform was then applied to rigid and affine stages using the mutual information similarity metric with 32 histogram bins optimized via the gradient descent algorithm with a step size of 0.1. A multi-resolution Gaussian pyramid with 4 levels was used with down-sampling factors 8x4x2x1 and corresponding smoothing Gaussian sigmas of 3x2x1x0 mm. A maximum of 10,000 iterations were set for each resolution level to ensure convergence (Glocker *et al.*, 2011).

An additional diffeomorphic transformation with explicit B-spline regularization (Tustison and Avants, 2013) that copes with larger deformations than the familiar Symmetric Normalization (SyN) algorithm (Avants *et al.*, 2008) was also applied to the resulting transform of the affine pipeline with a knot spacing for the update field of 65 mm. A 5-level multi-resolution pyramid was applied with down-sampling factors of 10x6x4x2x1 and corresponding smoothing Gaussian sigmas of 5x3x2x1x0 mm and the normalized correlation coefficient similarity metric. A step size of 0.2 was selected for the gradient descent optimization algorithm.

As detailed in Appendix A, the registration pipeline was tested on the inspiratory and expiratory COPD breath-hold DIR lab dataset (Castillo *et al.*, 2013), one of the most challenging pulmonary reference datasets to register, and a mean target registration of 1.26±0.27mm was observed. For this study, registration accuracy of inspiratory to expiratory CT and inspiratory CT to ^{1}H MRI was assessed using the dice overlap coefficient of the lung segmentations.

To reduce the computational time in performing the registration, 8 cores via an Intel Xeon E5-2670 processors @ 2.60 GHz were run in parallel on a 64-bit high performance Linux server (Iceberg, University of Sheffield) using the multi-threading options available in Insight Toolkit version 4 (ITK, www.itk.org).

As the ^{129}Xe MR image was acquired in the same inflation state of FRC+1L as its corresponding separate breath anatomic ^{1}H MR image, they were assumed to be initially spatially co-registered. This assumption was checked for each patient. Consequently, the same transform to map ^{129}Xe MRI's separate breath ^{1}H MRI to ^{3}He MRI's same breath ^{1}H MRI was applied to map ^{129}Xe MRI to ^{1}H MRI with linear interpolation using the `antsApplyTransform` tool available in ANTs.

5.3.6 CT ventilation computation

For this study, we investigated three methods for generating voxel-wise CT surrogates of ventilation: Hounsfield unit (HU) change (CT^{HU}), specific gas volume change (CT^{SGV}) and the Jacobian (CT^{Jac}) metrics. All CT ventilation images were generated at inhalation CT geometry. The following provides a brief explanation as to how the metrics were computed.

The CT^{HU} metric was computed from voxel-wise intensity differences in Hounsfield unit (HU) values based on a modified version of the original formulation of Guerrero *et al.* (2005) to account for the computation being performed in the inhalation CT spatial domain:

$$\frac{\Delta V}{V_{exp}} = 1000 \frac{HU_{ins} - \overline{HU}_{exp}}{\overline{HU}_{exp}(1000 + HU_{ins})}$$

where $\overline{HU}_{exp}$ is the average HU of the voxels in the moving deformed expiration image which spatially correspond to the voxels in the fixed inspiration image and HU_{insp} is the HU of the inspiratory voxel. CT^{HU} purports to be a measure of change in fractional content of air per voxel between respiratory phases.

CT^{SGV} was computed from voxel-wise differences in specific gas volume (ΔSGV) between the warped expiration ($\overline{SVG}_{exp}$) and fixed inspiration image (SGV_{ins}) using the following formula (Aliverti *et al.*, 2013):

$$\Delta SGV = SGV_{ins} - \overline{SVG}_{exp}$$

CT^{Jac} was calculated directly on the inversely consistent deformation field of expiratory CT to inspiratory CT by computing the Jacobian determinant (J) of the deformation field $h(x, y, z)$ as:

$$J\big(h(x,y,z)\big) = \begin{vmatrix} 1+\dfrac{\partial h_x(x,y,z)}{\partial x} & \dfrac{\partial h_x(x,y,z)}{\partial y} & \dfrac{\partial h_x(x,y,z)}{\partial z} \\ \dfrac{\partial h_y(x,y,z)}{\partial x} & 1+\dfrac{\partial h_y(x,y,z)}{\partial y} & \dfrac{\partial h_y(x,y,z)}{\partial z} \\ \dfrac{\partial h_z(x,y,z)}{\partial x} & \dfrac{\partial h_z(x,y,z)}{\partial y} & 1+\dfrac{\partial h_z(x,y,z)}{\partial z} \end{vmatrix}$$

The Jacobian determinant provides a measure of contraction and expansion such that a voxel value of one represents preservation of local volume while values less than and greater than one correspond to contraction and expansion of local volume, respectively. To ensure that it was spatially correlated to the other metrics, it was subsequently warped to the spatial domain of inspiratory CT by applying the transform of expiratory CT to inspiratory CT with linear interpolation using the `antsApplyTransform` tool available in ANTs.

5.3.7 Quantitative spatial comparison of ventilation CT & HP gas MRI

To ensure that the generated ventilation CT images were in the same spatial domain as ^{3}He and the warped ^{129}Xe MRI, the inspiratory CT to ^{1}H MRI transform was applied to all ventilation CT images using the `antsApplyTransform` with linear interpolation. This enabled a direct spatial comparison of CT ventilation with both ^{3}He and ^{129}Xe MRI as shown in Figure 5.3. Spatial correlation was assessed by computing the voxel-wise Spearman correlation coefficients between each ventilation CT image and its corresponding ^{3}He/^{129}Xe MR image and for the median values in corresponding regions of interest (ROIs), ranging from finer to coarser in-plane dimensions of 5 by 5, 10 by 10, 15 by 15 and 20 by 20, located within the lungs as defined by the same-breath ^{1}H MRI lung mask.

In order to account for uncertainties in the HU values due to image noise and registration errors, most studies post-process the computed ventilation CT images by applying filtering (Castillo *et al.*, 2012; Castillo *et al.*, 2010; Guerrero *et al.*, 2005). To understand the effect of filtering on the spatial correlation of ventilation CT and hyperpolarised gas MRI, the same analysis was performed

with a median filter radius ranging from 1x1x1 to 7x7x7 voxels applied to the CT^{HU} image. As a secondary analysis to establish baseline Spearman correlation coefficient values when two similar ventilation imaging techniques are compared, we assessed the Spearman coefficients between ^{3}He and ^{129}Xe MRI at the voxel-level and for the same ROIs detailed above.

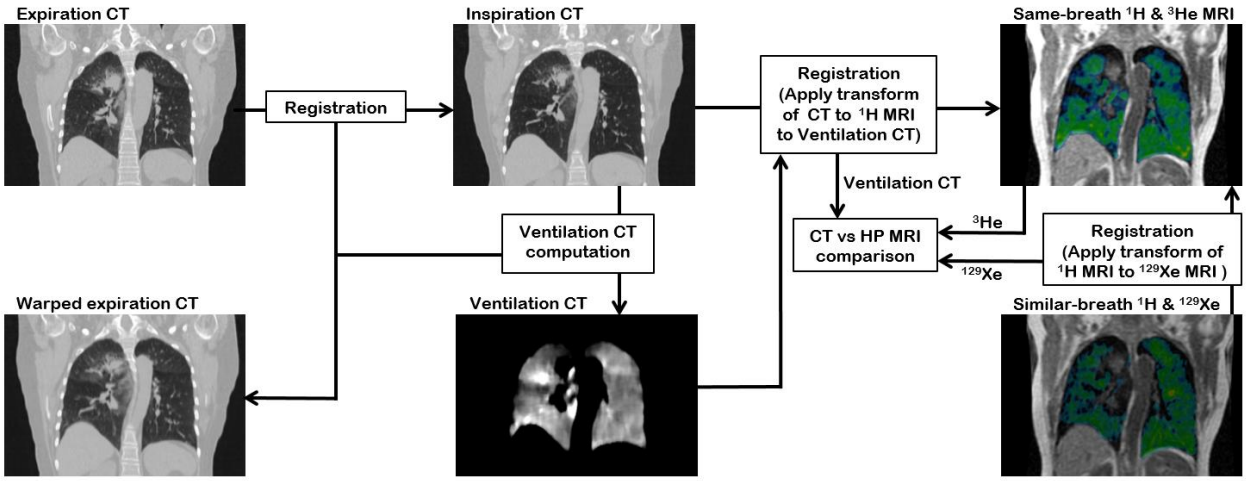

Figure 5.3 Workflow of comparison method of ventilation CT and HP MRI (^{3}He MRI and ^{129}Xe).

5.3.8 Statistical analysis

Statistical analysis was performed by using IBM SPSS software (version 20.0; Chicago, Il, USA). A p value less than 0.05 was considered statistically significant. The Wilcoxon signed-rank test was used to test the statistical significance of the differences between the Spearman correlation coefficients of the different ventilation CT methods and HP gas MRI for the voxel-wise and ROI analysis. In addition, the ^{3}He vs ^{129}Xe Spearman correlation coefficients were compared to that of ventilation CT vs ^{3}He and ^{129}Xe MRI.

5.4 Results

5.4.1 Patient characteristics

From February to December 2015, 7 patients were enrolled on the study. One patient was unable to tolerate the MR imaging acquisition procedure and the data for another was excluded due to truncated lung, thus leaving 5 patients. Characteristics of these patients are described in **Table 5.1**.

Table 5.1 NSCLC patient characteristics

	Demographics				Tumour	
Patient	Age	Sex	COPD	Smoker	Site	Staging
1	68	F	N	Current	RUL	T2 N2 M0
2	63	M	Y	Current	RLL	T2b N1/2 M0
3	73	F	N	Former	RUL	T2a N1 Mx
4	72	F	Y	Former	RUL	T2 N2 Mx
5	62	F	Y	Former	RUL	T3 N0 M0

5.4.2 Image registration

Visual examination indicated accurate registration of the three registration pipelines performed in this study. An example is shown in Figure 5.4 for the registration of expiratory to inspiratory breath-hold CT. Quantitative overlap analysis using the dice correlation coefficient demonstrated a mean±SD for the expiratory to inspiratory CT and inspiratory CT to ^{1}H MRI registrations of 0.99±0.00 and 0.98±0.00, respectively. Table **5.2** displays the dice results of both registration pipelines for all patients.

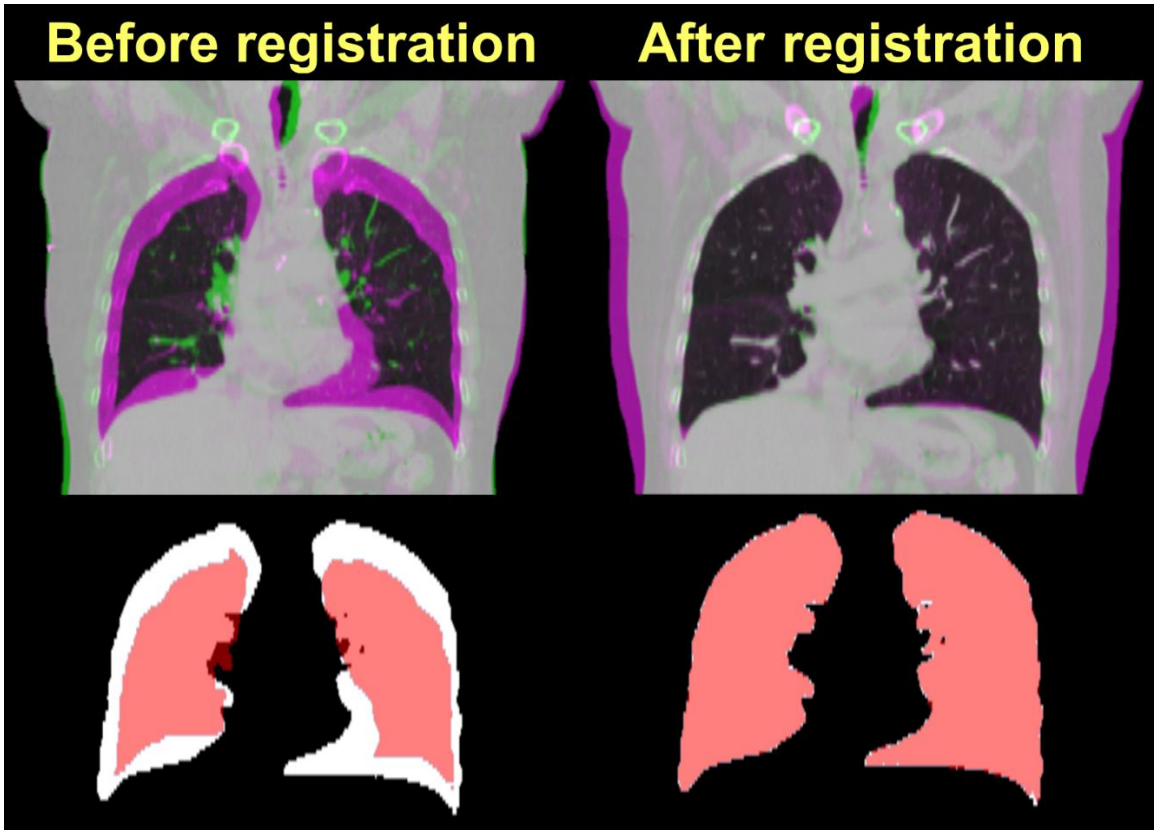

Figure 5.4 Example coronal slice of expiratory CT image overlaid on inspiratory CT image before (left) and after (right) diffeomorphic image registration for the intensity images (top) and lung segmentations (bottom).

Table 5.2 Dice correlation coefficients for the CT and ^{1}H MRI deformable registrations.

Patient	Inspiratory CT to Expiratory CT	Inspiratory CT to ^{1}H MRI
1	0.99	0.98
2	0.99	0.98
3	0.99	0.97
4	0.99	0.98
5	0.99	0.97
Mean	0.99	0.98
SD	0.00	0.00

5.4.3 Spatial comparison of ventilation CT & HP gas MRI

Figure 5.5 shows corresponding coronal slices of the three CT ventilation methods (CT^{HU}, CT^{SGV} and CT^{JAC}) filtered with a median radius of 3x3x3 and ^{3}He and ^{129}Xe MRI for an example patient after image registration. A similarly located ventilation defect can be observed in all images in the right upper lobe with varying degrees of spatial extent where CT^{HU} is visually closer to hyperpolarised gas MRI than that of CT^{SGV} and CT^{JAC}. Nonetheless, the hyperpolarised gas MR images exhibited a larger ventilation defect region than that of CT^{HU}. Consequently, whereas the voxel-wise Spearman correlation coefficients of CT^{HU} against ^{3}He and ^{129}Xe MRI were calculated to both be 0.50 for this patient, the correlation between ^{3}He and ^{129}Xe was 0.75.

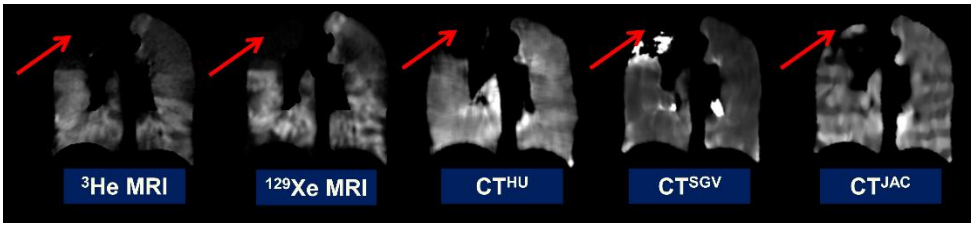

Figure 5.5 Coronal views of CT^{HU}, CT^{SGV} and CT^{JAC} filtered with a median radius of 3x3x3 and ^{3}He and ^{129}Xe MRI after image registration for an example patient. A similar ventilation defect is observed in all three images in the right upper lobe with varying spatial extent (red arrow).

Table **5.3** shows the Spearman correlation coefficients of all patients between CT^{HU} filtered with a median radius of 3x3x3 voxels against ^{3}He and ^{129}Xe MRI at the voxel level and for a range of corresponding ROIs. For comparison, the results of the spatial comparison between ^{3}He and ^{129}Xe MRI are also included. These results are graphically displayed as a box plot in Figure **5.6**. Several interesting results can be observed from the data. Firstly, the spatial correlations between CT^{HU}, ^{3}He and ^{129}Xe begin to increase with more coarsely defined ROIs and start to reach a plateau for ROIs of 15x15 voxels. Furthermore, a marked increase in Spearman correlation was observed for ^{3}He and ^{129}Xe MRI compared with when CT^{HU} was compared with either ^{3}He and ^{129}Xe MRI. These observed differences were statistically significant over all ROIs ($p < 0.05$). No significant differences were observed when CT^{HU} was compared to either ^{3}He and ^{129}Xe MRI.

Table 5.3 Spearman correlation coefficients for ventilation CT (CT^{HU} with median filter radius of 3x3x3) and hyperpolarised gas MRI (^{3}He MRI and ^{129}Xe) for a range of ROIs.

Patient	Voxel			5x5			10x10			15x15			20x20		
	CT vs ^{3}He	CT vs ^{129}Xe	^{3}He vs ^{129}Xe	CT vs ^{3}He	CT vs ^{129}Xe	^{3}He vs ^{129}Xe	CT vs ^{3}He	CT vs ^{129}Xe	^{3}He vs ^{129}Xe	CT vs ^{3}He	CT vs ^{129}Xe	^{3}He vs ^{129}Xe	CT vs ^{3}He	CT vs ^{129}Xe	^{3}He vs ^{129}Xe
1	0.33	0.34	0.69	0.39	0.40	0.72	0.45	0.46	0.77	0.54	0.56	0.82	0.53	0.50	0.80
2	0.12	0.22	0.58	0.16	0.28	0.61	0.22	0.34	0.65	0.26	0.40	0.68	0.29	0.46	0.68
3	0.35	0.43	0.45	0.42	0.52	0.50	0.47	0.58	0.53	0.50	0.62	0.53	0.50	0.63	0.52
4	0.40	0.29	0.47	0.45	0.36	0.51	0.50	0.41	0.56	0.51	0.41	0.55	0.54	0.44	0.59
5	0.50	0.50	0.75	0.54	0.55	0.78	0.57	0.58	0.81	0.61	0.63	0.82	0.64	0.68	0.83
Mean	0.34	0.36	0.59	0.39	0.42	0.62	0.44	0.47	0.66	0.48	0.52	0.68	0.50	0.54	0.68
SD	0.14	0.11	0.13	0.14	0.11	0.12	0.13	0.11	0.12	0.13	0.11	0.14	0.13	0.11	0.13

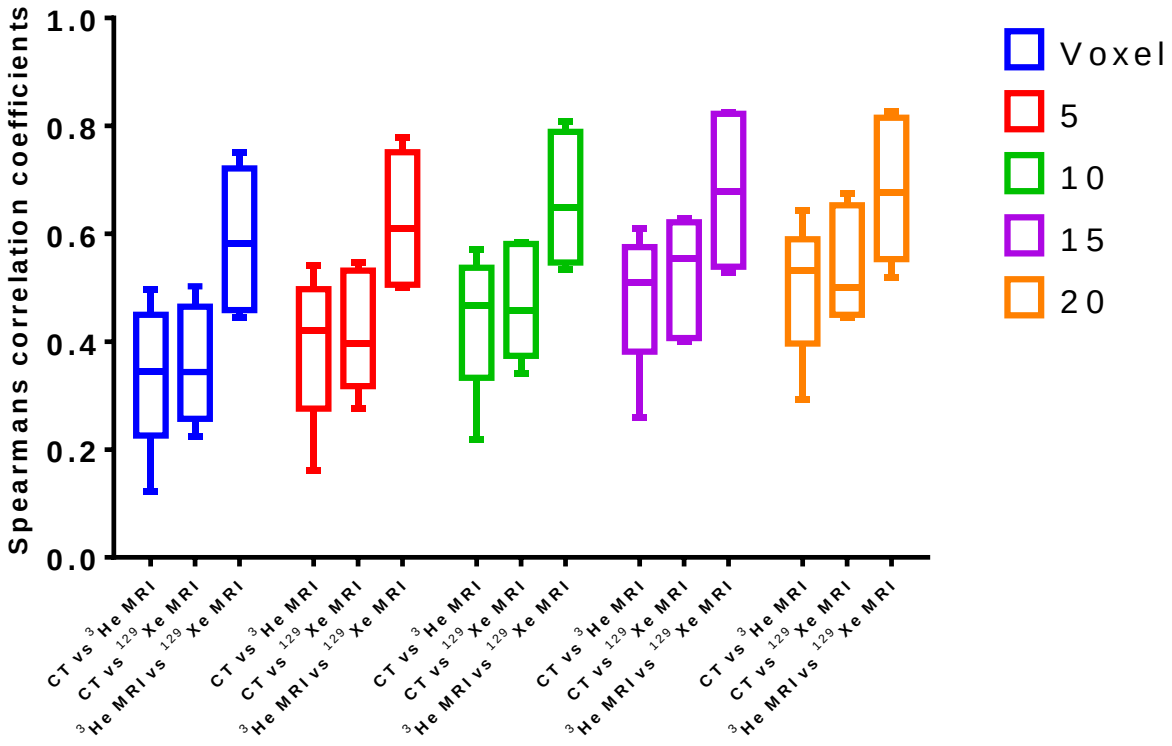

Figure 5.6 Box plot of Spearman correlation coefficients for ventilation CT (CT^{HU} with median filter radius of 3x3x3) and hyperpolarised gas MRI (^{3}He MRI and ^{129}Xe) at the voxel-level and for a range of ROIs. The central mark of each box represents the median, with its edges the 25th and 75th percentiles. The whiskers extend to the minimum and maximum values.

5.4.4 Effect of filtering

Table **5.4** shows the effects of varying median filter sizes on the Spearman correlations of the CT^{HU} metric and both ^{3}He and ^{129}Xe MRI. Individual scatter plots of CT^{HU} against both ^{3}He and ^{129}Xe MRI are shown in Figure **5.7**. A number of interesting results can be observed from the data. Firstly, the application of filtering brings about a marked improvement in spatial correlation against hyperpolarised gas MRI compared with the unfiltered images. However, a plateau is reached at a median filter radius of 3x3x3 voxels whereby no significant increases in correlation coefficients ($p < 0.05$) are observed thereafter. Performing the voxel-wise Spearman's analysis over increasing ROI sizes results in increased correlation. Again, a similar trend was observed as in Table **5.4** where the increases are only marginal at larger ROI sizes of 15x15 with little increase observed at 20x20.

Table 5.4 Median spearman correlation coefficients for CT^{HU} and hyperpolarised gas MRI (^{3}He MRI and ^{129}Xe) for varying median filer kernel sizes.

	Voxel		5x5		10x10		15x15		20x20	
Median filter radius	CT vs ^{3}He	CT vs ^{129}Xe	CT vs ^{3}He	CT vs ^{129}Xe	CT vs ^{3}He	CT vs ^{129}Xe	CT vs ^{3}He	CT vs ^{129}Xe	CT vs ^{3}He	CT vs ^{129}Xe
0	0.21	0.21	0.30	0.32	0.40	0.42	0.46	0.50	0.49	0.53
1	0.29	0.30	0.35	0.36	0.42	0.44	0.47	0.50	0.49	0.53
2	0.33	0.34	0.38	0.40	0.43	0.46	0.48	0.51	0.50	0.53
3	0.34	0.36	0.39	0.42	0.44	0.47	0.48	0.52	0.50	0.54
4	0.34	0.36	0.40	0.43	0.45	0.48	0.49	0.53	0.50	0.55
5	0.35	0.36	0.41	0.44	0.45	0.49	0.49	0.54	0.51	0.55
6	0.34	0.36	0.41	0.44	0.46	0.49	0.49	0.54	0.51	0.56
7	0.34	0.35	0.41	0.44	0.45	0.49	0.49	0.54	0.50	0.56

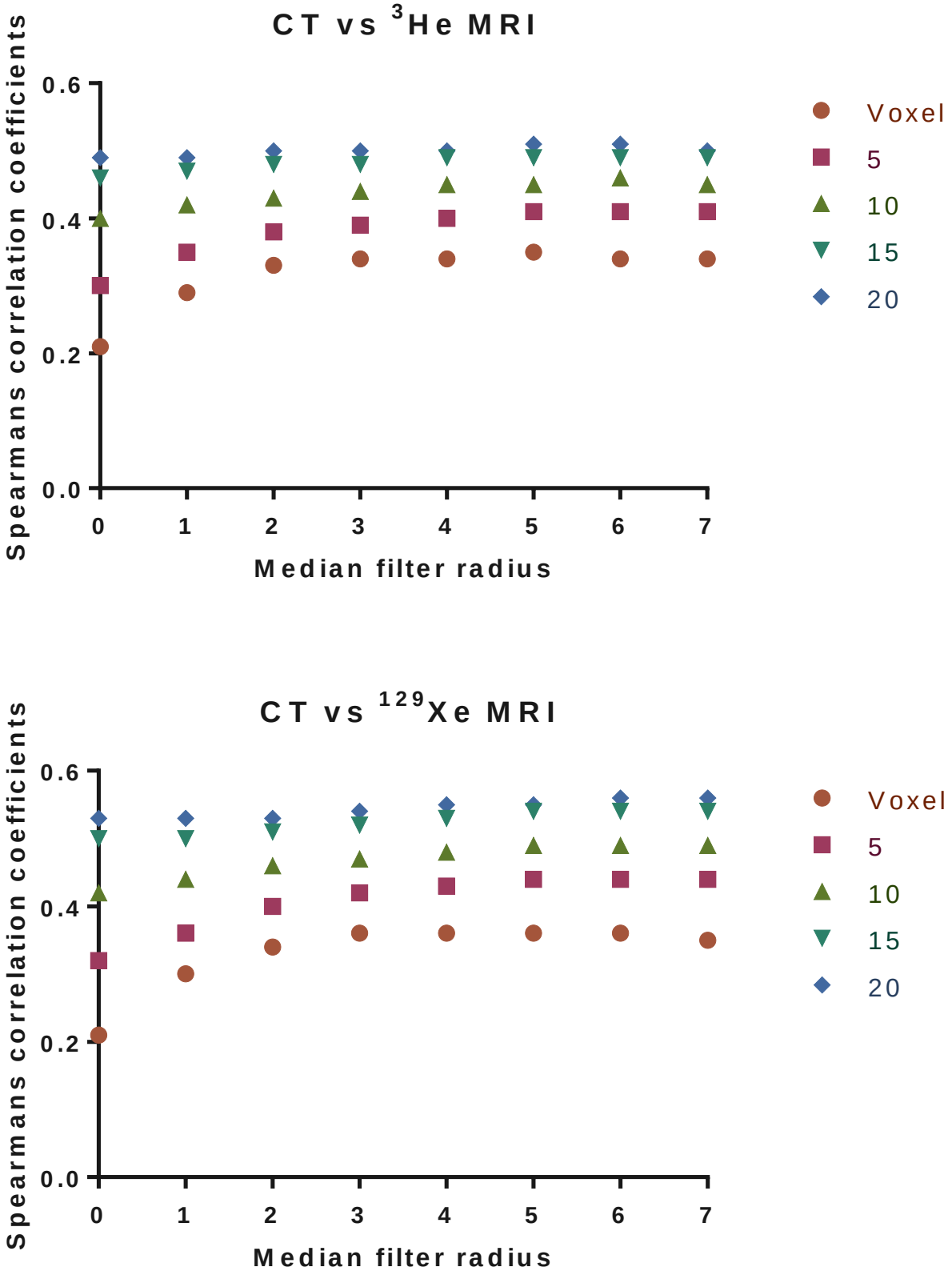

Figure 5.7 Scatter plots of CT^{HU} against both ^{3}He (top) and ^{129}Xe (bottom) MRI with varying median filter radius.

Table **5.5** shows the effects of different CT ventilation metrics and filtering settings on mean Spearman correlation coefficients of CT ventilation against both ^{3}He and ^{129}Xe. A similar trend is observable as in Table **5.3** whereby spatial correlation increases for each configuration with increasing ROIs size. In this study, we found that the CT^{HU} metric performed significantly better than the other two metrics studied when filtering was applied. One exception should be noted; CT^{Jac} performed better than the other two metrics for the voxel-wise comparison when no filtering was applied. This is perhaps attributable to the fact that CT^{Jac} is derived from the deformation field which already undergoes smoothing during the registration process and thus is more robust against outliers.

Table 5.5 Mean Spearman correlation coefficients between a range of CT ventilation metrics with varying filtering settings and both ^{3}He and ^{129}Xe MRI.

		Voxel		5x5		10x10		15x15		20x20	
CT ventilation method	Filter radius	CT vs ^{3}He	CT vs ^{129}Xe	CT vs ^{3}He	CT vs ^{129}Xe	CT vs ^{3}He	CT vs ^{129}Xe	CT vs ^{3}He	CT vs ^{129}Xe	CT vs ^{3}He	CT vs ^{129}Xe
CT^{HU}	0	0.21	0.21	0.30	0.32	0.40	0.42	0.46	0.50	0.49	0.53
CT^{SGV}	0	0.13	0.09	0.20	0.17	0.30	0.29	0.37	0.37	0.39	0.39
CT^{Jac}	0	0.23	0.25	0.27	0.29	0.34	0.36	0.39	0.42	0.43	0.47
CT^{HU}	3	0.34	0.36	0.39	0.42	0.44	0.47	0.48	0.52	0.50	0.54
CT^{SGV}	3	0.25	0.22	0.31	0.29	0.36	0.35	0.40	0.39	0.41	0.40
CT^{Jac}	3	0.28	0.30	0.31	0.33	0.37	0.39	0.40	0.44	0.44	0.48
CT^{HU}	6	0.34	0.36	0.41	0.44	0.46	0.49	0.49	0.54	0.51	0.56
CT^{SGV}	6	0.28	0.24	0.35	0.35	0.39	0.39	0.43	0.43	0.44	0.44
CT^{Jac}	6	0.33	0.35	0.36	0.40	0.41	0.45	0.44	0.48	0.46	0.50

5.5 Discussion

CT image registration based surrogates of ventilation have been proposed as an alternative technique of imaging regional ventilation. The clinical validation of these surrogates is a necessary prerequisite to clinical implementation. To this end, in this study, a novel image acquisition and processing strategy to facilitate the spatial correlation of ventilation surrogates computed from inspiratory and expiratory breath-hold CT with hyperpolarised ^{3}He & ^{129}Xe MRI was developed and tested in a cohort of lung cancer patients. The following findings were observed:

a. low correlations at the voxel level for CT ventilation against both ^{3}He and ^{129}Xe MRI, increasing to more moderate levels for coarser regions;
b. higher correlations with increased degrees of filtering reaching a plateau for a median filter radius of 3x3x3 voxels;
c. higher correlations for the CT^{HU} metric compared with CT^{Jac} and CT^{SGV};
d. consistently higher correlation of ^{3}He and ^{129}Xe MRI compared with the case when either gas was correlated to CT ventilation.

5.5.1 Spatial correlation of CT ventilation with HP gas MRI

This study observed low correlations at the voxel level for CT ventilation against both ^{3}He and ^{129}Xe MRI, increasing to more moderate levels for coarser regions. These findings are consistent with those of a previously published study comparing 4D-CT based ventilation with ex vivo Cryomicrotome imaging of FMS in the excised lungs of rats (Jacob *et al.*, 2015). That study observed improved correlations for larger ROIs. At the lobar level, high correlations have also been demonstrated for ^{3}He MRI (see chapter 3) and PET Galligas (Eslick *et al.*, 2016). Visual comparisons of the ventilation CT and hyperpolarised MR images demonstrated similar ventilation defects but, in many cases, spatially offset with varying extent. This may explain why CT-based surrogates of ventilation tend to demonstrate increased correlation at coarser levels. Larger ROIs will also be less dependent on registration errors, inducing stronger correlation.

A similar trend in increasing correlation at the voxel level was observed for increasing filter sizes which is in line with previous studies comparing the effects of filtering on Spearman's correlation (Kipritidis *et al.*, 2016). Interestingly, although an increase in Spearman correlations were observed with increasing ROI size, a plateau was observed for filter sizes of 3x3x3 voxels and higher. A possible explanation is that we only applied filtering to the ventilation CT images and not to the reference hyperpolarised gas MR images whereas the ROI analysis was applied equally to all images. As the ROI acts as a filter, we speculate that the same trend may be observed when filtering is applied equally to the reference hyperpolarised MR images. Nonetheless, for most applications, a median filter of 3x3x3 voxels seems reasonable.

In agreement with previous studies (Yamamoto *et al.*, 2011b; Latifi *et al.*, 2013b), visual examination of ventilation images derived from the intensity (CT^{HU} and CT^{SGV}) and volume change (CT^{JAC}) based metrics indicated significant differences between the two methods. These differences could be related to several causes. One explanation could be due to the fact that the density based metrics are applied directly to the raw HU values of the fixed and registered images and are thus susceptible to the inherent fluctuations in HUs as measured by CT (Boedeker *et al.*, 2004; Hochhegger *et al.*, 2011). On the other hand, the Jacobian metric is calculated on the deformation field which in the case of ANTs is smoothed by B-Spline regularization (Tustison and Avants, 2013). This can be shown from the Jacobian images which constantly appear smoother than their intensity based analogues when no filtering is applied and misregistration errors will thus have less of an effect on these images. This could explain why CT^{JAC} outperformed the other density based metrics for the voxel wise analysis when no filtering was applied. Recent work has shown the Jacobian metric to be numerically unstable in that small changes in the deformation field can give rise to larger changes in the ventilation distribution (Castillo *et al.*, 2017). The B-Spline knot spacing used for regularisation was constant for each patient. Future work will investigate the effect of varying this parameter on CT^{JAC}.

To the best of our knowledge, this study represents the first published attempt to compare CT^{SGV} with an established ventilation modality. CT^{SGV} has recently been proposed as an alternative technique for generating surrogates of ventilation (Aliverti *et al.*, 2013). In this study, CT^{SGV} was consistently outperformed by both CT^{HU} and CT^{Jac}. Previously, Pennati *et al.* (2014) compared CT^{SGV} with CT^{HU} in healthy normals and observed that CT^{SGV} provides more homogenous distributions of ventilation with minimal gravitational dependence. However, although this has been argued to be an advantage of CT^{SGV} in terms of decreasing variation in longitudinal evaluations and improving discernment of health from disease (Pennati *et al.*, 2014), it appears to mask true ventilation heterogeneity. Although gravitational effects have been traditionally invoked as the sole cause of ventilation heterogeneity in healthy subjects, recent studies have demonstrated heterogeneity within isogravitational planes (Glenny, 2009). Thus, CT^{HU} and CT^{JAC} may provide more accurate estimates of regional ventilation.

Despite notable similarities, none of the ventilation CT images were perfectly matched to hyperpolarised gas MRI and marked discrepancies in ventilation were observed. There are multiple mechanisms that may be responsible for the differences observed between CT-based surrogates of ventilation and hyperpolarised gas MRI. Most notably, the fundamental assumption inherent in all the ventilation metrics applied in this study is that changes in lung density and volume between inflation levels are due solely to the influx of air and that air distribution is uniform (Ding *et al.*, 2012). However, recent investigations with dual energy CT has demonstrated that the regional distribution of pulmonary blood volume is sensitive to inflation level with marked variations observed in dependant and non-dependant regions (Fuld *et al.*, 2013). The correlation of CT-based surrogates of ventilation with hyperpolarised gas MRI may improve if additional images of regional blood volume at the same inflation levels as ventilation CT are explicitly incorporated within the ventilation model.

Discrepancies between techniques may also be due to transient ventilation defects caused by a number of factors including a shift of mucus plugs during

breath-hold (Woodhouse *et al.*, 2009). A competing explanation is that variations may also be due to delayed-filling ventilation defects related to the difference in breath-hold acquisition times; CT was acquired within 15 to 20 seconds whilst ^{3}He and ^{129}Xe MRI were acquired within 7 and 15 seconds, respectively. Marshall *et al.* (2012) have shown that some ventilation defects tend to resolve at a later time point within a single 15 second breath-hold. Collateral ventilation has been proposed as a possible mechanism associated with this observed phenomenon.

5.5.2 Spatial correlation of ^{3}He and ^{129}Xe MRI

To the best of our knowledge, this is also the first study to quantitatively assess the spatial correlation between ^{3}He and ^{129}Xe MRI at a voxel and regional level. As such, the results may have important implications to clinicians and scientists specialising in the field of hyperpolarised gas MRI. The hyperpolarised gases used in this study, namely, ^{3}He and ^{129}Xe, exhibited a moderately high degree of spatial correlation, improving with increasing ROI sizes. Given the paucity of global ^{3}He supplies, these preliminary results are promising for using ^{129}Xe as an analogue to ^{3}He for hyperpolarised Gas MRI.

Although, in general, the locations of ventilation defects were similar between the gases, subtle differences in ventilation distributions were observed in this study. In all cases, a higher degree o f ventilation heterogeneity and defects was observed for ^{129}Xe compared with ^{3}He MRI, consistent with recent studies comparing ^{129}Xe and ^{3}He MRI in patients with asthma and COPD (Svenningsen *et al.*, 2013; Kirby *et al.*, 2013).

There are a number of potential explanations for the differences in regional ventilation between ^{3}He and ^{129}Xe MRI. Firstly, due to the lower signal to noise ratio of ^{129}Xe MRI compared to ^{3}He MRI, as noted by Svenningsen *et al.* (2013), it is possible that regions of reduced intensity appear as additional ventilation defects. Secondly, the differences in diffusivity of the gases may give rise to the differences; by virtue of its lower molecular weight, ^{3}He has a

much higher diffusion coefficient than ^{129}Xe and is thus more prone to penetrate partial obstructions, leading to increased ventilation.

Despite the observed differences between ^{3}He and ^{129}Xe MRI, the two techniques agreed with each other to a considerably better level than when each was compared to ventilation CT. The Spearman correlations between the MR images of the noble gases studied may provide an upper limit of what can be achieved when comparing similar modalities.

5.5.3 Study limitations

Although this study provides promising preliminary results, several points of limitation need to be acknowledged. First, the sample size is small; thus caution must be exercised when extrapolating the results to a larger cohort. However, the primary purpose of this study was methodological in nature with the aim of developing an optimised image acquisition and analysis framework to facilitate spatial correlation between ventilation CT and hyperpolarised gas MRI. A larger scale correlation study is currently underway which will apply the methods developed in this study to a greater number of patients.

Although ^{1}H MRI was acquired in the same breath as ^{3}He MRI, in order to improve registration to CT by indirectly registering ^{3}He to CT via ^{1}H MRI as was demonstrated in chapter 2, this was not the case with the ^{129}Xe MRI's corresponding anatomic ^{1}H MRI. Furthermore, the slice thickness of the ^{129}Xe MRI was twice that of ^{3}He MRI (10mm vs 5mm), requiring interpolation of the former to the latter. ^{129}Xe has an approximately 3-fold lower gyromagnetic ratio than ^{3}He; as such, lower bandwidths are required to achieve an adequate signal to noise ratio. This inevitably prolongs the acquisition time, prohibiting volumetric acquisition of ^{129}Xe and ^{1}H MRI in a single breath-hold. However, progress towards overcoming these technical limitations is currently underway in our research group, particularly with the introduction of novel compressed sensing techniques to accelerate the image acquisition and facilitate same-breath ^{129}Xe and ^{1}H MRI by acquiring an undersampled k-space.

Registration accuracy was assessed using the COPD breath-hold DIR lab reference dataset (Castillo *et al.*, 2013) and sub-voxel accuracy was achieved. However, that dataset consisted of paired CT acquired at the extremes of inflation whilst the motion magnitudes of the data used here were significantly lower (FRC and FRC+1L). As such, equivalency cannot be assumed. Future work will entail delineating landmarks on the data used for this study and tuning registration parameters to ensure the best possible registration accuracy is achieved.

5.6 Conclusion

In conclusion, we developed an image acquisition protocol and analysis strategy to facilitate a direct spatial correlation of several methods of generating CT-based surrogates of ventilation against hyperpolarised ^{3}He and ^{129}Xe gas MRI. We tested this methodology in a cohort of lung cancer patients and observed moderately low correlations of CT at the voxel level against both hyperpolarised gases, increasing for more courser regional analysis. Discrepancies could be attributable to a number of factors including non-ventilatory effects due to blood volume changes between inflation states which are not accounted for in the CT ventilation models, the inherent noise in CT intensity, and registration errors at the voxel-level. Thus, it may be more beneficial to quantify ventilation at a more regional level. In all cases, the correlation was significantly less than for ^{3}He vs ^{129}Xe MRI.

Chapter 6
Summary and future directions

The novel contributions in this these are summarised in section 6.1. Potential clinical applications are discussed in section 6.2. Future research directions and limitations are noted in 6.3.

6.1 Novel contributions

The aim of this thesis was to compare surrogates of regional ventilation derived from inhale and exhale CT data with an established measure of ventilation. To this end, several methods were developed to facilitate lobar, regional and voxel level comparisons with hyperpolarised gas MRI and their application in patients was demonstrated.

Chapter 2 presented a novel methodology for improving registration accuracy of CT and hyperpolarised gas MRI by utilizing ^{1}H-structural MR images that are acquired in the same breath-hold as the ^{3}He MRI as an intermediary. This indirect method was shown to be significantly more accurate than direct registration. The feasibility of using this technique for the regional quantification of ventilation of specific pulmonary structures was also demonstrated for the lobes.

Chapter 3 took this method one step further and described a workflow for comparing lobar lung ventilation, computed from expiratory and inspiratory CT segmentations, with ventilation measurements from ^{3}He MRI. The workflow was applied to a cohort of asthmatics and despite subtle differences,

percentage regional ventilation per lobe calculated from CT was shown to be comparable to ^{3}He MRI.

Chapter 4 evaluated the impact of varying the inflation level of ^{3}He MRI on correlation with image registration based CT surrogates of ventilation. The correlation of ventilation CT and hyperpolarised gas MRI was shown to be sensitive to inflation state.

Chapter 5 described a novel image acquisition and analysis strategy for facilitating direct spatial correlation of ventilation CT and hyperpolarised gas MRI. The methods were tested with a cohort of lung cancer patients. The effect of using two different noble gases, namely, ^{3}He and ^{129}Xe, on the spatial correlation was also evaluated. In general, an increase in spatial correlations with more coarsely defined regions was observed. Furthermore, a marked increase in correlation was observed for ^{3}He and ^{129}Xe MRI in contrast to when ventilation CT was compared with either ^{3}He and ^{129}Xe MRI.

6.2 Potential Clinical applications

Sections 6.2.1 and 6.2.2 critically review the radiotherapy applications proposed in the literature. Speculations on potential applications in the wider respiratory field are briefly noted in section 6.2.3.

6.2.1 Functional avoidance radiotherapy treatment planning

One of the major driving forces behind the development of the ventilation CT technique is its potential for functionally guided radiotherapy treatment planning (Ireland *et al.*, 2016). This is due to its potential advantages over alternative functional modalities in terms of superior spatial resolution, not requiring a contrast agent and its widespread availability in radiotherapy clinics. In fact, in many centres worldwide, breath-holds and particularly 4D-CT are a pre-treatment requirement and would thus not cause additional scanner time, ionising radiation or patient inconvenience. Hence, the

ventilation information is referred to as ‘freely available’ (Partridge *et al.*, 2010) as only image processing comprising of non-rigid image registration and computation of the ventilation metric is required.

In an initial feasibility study, Yaremko *et al.* (2007) evaluated the dosimetric impact of incorporation of intensity based 4D-CT ventilation in intensity modulated radiotherapy (IMRT) for 21 lung cancer patients. Nine equidistant fields were used and a functionally guided approach to treatment planning was employed to test the hypothesis that the incorporation of the ventilation information results in statistically significant reductions in dose to functional lung. The study demonstrated a reduction in a number of functional dosimetric parameters including the mean reduction in dose to functional lung, which was shown to be 2.9 Gy.

In another retrospective study, Yamamoto *et al* (2011c) evaluated the dosimetric effects of incorporation of 4D-CT ventilation imaging in volumetric modulated arc therapy (VMAT) in addition to IMRT planning for 15 lung cancer patients. Six fixed-field coplanar IMRT and single arc VMAT treatment plans, with and without incorporation of ventilation information, were created for each patient. Field arrangements were the same for paired plans incorporating anatomical information only and those incorporating the additional functional information. However, optimization constraints differed, where plans incorporating functional informational had constraints chosen to minimise dose to functional lung while only dose to the total lung parenchyma volumes were minimised for anatomical plans (Yamamoto *et al.*, 2011c). Statistically significant reductions in mean dose to functional lung of 1.8 Gy and 2.0 Gy for IMRT and VMAT were demonstrated, respectively. However, this was to the detriment of the target volume dose conformity and homogeneity.

Caution should be exercised when drawing conclusions from the results of the two aforementioned ventilation CT treatment planning studies. Careful examination of their methodology indicates that the reductions observed could be attributable to their ventilation segmentation methodology, where functional lung parameters were reported as percentile ventilation masks. Yaremko *et al*

(2007) used a threshold mask to delineate the 10% of ventilated lung with the highest value. The method proposed by Yamamoto *et al* (2011c) differed slightly in that the ventilated lung volumes were divided equally into three volumes referred to as low, moderate and highly ventilated lung. The optimisation constraints of the inverse algorithm were prioritised to preferentially reduce the dose to highly ventilated regions. This may explain why a lower reduction in mean dose to functional lung of 1.8 Gy was demonstrated in Yamamoto *et al* (2011c) for IMRT, compared with the 2.7 Gy value in Yaremko *et al* (2007), as the 90% percentile would inevitably lead to smaller ventilated lung volumes.

Both studies do not present a physiological basis for choosing their respective threshold segmentation methods. Furthermore, their methods do not conform to published validation studies evaluating the physiological accuracy against established pulmonary functional imaging modalities. An improved follow-up study would evaluate the dosimetric impact with the raw ventilated volumes derived from the relevant metrics or by established thresholds which have been demonstrated to spatially correspond with competing clinical modalities.

The intra- and inter-session reproducibility of CT ventilation derived from 4D-CT images has also been investigated (Du et al., 2012; Yamamoto et al., 2012) with moderately weak correlations observed in human patient cohorts. One important factor for these discrepancies relevant to functional avoidance planning is the degree of respiratory variation in tidal breathing between scans. As HU values are sensitive to inflation state, the derived CT ventilation surrogates will depend on breathing manoeuvre. These effects have been noted by Mistry *et al.* (2013), who have demonstrated significant differences in CT ventilation derived from 4D-CT and breath-hold. The imaging protocol detailed in Chapter 5 of this thesis has the potential to mitigate these problems by ensuring highly reproducible inflation levels. However, anatomical variations occur between breath-hold and tidal breathing which may have implications for treatment efficacy if patients are treated during free breathing. This would not be an issue if patients are treated during breath-hold.

So far the clinical efficacy of functional image guided treatment planning has not been proven. Ultimately, extensive clinical trials are needed to ensure widespread clinical use of the technique. To this end, three clinical trials have commenced to investigate the clinical utility of CT-based surrogates of ventilation for functional lung avoidance treatment planning (ClinicalTrials.gov: NCT02528942, NCT02308709, NCT02843568).

6.2.2 Radiotherapy assessment

Several CT-based studies have also investigated the effects of radiotherapy on surrogate measures of ventilation. Similar to previous SPECT perfusion and ventilation studies (Marks *et al.*, 1997; Theuws *et al.*, 1998), a general trend in regional function decline post-RT has been observed with CT ventilation measurements for intensity (King *et al.*, 2015) and expansion-based metrics (Ding *et al.*, 2010; Latifi *et al.*, 2013a). These effects tend to occur at higher doses greater than 20 Gy (Ding *et al.*, 2010; King *et al.*, 2015).

Whilst the SPECT studies have investigated lung function changes for more conventional dose fractionation schemes, the CT ventilation studies provide the only functional imaging evidence for ventilation decline after SBRT, where greater ventilation decline has been observed in SBRT compared with conventional RT, perhaps attributable to the larger biological effect of SBRT.

Despite this general trend in post-RT function decline, pulmonary function recovery has also been observed in the CT ventilation literature. Vinogradskiy *et al.* (2012) studied weekly ventilatory changes using the intensity-based metric during the course of treatment and noted reventilation throughout treatment in some patients. This phenomenon was observed particularly in lobes containing tumours, which could be due to airway opening as tumour volume reduces. This was supported by statistically significant reductions in pre-treatment ventilation for lobes containing tumours. Whereas other CT-based studies have chiefly focussed on post-RT effects, with the largest patient study to date (n=30) using data with a median time interval of 1.2 years (range: 0.3-3.3 years) between pre- and post-RT imaging, the study of

Vinogradskiy et al is the only systematic analysis of CT-based regional lung ventilation over the course of treatment. However, their results could be masked by limited patient numbers (n = 6) and uncertainties in ventilation computation; thus caution should be exercised when extrapolating their results and more research is required before making firm conclusions.

The recovery of ventilated lung could limit the ability of functional avoidance strategies to preserve functional regions as the technique is premised on the assumption that the snap shot of functional defects pre-RT remains constant throughout treatment (Ireland *et al.*, 2016). To mitigate these problems, greater personalisation of the technique may be needed via adaptive functional treatment planning by modifying treatment plans throughout treatment according to lung function changes rather than relying solely on pre-RT functional imaging.

6.2.3 Other respiratory diseases

CT based surrogates of ventilation may have wider implications for patients with other respiratory diseases. Obstructive lung diseases in particular such as asthma, COPD and cystic fibrosis are characterised by regionally impaired lung ventilation. CT is already part of the routine radiological assessment of these patients. The CT ventilation technique may facilitate longitudinal ventilation assessment, either due to disease progression or therapeutic intervention, in a way that is not currently possible. For asthmatics, the impact of therapeutic interventions such as bronchial thermoplasty may benefit from the quantitative information produced by ventilation from treatment planning to the assessment of regional pathophysiology response to treatment (Thomen *et al.*, 2015). For COPD patients, regional ventilation can help assess the impact of lung volume reduction surgery (Kurose *et al.*, 2004). For children with cystic fibrosis, an early detection of ventilation dysfunction may enable intervention prior to disease irreversibility (Thomen *et al.*, 2015).

6.3 Limitations and future research directions

6.3.1 Multi-institutional study

Since the introduction of image registration derived CT-based surrogates of ventilation a decade ago, no consensus yet exists as to what is the most accurate pipeline (image registration algorithm and ventilation metric) to use. To this end, the author and several CT ventilation researchers worldwide have launched the first international effort to compare the accuracy of several implementations for generating the ventilation maps. The initial phase of this study constitutes human and animal 4D-CT data from three ventilation studies, paired with Galligas PET, Xenon-CT and DTPA-SPECT. To date, 7 groups from Europe, Australia, USA and Japan have submitted their ventilation maps and have been compared with the assumed ground truth ventilation modalities using the voxel-wise Spearman correlation coefficient. Preliminary results have demonstrated marked differences between algorithms and their performance for certain datasets. A subsequent multi-institutional study will investigate correlation of breath-hold CT against hyperpolarised gas MRI. It is hoped that the insight these studies will provide in understanding algorithmic differences and correlation to other more established measures of ventilation will be a key step towards translation of the technique into the clinic.

6.3.2 Alveolar ventilation vs lung expansion

It could be argued that the term ‘ventilation CT’ applied to this technique is in fact a misnomer as it is not identical to the pulmonary physiologist’s definition of specific ventilation. The physiological definition of specific ventilation is the fractional volume of fresh gas (rather than dead space gas) exchanged at the alveoli per unit time (Simon, 2005; Simon *et al.*, 2012). Simon *et al* (2012) mention that although dead space gas may have an equivalent composition to alveoli gas, its redistribution at the alveoli is not considered ‘fresh gas’ exchange. Consequently, it plays no part in the removal of carbon dioxide from the body (Simon *et al.*, 2012). The so-called ventilation image comprises of both fresh and dead space gas and does not explicitly differentiate between

the two. Therefore, although it may be related to specific ventilation, it is not equivalent. This must be borne in mind when interpreting clinical images. For this reason, instead of the use of misleading terminology, the technique could be referred to as ‘local lung expansion CT’.

6.3.3 Ground truth: Imaging or Histology?

In all comparative validation studies, established imaging modalities taken to be the reference are assumed to represent ground truth. It has been argued that this ground truth assumption is invalid and only true validation of the technique would be through histopathological studies (Simon *et al.*, 2012). As such, an important contribution to the field would be to validate the ventilation surrogates against histologic specimens of human lung tissue.

6.3.4 Perfusion

One major drawback in the clinical translation of CT-based surrogates of ventilation is their inability to provide a complete representation of lung function. The lung’s function of gas exchange comprises both ventilation and perfusion (Zhang *et al.*, 2008). Moreover, it has been suggested that perfusion is more relevant than ventilation because under perfused lung with viable ventilation is more widespread than the reverse (Marks *et al.*, 1999). If it is assumed that the functional information provided by CT can be used as a perfect surrogate for ventilation, there is the risk that a higher dose is received by perfused lung identified as non-ventilated (Ireland *et al.*, 2016). An improved approach would be to incorporate perfusion information in addition to the ventilation information for truly pulmonary functionally guided treatment.

Appendix A
Optimisation of image registration parameters

This chapter provides the justification of the registration algorithm used in the thesis for generating ventilation CT images and demonstrates the experiments undertaken to optimise its parameters.

A.1 Introduction

The goal of image registration is to find the spatial correspondence between at least two images, a fixed image and a moving image. The moving imaging is spatially aligned to the coordinate space of the fixed image. There are three basic components to any registration algorithm: (1) transformation model, (2) cost function and (3) optimiser.

Image registration is normally formulated as an optimisation problem with the aim of finding the optimal spatial transformation that minimises (or maximises) a cost function computed between the aligned images. The cost function comprises of a similarity metric and a regularisation term. The similarity metric quantifies the quality of alignment whilst the regularisation term constrains the possible transformations to physically plausible transformations. Common similarity metrics include those which are based on intensity differences such as the sum of squared differences (SSD), cross-correlation of the intensities such as normalised cross correlation (NCC) and information theory such as the mutual information (MI). SSD assumes that the intensities of corresponding features are identical. NCC assumes that there is a linear relationship between intensities of corresponding features. MI assumes that

there is only a functional relationship between intensities and as such, is most commonly employed for multi-modal registration.

The transformation model refers to the mathematical formulation of spatial mapping between image coordinate spaces. The simplest transformation model is the rigid transformation. In 3D, it has six degrees-of-freedom (three rotations and three translations). The rigid transformation is a subset of the affine transformation which can be characterised by scaling and shearing in addition to rotations and translations (Oliveira and Tavares, 2014). Given the deformable nature of the movement of pulmonary structures, lung image registration algorithms frequently employ curved (or deformable) transformations. A large body of curved transformations have been used for the lungs including those based on B-splines and diffeomorphisms (Murphy *et al.*, 2011).

Ventilation CT images have been shown to be highly sensitive to registration technique (Yamamoto *et al.*, 2011b; Latifi *et al.*, 2013b). In order to generate robust ventilation CT images, accurate registration of inspiratory and expiratory CT is essential. The vast majority of ventilation CT validation studies to date have utilised 4D-CT data, acquired during tidal breathing (Mathew *et al.*, 2012; Castillo *et al.*, 2012; Castillo *et al.*, 2010). However, 4D-CT images are prone to artefacts which have been shown to affect 90% of images (Yamamoto *et al.*, 2008). Furthermore, static ventilation-weighted images of hyperpolarised gas MRI are acquired at breath-hold and thus to improve the spatial correlation of both techniques, it is desirable to acquire pulmonary CT images at breath-hold to mitigate discrepancies in acquisition settings between modalities (Ireland *et al.*, 2008). The motion magnitudes between the maximum inhale and exhale phases of normal tidal breathing are significantly lower than that of paired breath-hold CT images acquired at the extremes of inflation (Castillo *et al.*, 2013). As such, they pose significant challenges for deformable image registration.

This appendix summarises attempts made to parameterise a well-established registration algorithm for a publicly available paired breath-hold reference

dataset, characterised by extreme differences between inhale and exhale. The developers' own settings submitted to an ongoing grand challenge in pulmonary CT registration are employed as a basis for determination of optimal parameters. The optimised parameters are employed in the CT inspiratory and expiratory registration used for the ventilation CT computation in Chapters 4 and 5 of this thesis.

A.2 Methods

A.2.1 Reference dataset and validation

Although several pulmonary CT datasets for validation of deformable registration exist (Vandemeulebroucke *et al.*, 2011), given the large differences between inspiratory and expiratory breath-hold CT used in this thesis (see Chapter 4), image registration was validated by using the mean target registration error (TRE) of 300 corresponding expert landmarks on inspiratory and expiratory breath-hold image pairs for ten COPD patients. The paired images were acquired at the two extremes of inflation. These ten patients were obtained from the DIR-lab dataset (www.dir-lab.com), a publicly available reference dataset acquired from the National Heart Lung Blood Institute COPDgene study archive for the validation of pulmonary deformable registration algorithms (Castillo *et al.*, 2013). For each inspiratory and expiratory image, 300 anatomical landmarks located within the lungs are available. Landmarks were demarcated by a medical expert. The in-plane resolution of the images ranged from 0.586x0.586 to 0.742x0.742 mm. Slice thickness was always 2.5 mm. The TRE is computed by taking the Euclidean distance of a corresponding landmark on the fixed and warped moving image.

A.2.2 Deformable Registration

In this study, the choice of registration software used was based on the best performing algorithm at the time of writing at an ongoing pulmonary image registration competition (EMPIRE10, http://empire10.isi.uu.nl/), which forms part of the MICCAI Grand Challenges in image analysis. The results of this challenge were reported in Murphy *et al.* (2011) where the Greedy symmetric normalization (SyN) algorithm implemented within the Advanced

Normalization Tools (ANTs) registration framework (Avants *et al.*, 2011) attained first place in this challenge. An additional advantage of using this software is that it is open source and its source code is publicly available to the research community. The latest version of the software, referred to as '`antsRegistration`', is based on version 4 of the Insight ToolKit (ITK[4]), a generic C++ medical image processing library revised to benefit from multi-threaded capability (Avants *et al.*, 2012).

To find the optimal parameters for this dataset, a number of parameters were varied, and the mean TRE per patient was calculated. Initial parameters used were based on the developers own submissions to the EMPIRE10 challenge (http://empire10.isi.uu.nl/mainResults.php) where two variants of their Symmetric Normalization (SyN) algorithm was used, one with Gaussian regularization and the other with B-splines. These two settings are referred to here as 'EMPIRE10_Syn' and 'EMPIRE10_BSplineSyn', respectively. Numerous experiments were undertaken to find the optimal parameters for the reference datasets in respect to minimising TRE. In this study, we compare the results of these two scripts with that of an empirically validated optimised parameter script and is referred to here as 'Optimised'.

All three methods are discussed in brief below:

EMPIRE10_Syn

- A coarse pre-alignment rigid transform was applied to align the centres of mass of the fixed and moving image intensities.
- The resulting transform was then applied to rigid and affine stages using the mutual information similarity metric with 32 histogram bins optimised via the gradient descent algorithm with a step size of 0.1.
- A multi-resolution Gaussian pyramid with 4 levels was used with down-sampling factors 8x4x2x1 and corresponding smoothing Gaussian sigmas of 3x2x1x0 mm.
- A maximum of 10,000 iterations were set for each resolution level to ensure convergence (Glocker *et al.*, 2011).

- For the non-rigid stage, the SyN diffeomorphic transform was used with a Gaussian regularization kernel width of 3 voxels for smoothing of the update transform field.
- A 4-level multi-resolution pyramid with down-sampling factors of 6x4x2x1 and corresponding smoothing Gaussian sigmas of 3x2x1x0 mm and the normalized correlation coefficient similarity metric with a radius of 4 voxels were used.
- A step size of 0.1 was selected for the gradient descent optimisation algorithm.

EMPIRE10_BSplineSyn

- For the rigid and affine stages, the same parameters as above were employed.
- An additional diffeomorphic transformation with explicit B-spline regularization (Tustison and Avants, 2013) that copes with larger deformations than the familiar SyN algorithm (Avants *et al.*, 2008) was applied instead to the resulting transform of the affine pipeline with a knot spacing for the update field of 40 mm.
- The same 4-level multi-resolution strategy was employed.

Optimised

- The empirically optimised script used identical rigid and affine parameters as EMPIRE10_Syn and EMPIRE10_BSplineSyn.
- For the deformable stage, the explicit B-spline regularization significantly outperformed the SyN algorithm for the reference dataset and was thus applied to the resulting transform of the affine pipeline.
- A knot spacing for the update field of 65 mm provided optimal results.
- Additionally, a 5-level multi-resolution pyramid was used (instead of 4 levels) with down-sampling factors of 10x6x4x2x1 and corresponding smoothing Gaussian sigmas of 5x3x2x1x0 mm and

the normalized correlation coefficient similarity metric with a radius of 2 voxels instead of 4.

- A step size of 0.2 was selected for the gradient descent optimisation algorithm.

To understand the effects of varying specific parameters on registration accuracy, the following was studied:

Masking

- The effect of limiting the registration to the lungs was investigated for the ‘EMPIRE10_Syn’ and ‘EMPIRE10_BSplineSyn’ registration pipelines.

Multiresolution strategy

- ‘EMPIRE10_Syn’ and ‘EMPIRE10_BSplineSyn’ both employed a 4-level resolution multi-resolution pyramid. To study the effect of using a different number of levels on this dataset, 3- and 5-level multi-resolution pyramids are also studied with down-sampling factors of 4x2x1 and 10x6x4x2x1 and corresponding smoothing Gaussian sigmas of 2x1x0 mm and 5x3x2x1x0 mm, respectively.

To reduce the computational times in performing the three registration pipelines above, 8 cores via an Intel Xeon E5-2670 eight-core processors @ 2.60 GHz were run in parallel on a 64-bit high performance Linux server (Iceberg, University of Sheffield) using the multi-threading options available in ITK[4].

A.3 Results

A.3.1 Effect of masking

The effect of masking on registration accuracy is shown in Table A.1 for the ‘EMPIRE10_Syn’ and ‘EMPIRE10_BSplineSyn’ pipelines. For reference, Euclidian distances between landmarks when no registration was performed are also provided. The results demonstrate marked improvements for both methods when masking is incorporated within the registration (Wilcoxon signed-rank test, $p < 0.05$). Furthermore, B-Spline regularisation is shown to improve registration accuracy compared with that of Gaussian regularization.

A.3.2 Effect of multi-resolution strategy and parameterisation

The results for the mean TREs before registration and for the registration pipelines are displayed in Table A.2. The results show that increasing the number of multi-resolution levels to 5 can significantly improve registration accuracy. The optimised script proposed in this study outperformed all other methods ($p < 0.05$) at the higher multi-resolution levels.

Table A.1 Effect of masking on registration accuracy. Mean and standard deviation of the TREs of the 300 expert landmarks for breath-hold CT reference dataset. Values are given in mm. Euclidian distances between landmarks when no registration was performed are provided for reference.

Registration method	Masking	Mean TRE±SD (mm)
No registration	N/A	23.36±10.11
EMPIRE10_Syn	No	19.18±7.09
	Yes	7.98±3.49
EMPIRE10_BSplineSyn	No	10.16±7.85
	Yes	3.09±1.53

Table A.2 Effect of multi-resolution strategy and parameterisation on registration accuracy. Mean and standard deviation of the TREs of the 300 expert landmarks for breath-hold CT reference dataset. Values are given in mm. Summary statistics are shown for the registration methods compared in this study. Euclidian distances between landmarks when no registration was performed are provided for reference.

Registration method	Multi-resolution levels	Mean TRE±SD (mm)
No registration	N/A	23.36±10.11
EMPIRE10_Syn	3	10.12±3.61
	4	7.98±3.49
	5	5.79±2.83
EMPIRE10_BSplineSyn	3	5.27±2.78
	4	3.09±1.53
	5	2.57±1.07
Optimised	3	6.19±3.60
	4	2.46±1.22
	5	1.26±0.27

A.4 Discussion

Masked registration yielded significant improvements in TRE values for both of the developer's pipelines. This demonstrates the importance of masking when registering pulmonary images acquired at very different inflation levels. All top performing algorithms in the EMPIRE10 challenge incorporated lung masks as part of their registration pipeline (Murphy *et al.*, 2011). Limiting the registration to voxels within the lungs can better account for the sliding motion that occurs at the pleura between the lung parenchyma and the ribcage and improves spatial alignment of structures within the lungs by avoiding high contrast structures such as the ribs (Wu *et al.*, 2008; Murphy *et al.*, 2011). It also has the advantage of reducing overall computational time due to enabling cropping of overall image dimensions. Only whole-lung masks were used in this study; further improvements in registration accuracy may be achieved by constraining registration to a single lung or to the lobes. For the latter, sliding motion of the lobes has also been shown to be important and thus lobar level registration may better account for this phenomenon (Ding *et al.*, 2009). Given the coarse slice thickness of the reference dataset, lobar segmentation was not possible for this dataset as the major (oblique) pulmonary fissures were not detectable on all slices. Slice thicknesses greater than 1.5 mm are generally not recommended for lobar segmentation due to the increased difficulty in discernment of fissures (Doel *et al.*, 2015). Future work will test this hypothesis on higher resolution CT images.

The 'EMPIRE10_Syn' pipeline was consistently outperformed by its B-spline analogue. The parameters of both scripts are identical with the exception of regularisation methods for the deformable stage; the 'EMPIRE10_Syn' employs Gaussian convolution for regularization whilst 'EMPIRE10_BsplineSyn' employs B-spline functions. These results are in line with that of a previous study in the context of brain registration, where the B-spline Syn algorithm was shown to yield statistically significant improvements in dice coefficients compared with the well-known Syn algorithm (Tustison and Avants, 2013). Tustison and Avants (2013) have speculated that the improvement could be due to the continuous nature of B-spline regularization compared to the discrete approximation offered by Gaussian smoothing.

The use of increased multi-resolution levels improved registration accuracy for all scripts. Due to enlarged capture ranges, a greater number of multi-resolution levels are able to capture larger deformations and are thus particularly well suited to the problem in question. Further advantages include improved robustness to local minima during the optimisation process and enhanced computational efficiency (Oliveira and Tavares, 2014).

A significant improvement in registration accuracy compared with the developer's settings was shown for the optimised pipeline developed in this study. Although the developers' settings provided excellent results for the EMPIRE10 challenge data which comprised of a range of data including 4D-CT and breath-hold, it was not specifically optimised for paired breath-hold CT with extreme motion amplitudes. This demonstrates the importance of problem-specific parameterisation for new registration applications.

A.5 Conclusion

Registration accuracy was significantly improved by the use of lung-constrained registration and increased multiresolution levels for all methods studied. Registration accuracy was also significantly improved with B-spline regularization. A parameterised method developed here which built upon the B-Spline Syn parameters proposed by the developers of the algorithm for pulmonary CT registration produced more accurate registrations than the developers' settings for a highly challenging paired breath-hold dataset, demonstrating the importance of parameterisation for specific applications.

Appendix B
Derivation of the formula for determining specific ventilation from paired inspiratory and expiratory CT images

This chapter provides the derivation for the Hounsfield Units based formula for determining voxel-wise specific ventilation maps from spatially aligned inspiratory and expiratory CT images, see also Castillo *et al.* (2010).

Provided no contrast agent is used, the methodology for computing CT-based specific ventilation surrogates as described in section 1.2.1 is premised on the assumption that any given voxel volume comprises of the linear combination of air and tissue and that the tissue volume remains constant between inflation levels. Thus, for a voxel volume at inspiration, this can be expressed as:

$$V_{ins} = V_{air}^{ins} + V_{tissue}$$

The equivalent formulation at expiration is:

$$V_{exp} = V_{air}^{exp} + V_{tissue}$$

Accordingly, the fraction of air in a given voxel at inspiration can be expressed:

$$F_{ins} = \frac{V_{ins} - V_{tissue}}{V_{ins}}$$

At expiration, a similar formula can be shown:

$$F_{exp} = \frac{V_{exp} - V_{tissue}}{V_{ins}}$$

Specific ventilation is assumed to be the air volume change between inspiration and expiration ΔV normalized by the initial air volume at expiration V_{air}^{exp}.

$$\frac{\Delta V}{V_{air}^{exp}} = \frac{V_{air}^{ins} - V_{air}^{exp}}{V_{air}^{exp}}$$

Substitution of the first two equations in this chapter gives:

$$\frac{\Delta V}{V_{air}^{exp}} = \frac{V_{ins} - V_{exp}}{V_{exp} - V_{tissue}}$$

Multiplying the numerator and denominator by V_{tissue} gives:

$$\frac{\Delta V}{V_{air}^{exp}} = \frac{V_{ins}V_{tissue} - V_{exp}V_{tissue}}{V_{tissue}(V_{exp} - V_{tissue})}$$

Next, zero is added to the numerator in the form $V_{exp}V_{ins} - V_{exp}V_{ins}$:

$$\frac{\Delta V}{V_{air}^{exp}} = \frac{V_{exp}V_{ins} - V_{exp}V_{ins} + V_{ins}V_{tissue} - V_{exp}V_{tissue}}{V_{tissue}(V_{exp} - V_{tissue})}$$

Rearranging gives:

$$\frac{\Delta V}{V_{air}^{exp}} = \frac{V_{exp}V_{ins} - V_{exp}V_{tissue} - V_{exp}V_{ins} + V_{ins}V_{tissue}}{V_{tissue}(V_{exp} - V_{tissue})}$$

Next, the denominator is multiplied by $V_{exp}V_{ins}/V_{exp}V_{ins}$:

$$\frac{\Delta V}{V_{air}^{exp}} = \frac{V_{exp}V_{ins} - V_{exp}V_{tissue} - V_{exp}V_{ins} + V_{ins}V_{tissue}}{V_{tissue}(V_{exp} - V_{tissue})\left(\frac{V_{exp}V_{ins}}{V_{exp}V_{ins}}\right)}$$

Factoring terms in both the numerator and denominator gives:

$$\frac{\Delta V}{V_{air}^{exp}} = \frac{V_{exp}(V_{ins} - V_{tissue}) - V_{ins}(V_{exp} - V_{tissue})}{V_{exp}V_{ins}\left(\frac{V_{exp} - V_{tissue}}{V_{exp}}\right)\left(\frac{V_{tissue}}{V_{ins}}\right)}$$

Multiplying both the numerator and denominator by $1/V_{exp}V_{ins}$ and simplifying the result gives:

$$\frac{\Delta V}{V_{air}^{exp}} = \frac{\left(\frac{V_{ins} - V_{tissue}}{V_{ins}}\right) - \left(\frac{V_{exp} - V_{tissue}}{V_{exp}}\right)}{\left(\frac{V_{exp} - V_{tissue}}{V_{exp}}\right)\left(\frac{V_{tissue}}{V_{ins}}\right)}$$

Adding $(V_{ins} - V_{tissue} = 0)$ to the second bracketed expression in the denominator gives:

$$\frac{\Delta V}{V_{air}^{exp}} = \frac{\left(\frac{V_{ins} - V_{tissue}}{V_{ins}}\right) - \left(\frac{V_{exp} - V_{tissue}}{V_{exp}}\right)}{\left(\frac{V_{exp} - V_{tissue}}{V_{exp}}\right)\left(1 - \frac{V_{ins} - V_{tissue}}{V_{ins}}\right)}$$

Finally, substitution of the equations for the voxel fraction of air at inspiration and expiration yields the same result as Guerrero *et al.* (2005):

$$\frac{\Delta V}{V_{air}^{exp}} = \frac{F_{ins} - F_{exp}}{F_{exp}(1 - F_{ins})}$$

Simon (2000) proposed that the fraction of air in a voxel located in a CT image with an associated Hounsfield unit (HU) is equal to:

$$F_{air} = -\frac{HU}{1000}$$

Substituting this equation into the previous equation gives the final expression for generating voxel-wise specific ventilation maps from the HU values of corresponding spatially aligned inspiratory and expiratory CT images:

$$\frac{\Delta V}{V_{air}^{exp}} = 1000\frac{\overline{HU}_{ins} - HU_{exp}}{HU_{exp}(1000 + \overline{HU}_{ins})} \quad .$$

Appendix C
Publications resulting from this thesis

C.1 Journal articles

Tahir BA, Van Holsbeke C, Ireland RH, Swift AJ, Horn FC, Marshall H, Parra-Robles J, Hartley R, Laurencin M, Kay R, Siddiqui S, Brightling CE, Vos W, Wild JM (2016). Comparison of CT-based lobar ventilation with hyperpolarised ^{3}He MRI using image registration. Radiology 278(2):585-92

Tahir BA, Swift A, Marshall H, Parra-Robles J, Hatton MQ, Hartley R, Kay R, Brightling CE, Vos W, Wild JM, Ireland RH (2014). A method for quantitative analysis of regional lung ventilation using deformable image registration of CT and hybrid hyperpolarised gas/1H MRI. Physics in Medicine and Biology 59(23):7267-77

Horn FC, Tahir BA, Stewart NJ, Collier GJ, Norquay G, Leung G, Ireland RH, Parra-Robles J, Marshall H and Wild JM (2014). Lung ventilation volumetry with same-breath acquisition of hyperpolarised gas and proton MRI. NMR in Biomedicine 27(12):1461-7

C.2 Invited review articles

Ireland, RH, Tahir BA, Wild JM, Lee CE, Hatton MQH (2016). Functional image-guided radiotherapy planning for normal lung avoidance. Clinical Oncology 28(11):695-707

C.3 Invited talks

Validation of breath-hold ventilation CT against Hyperpolarised Gas MRI. American Association of Physicists in Medicine Annual Meeting 2014, Austin, Texas

Ventilation CT: Voxel-level comparison with hyperpolarised Helium-3 & Xenon-129 MRI. American Association of Physicists in Medicine Annual Meeting 2016, Washington, DC

C.4 Conference proceedings

Tahir BA, Marshall H, Hart KA, Swinscoe JA, Hatton MQ, Wild JM and Ireland RH. Ventilation CT: Voxel-level comparison with hyperpolarised Helium-3 & Xenon-129 MRI. American Association of Physicists in Medicine Annual Meeting (AAPM) 2016, Washington DC, USA

Tahir BA, Marshall H, Hart KA, Swinscoe JA, Wild JM, Ireland RH and Hatton MQ. CT-based surrogates of pulmonary ventilation in lung cancer: A voxel-level comparison with HP gas MRI. World Conference on Lung Cancer (WCLC) 2016, Vienna, Austria

Tahir BA, Marshall H, Hart KA, Swinscoe JA, Hatton MQ, Wild JM and Ireland RH. Ventilation CT: Voxel-level comparison with HP gas MRI. European Respiratory Society (ERS) International Congress, London, UK

Tahir BA, Marshall H, Hart KA, Swinscoe JA, Hatton MQ, Wild JM and Ireland RH. An image acquisition and analysis strategy for comparison of ventilation CT and HP gas MRI. 7th International Workshop on Pulmonary Functional Imaging (IWPFI) 2015, Edinburgh, Scotland

Tahir BA, Marshall H, Hart KA, Swinscoe JA, Hatton MQ, Wild JM and Ireland RH. A method for the comparison of ventilation CT and hyperpolarised gas MRI. IPEM Medical Physics and Engineering Conference (MPEC) 2015, Liverpool, United Kingdom

Tahir BA, Marshall H, Wild JM, Ireland RH. Comparison of ^{3}He MRI and CT image-based ventilation using deformable image registration. 23rd Annual Meeting of The International Society for Magnetic Resonance in Medicine (ISMRM) 2015, Toronto, Ontario, Canada

Hughes PJC, Tahir BA, Horn FC, Ireland RH, Marshall H, Wild JM. Ventilation-perfusion analysis with co-registered hyperpolarised gas and CE ^{1}H perfusion MRI. 23rd Annual Meeting of The International Society for Magnetic Resonance in Medicine (ISMRM) 2015, Toronto, Ontario, Canada

Tahir BA, Van Holsbeke C, Ireland RH, Swift AJ, Horn FC, Marshall H, Parra-Robles J, Hartley R, Laurencin M, Kay R, Siddiqui S, Brightling CE, Vos W, Wild JM. Comparison of CT-based lobar ventilation models with ^{3}He MRI ventilation measurements in asthmatics. European Respiratory Society (ERS) International Congress 2014, Munich, Germany

Tahir BA, Swift AJ, Marshall H, Leung G, Hatton MQ, Hartley R, Kay R, Brightling CE, Wild JM and Ireland RH. High performance computing for automatic deformable image registration of hyperpolarised ^{3}He MRI to X-ray CT using synchronously

acquired ^{1}H MRI. High Performance Computing Conference 2014, Sheffield, United Kingdom

Tahir BA, Van Holsbeke C, Ireland RH, Swift AJ, Horn FC, Marshall H, Parra-Robles J, Hartley R, Laurencin M, Kay R, Siddiqui S, Brightling CE, Vos W, Wild JM. Comparison of CT-based lobar ventilation models with ^{3}He MRI ventilation measurements in asthmatics. UK Respiratory and Pulmonary Vascular Imaging Meeting 2014, Sheffield, United Kingdom

Tahir BA, Swift AJ, Marshall H, Leung G, Hatton MQ, Hartley R, Kay R, Brightling CE, Wild JM, Ireland RH. Target registration error of diffeomorphic image registration of same breath-hold ^{1}H and hyperpolarised ^{3}He MRI to lung CT. INSIGNEO Showcase 2014, Sheffield, United Kingdom

Tahir BA, Van Holsbeke C, Ireland RH, Swift AJ, Horn FC, Marshall H, Parra-Robles J, Hartley R, Laurencin M, Kay R, Siddiqui S, Brightling CE, Vos W, Wild JM. Comparison of CT-based lobar ventilation models with ^{3}He MRI ventilation measurements in asthmatics. American Thoracic Society (ATS) 2014, San Diego, USA

Tahir BA, Swinscoe JA, Hatton MQ, Wild JM, Ireland RH. Towards validation of breath-hold ventilation CT for NSCLC radiotherapy planning. 12th Annual British Thoracic Oncology Group Conference (BTOG) 2014, Dublin, Ireland

Tahir BA, Swift AJ, Marshall H, Leung G, Hatton MQ, Hartley R, Kay R, Brightling CE, Wild JM, Ireland RH. Image registration accuracy of synchronously acquired ^{1}H and hyperpolarised ^{3}He MRI to X-ray CT for lung cancer treatment planning. UK Radiation Oncology (UKRO) 2013, Nottingham, United Kingdom

Tahir BA, Swift AJ, Marshall H, Leung G, Hatton MQ, Hartley R, Kay R, Brightling CE, Wild JM, Ireland RH. Target registration error of diffeomorphic image registration of same breath-hold ^{1}H and hyperpolarised ^{3}He MRI to lung CT for radiotherapy treatment planning. IPEM Medical Physics and Engineering Conference (MPEC) 2014, Glasgow, Scotland

Tahir BA, Van Holsbeke C, Ireland RH, Swift AJ, Horn FC, Marshall H, Parra-Robles J, Hartley R, Laurencin M, Kay R, Siddiqui S, Brightling CE, Vos W, Wild JM. Comparison of CT-based lobar ventilation with hyperpolarised ^{3}He MRI using image registration. 6th International Workshop on Pulmonary Functional Imaging (IWPFI) 2013, Madison, Wisconsin, USA

C.5 Prizes

6th International Workshop on Pulmonary Functional Imaging (IWPFI) 2013 – Best rapid fire presentation and e-poster

UK Radiation Oncology (UKRO) 2013 – Best poster prize

Bibliography

Aliverti A, Pennati F, Salito C and Woods J C 2013 Regional lung function and heterogeneity of specific gas volume in healthy and emphysematous subjects *Eur Respir J* **41** 1179-88

Altes T A, Powers P L, Knight-Scott J, Rakes G, Platts-Mills T A, de Lange E E, Alford B A, Mugler J P, 3rd and Brookeman J R 2001 Hyperpolarized 3He MR lung ventilation imaging in asthmatics: preliminary findings *Journal of Magnetic Resonance Imaging* **13** 378-84

Avants B, Tustison N, Song G, Wu B, Stauffer M, McCormick M, Johnson H and Gee J 2012 *Biomedical Image Registration,* ed B Dawant*, et al.*: Springer Berlin Heidelberg) pp 266-75

Avants B B, Epstein C L, Grossman M and Gee J C 2008 Symmetric diffeomorphic image registration with cross-correlation: evaluating automated labeling of elderly and neurodegenerative brain *Med Image Anal* **12** 26-41

Avants B B, Tustison N J, Song G, Cook P A, Klein A and Gee J C 2011 A reproducible evaluation of ANTs similarity metric performance in brain image registration *Neuroimage* **54** 2033-44

Bates E L, Bragg C M, Wild J M, Hatton M Q and Ireland R H 2009 Functional image-based radiotherapy planning for non-small cell lung cancer: A simulation study *Radiother Oncol* **93** 32-6

Bezdek J C 1981 *Pattern Recognition with Fuzzy Objective Function Algorithms*: Kluwer Academic Publishers

Boedeker K L, McNitt-Gray M F, Rogers S R, Truong D A, Brown M S, Gjertson D W and Goldin J G 2004 Emphysema: effect of reconstruction algorithm on CT imaging measures *Radiology* **232** 295-301

Brennan D, Schubert L, Diot Q, Castillo R, Castillo E, Guerrero T, Martel M K, Linderman D, Gaspar L E, Miften M, Kavanagh B D and Vinogradskiy Y 2015 Clinical Validation of 4-Dimensional Computed Tomography Ventilation With Pulmonary Function Test Data *International Journal of Radiation Oncology*Biology*Physics* **92** 423-9

Brightling C E, Gupta S, Gonem S and Siddiqui S 2012 Lung damage and airway remodelling in severe asthma *Clin Exp Allergy* **42** 638-49

Brown R H and Mitzner W 1996 Effect of lung inflation and airway muscle tone on airway diameter in vivo *J Appl Physiol (1985)* **80** 1581-8

Callahan J, Hofman M S, Siva S, Kron T, Schneider M E, Binns D, Eu P and Hicks R J 2014 High-resolution imaging of pulmonary ventilation and perfusion with 68Ga-VQ respiratory gated (4-D) PET/CT *Eur J Nucl Med Mol Imaging* **41** 343-9

Castillo E, Castillo R, Vinogradskiy Y and Guerrero T 2017 The numerical stability of transformation-based CT ventilation *International Journal of Computer Assisted Radiology and Surgery* 1-12

Castillo R, Castillo E, Fuentes D, Ahmad M, Wood A M, Ludwig M S and Guerrero T 2013 A reference dataset for deformable image registration spatial accuracy evaluation using the COPDgene study archive *Phys Med Biol* **58** 2861-77

Castillo R, Castillo E, Martinez J and Guerrero T 2010 Ventilation from four-dimensional computed tomography: density versus Jacobian methods *Phys Med Biol* **55** 4661-85

Castillo R, Castillo E, McCurdy M, Gomez D R, Block A M, Bergsma D, Joy S and Guerrero T 2012 Spatial correspondence of 4D CT ventilation and SPECT pulmonary perfusion defects in patients with malignant airway stenosis *Phys Med Biol* **57** 1855-71

Christian J A, Partridge M, Nioutsikou E, Cook G, McNair H A, Cronin B, Courbon F, Bedford J L and Brada M 2005 The incorporation of SPECT functional lung imaging into inverse radiotherapy planning for non-small cell lung cancer *Radiotherapy and Oncology* **77**

Chuang K-S, Tzeng H-L, Chen S, Wu J and Chen T-J 2006 Fuzzy c-means clustering with spatial information for image segmentation *Computerized Medical Imaging and Graphics* **30** 9-15

Couser J I, Martinez F J, Celli B R and Rassulo J 1992 Respiratory response and ventilatory muscle recruitment during arm elevation in normal subjects *Chest* **101**

Coxson H O, Mayo J R, Behzad H, Moore B J, Verburgt L M, Staples C A, Pare P D and Hogg J C 1995 Measurement of lung expansion with computed tomography and comparison with quantitative histology *J Appl Physiol (1985)* **79** 1525-30

Crawford A B, Makowska M, Paiva M and Engel L A 1985 Convection- and diffusion-dependent ventilation maldistribution in normal subjects *J Appl Physiol (1985)* **59** 838-46

De Backer J W, Vos W G, Vinchurkar S C, Claes R, Drollmann A, Wulfrank D, Parizel P M, Germonpre P and De Backer W 2010 Validation of computational fluid dynamics in CT-based airway models with SPECT/CT *Radiology* **257** 854-62

de Lange E E, Altes T A, Patrie J T, Gaare J D, Knake J J, Mugler J P, 3rd and Platts-Mills T A 2006 Evaluation of asthma with hyperpolarized helium-3 MRI: correlation with clinical severity and spirometry *Chest* **130** 1055-62

Dimick J B, Chen S L, Taheri P A, Henderson W G, Khuri S F and Campbell Jr D A 2004 Hospital costs associated with surgical complications: A report from the private-sector National Surgical Quality Improvement Program *Journal of the American College of Surgeons* **199** 531-7

Ding K, Bayouth J E, Buatti J M, Christensen G E and Reinhardt J M 2010 4DCT-based measurement of changes in pulmonary function following a course of radiation therapy *Medical Physics* **37** 1261

Ding K, Cao K, Fuld M K, Du K, Christensen G E, Hoffman E A and Reinhardt J M 2012 Comparison of image registration based measures of regional lung ventilation from dynamic spiral CT with Xe-CT *Med Phys* **39** 5084-98

Ding K, Yin Y, Cao K, Christensen G E, Lin C-L, Hoffman E A and Reinhardt J M 2009 Evaluation of Lobar Biomechanics during Respiration Using Image Registration. In: *Proceedings of the 12th International Conference on Medical Image Computing and Computer-Assisted Intervention: Part I,* (London, UK: Springer-Verlag) pp 739-46

Doel T, Gavaghan D J and Grau V 2015 Review of automatic pulmonary lobe segmentation methods from CT *Comput Med Imaging Graph* **40** 13-29

Du K, Bayouth J E, Cao K, Christensen G E, Ding K and Reinhardt J M 2012 Reproducibility of registration-based measures of lung tissue expansion *Med Phys* **39** 1595-608

Eslick E M, Bailey D L, Harris B, Kipritidis J, Stevens M, Li B T, Bailey E, Gradinscak D, Pollock S, Htun C, Turner R, Eade T, Aslani A, Snowdon G and Keall P J 2016 Measurement of preoperative lobar lung function with computed tomography ventilation imaging: progress towards rapid stratification of lung cancer lobectomy patients with abnormal lung function *Eur J Cardiothorac Surg* **49** 1075-82

Fedorov A, Beichel R, Kalpathy-Cramer J, Finet J, Fillion-Robin J, Pujol S, Bauer C, Jennings D, Fennessy F, Sonka M, Buatti J, Aylward S, Miller J, Pieper S and Kikinis R 2012 3D Slicer as an image computing platform for the Quantitative Imaging Network *Magnetic Resonance Imaging* **30** 1323-41

Fuld M K, Easley R B, Saba O I, Chon D, Reinhardt J M, Hoffman E A and Simon B A 2008 CT-measured regional specific volume change reflects regional ventilation in supine sheep *J Appl Physiol* **104** 1177-84

Fuld M K, Halaweish A F, Haynes S E, Divekar A A, Guo J and Hoffman E A 2013 Pulmonary perfused blood volume with dual-energy CT as surrogate for pulmonary perfusion assessed with dynamic multidetector CT *Radiology* **267** 747-56

Gibson G J, Loddenkemper R, Lundback B and Sibille Y 2013 Respiratory health and disease in Europe: the new European Lung White Book *Eur Respir J* **42** 559-63

Glenny R W 2009 Determinants of regional ventilation and blood flow in the lung *Intensive Care Medicine* **35**

Glocker B, Sotiras A, Komodakis N and Paragios N 2011 Deformable Medical Image Registration: Setting the State of the Art with Discrete Methods *Annu Rev Biomed Eng* **13** 219-44

Guerrero T, Sanders K, Castillo E, Zhang Y, Bidaut L, Pan T and Komaki R 2006 Dynamic ventilation imaging from four-dimensional computed tomography *Phys Med Biol* **51** 777-91

Guerrero T, Sanders K, Noyola-Martinez J, Castillo E, Zhang Y, Tapia R, Guerra R, Borghero Y and Komaki R 2005 Quantification of regional ventilation from treatment planning CT *Int J Radiat Oncol Biol Phys* **62** 630-4

Halaweish A F, Hoffman E A, Thedens D R, Fuld M K, Sieren J P and van Beek E J 2013 Effect of lung inflation level on hyperpolarized 3He apparent diffusion coefficient measurements in never-smokers *Radiology* **268** 572-80

Hochhegger B, Irion K L, Marchiori E and Moreira J S 2011 Reconstruction algorithms influence the follow-up variability in the longitudinal CT emphysema index measurements *Korean J Radiol* **12** 169-75

Hogg J C and Nepszy S 1969 Regional lung volume and pleural pressure gradient estimated from lung density in dogs *J Appl Physiol* **27** 198-203

Hong C, Leawoods J C, Yablonskiy D A, Leyendecker J R, Bae K T, Pilgram T K, Woodard P K, Conradi M S and Zheng J 2005 Feasibility of combining MR perfusion, angiography, and 3He ventilation imaging for evaluation of lung function in a porcine model *Acad Radiol* **12** 202-9

Horn F C, Tahir B A, Stewart N J, Collier G J, Norquay G, Leung G, Ireland R H, Parra-Robles J, Marshall H and Wild J M 2014 Lung ventilation volumetry with same-breath acquisition of hyperpolarized gas and proton MRI *NMR Biomed* **27** 1461-7

Ireland R, Woodhouse N, Swinscoe J A, Hatton M Q and M. W J 2009 Towards automatic image registration of hyperpolarized 3He MRI and x-ray CT images of the lung *Proc Intl Soc Mag Reson Med* **17**

Ireland R H, Bragg C M, McJury M, Woodhouse N, Fichele S, van Beek E J, Wild J M and Hatton M Q 2007a Feasibility of image registration and intensity-modulated radiotherapy planning with hyperpolarized helium-3 magnetic resonance imaging for non-small-cell lung cancer *Int J Radiat Oncol Biol Phys* **68** 273-81

Ireland R H, Dyker K E, Barber D C, Wood S M, Hanney M B, Tindale W B, Woodhouse N, Hoggard N, Conway J and Robinson M H 2007b Nonrigid image registration for head and neck cancer radiotherapy treatment planning with PET/CT *Int J Radiat Oncol Biol Phys* **68** 952-7

Ireland R H, Tahir B A, Wild J M, Lee C E and Hatton M Q 2016 Functional Image-guided Radiotherapy Planning for Normal Lung Avoidance *Clin Oncol (R Coll Radiol)* **28** 695-707

Ireland R H, Woodhouse N, Hoggard N, Swinscoe J A, Foran B H, Hatton M Q and Wild J M 2008 An image acquisition and registration strategy for the fusion of hyperpolarized helium-3 MRI and x-ray CT images of the lung *Phys Med Biol* **53** 6055-63

Jacob R E, Lamm W J, Einstein D R, Krueger M A, Glenny R W and Corley R A 2015 Comparison of CT-derived ventilation maps with deposition patterns of inhaled microspheres in rats *Exp Lung Res* **41** 135-45

Jensen A, Atileh H, Suki B, Ingenito E P and Lutchen K R 2001 Selected contribution: airway caliber in healthy and asthmatic subjects: effects of bronchial challenge and deep inspirations *J Appl Physiol (1985)* **91** 506-15; discussion 4-5

Jogi J, Jonson B, Ekberg M and Bajc M 2010 Ventilation-Perfusion SPECT with (99m)Tc-DTPA Versus Technegas: A Head-to-Head Study in Obstructive and Nonobstructive Disease *Journal of Nuclear Medicine* **51**

Kabus S, Klinder T, Murphy K, Ginneken B, Lorenz C and Pluim J W 2009 *Medical Image Computing and Computer-Assisted Intervention – MICCAI 2009,* ed G-Z Yang*, et al.*: Springer Berlin Heidelberg) pp 747-54

Kauczor H U, Hofmann D, Kreitner K F, Nilgens H, Surkau R, Heil W, Potthast A, Knopp M V, Otten E W and Thelen M 1996 Normal and abnormal pulmonary ventilation: visualization at hyperpolarized He-3 MR imaging *Radiology* **201** 564-8

King M T, Maxim P G, Diehn M, Loo B W, Jr. and Xing L 2015 Analysis of Long-Term 4-Dimensional Computed Tomography Regional Ventilation After Radiation Therapy *Int J Radiat Oncol Biol Phys* **92** 683-90

Kipritidis J, Hofman M S, Siva S, Callahan J, Le Roux P Y, Woodruff H C, Counter W B and Keall P J 2016 Estimating lung ventilation directly from 4D CT Hounsfield unit values *Med Phys* **43** 33

Kipritidis J, Siva S, Hofman M S, Callahan J, Hicks R J and Keall P J 2014 Validating and improving CT ventilation imaging by correlating with ventilation 4D-PET/CT using 68Ga-labeled nanoparticles *Med Phys* **41** 011910

Kirby M, Mathew L, Heydarian M, Etemad-Rezai R, McCormack D G and Parraga G 2011 Chronic obstructive pulmonary disease: quantification of bronchodilator effects by using hyperpolarized (3)He MR imaging *Radiology* **261** 283-92

Kirby M, Svenningsen S, Kanhere N, Owrangi A, Wheatley A, Coxson H O, Santyr G E, Paterson N A, McCormack D G and Parraga G 2013 Pulmonary ventilation visualized using hyperpolarized helium-3 and xenon-129 magnetic resonance imaging: differences in COPD and relationship to emphysema *J Appl Physiol (1985)* **114** 707-15

Kurose T, Okumura Y, Sato S, Yamamoto Y, Akaki S, Takeda Y, Kanazawa S, Ando A, Date H, Shimizu N and Hiraki Y 2004 Functional evaluation of lung by Xe-133 lung ventilation scintigraphy before and after lung volume reduction surgery (LVRS) in patients with pulmonary emphysema *Acta Med Okayama* **58** 7-15

Latifi K, Feygelman V, Moros E G, Dilling T J, Stevens C W and Zhang G G 2013a Normalization of ventilation data from 4D-CT to facilitate comparison between datasets acquired at different times *PLoS ONE* **8** e84083

Latifi K, Forster K M, Hoffe S E, Dilling T J, van Elmpt W, Dekker A and Zhang G G 2013b Dependence of ventilation image derived from 4D CT on deformable image registration and ventilation algorithms *J Appl Clin Med Phys* **14** 4247

Lederlin M and Crémillieux Y 2013 Three-dimensional assessment of lung tissue density using a clinical ultrashort echo time at 3 tesla: A feasibility study in healthy subjects *J Magn Reson Imaging*

Magnant J, Vecellio L, De Monte M, Grimbert D, Valat C, Boissinot E, Guilloteau D, Lemarie E and Diot P 2006 Comparative analysis of different scintigraphic approaches to assess pulmonary ventilation *Journal of Aerosol Medicine-Deposition Clearance and Effects in the Lung* **19**

Marks L B, Munley M T, Spencer D P, Sherouse G W, Bentel G C, Hoppenworth J, Chew M, Jaszczak R J, Coleman R E and Prosnitz L R 1997 Quantification of radiation-induced regional lung injury with perfusion imaging *International Journal of Radiation Oncology*Biology*Physics* **38** 399-409

Marks L B, Sherouse G W, Munley M T, Bentel G C and Spencer D P 1999 Incorporation of functional status into dose-volume analysis *Medical Physics* **26** 196-9

Marshall H, Deppe M H, Parra-Robles J, Hillis S, Billings C G, Rajaram S, Swift A, Miller S R, Watson J H, Wolber J, Lipson D A, Lawson R and Wild J M 2012 Direct visualisation of collateral ventilation in COPD with hyperpolarised gas MRI *Thorax* **67** 613-7

Mathew L, Wheatley A, Castillo R, Castillo E, Rodrigues G, Guerrero T and Parraga G 2012 Hyperpolarized (3)He Magnetic Resonance Imaging: Comparison with Four-dimensional X-ray Computed Tomography Imaging in Lung Cancer *Acad Radiol* **19** 1546-53

Milic-Emili J 2011 *Comprehensive Physiology*: John Wiley & Sons, Inc.
Milic-Emili J, Henderson J A, Dolovich M B, Trop D and Kaneko K 1966 Regional distribution of inspired gas in the lung *J Appl Physiol* **21** 749-59
Mistry N N, Diwanji T, Shi X, Pokharel S, Feigenberg S, Scharf S M and D'Souza W D 2013 Evaluation of fractional regional ventilation using 4D-CT and effects of breathing maneuvers on ventilation *Int J Radiat Oncol Biol Phys* **87** 825-31
Mugler J P, 3rd, Altes T A, Ruset I C, Dregely I M, Mata J F, Miller G W, Ketel S, Ketel J, Hersman F W and Ruppert K 2010 Simultaneous magnetic resonance imaging of ventilation distribution and gas uptake in the human lung using hyperpolarized xenon-129 *Proc Natl Acad Sci U S A* **107** 21707-12
Muradyan I, Loring S H, Ferrigno M, Lindholm P, Topulos G P, Patz S and Butler J P 2010 Inhalation heterogeneity from subresidual volumes in elite divers *J Appl Physiol (1985)* **109** 1969-73
Murphy K, van Ginneken B, Reinhardt J M, Kabus S, Ding K, Deng X, Cao K, Du K, Christensen G E, Garcia V, Vercauteren T, Ayache N, Commowick O, Malandain G, Glocker B, Paragios N, Navab N, Gorbunova V, Sporring J, de Bruijne M, Han X, Heinrich M P, Schnabel J A, Jenkinson M, Lorenz C, Modat M, McClelland J R, Ourselin S, Muenzing S E, Viergever M A, De Nigris D, Collins D L, Arbel T, Peroni M, Li R, Sharp G C, Schmidt-Richberg A, Ehrhardt J, Werner R, Smeets D, Loeckx D, Song G, Tustison N, Avants B, Gee J C, Staring M, Klein S, Stoel B C, Urschler M, Werlberger M, Vandemeulebroucke J, Rit S, Sarrut D and Pluim J P 2011 Evaluation of registration methods on thoracic CT: the EMPIRE10 challenge *IEEE Trans Med Imaging* **30** 1901-20
Norquay G, Parnell S R, Xu X, Parra-Robles J and Wild J M 2013 Optimized production of hyperpolarized 129Xe at 2 bars for in vivo lung magnetic resonance imaging *Journal of Applied Physics* **113**
Oliveira F P and Tavares J M 2014 Medical image registration: a review *Comput Methods Biomech Biomed Engin* **17** 73-93
Otsu N 1979 A Threshold Selection Method from Gray-Level Histograms *IEEE Trans Syst Man Cybern* **9** 62-6
Papi A, Casoni G, Caramori G, Guzzinati I, Boschetto P, Ravenna F, Calia N, Petruzzelli S, Corbetta L, Cavallesco G, Forini E, Saetta M, Ciaccia A and Fabbri L M 2004 COPD increases the risk of squamous histological subtype in smokers who develop non-small cell lung carcinoma *Thorax* **59** 679-81
Partridge M, Yamamoto T, Grau C, Hoyer M and Muren L P 2010 Imaging of normal lung, liver and parotid gland function for radiotherapy *Acta Oncol* **49** 997-1011
Patz S, Hersman F W, Muradian I, Hrovat M I, Ruset I C, Ketel S, Jacobson F, Topulos G P, Hatabu H and Butler J P 2007 Hyperpolarized (129)Xe MRI: a viable functional lung imaging modality? *Eur J Radiol* **64** 335-44
Pennati F, Salito C, Baroni G, Woods J and Aliverti A 2014 Comparison between multivolume CT-based surrogates of regional ventilation in healthy subjects *Acad Radiol* **21** 1268-75

Petersson J, Sanchez-Crespo A, Larsson S A and Mure M 2007 Physiological imaging of the lung: single-photon-emission computed tomography (SPECT) *J Appl Physiol (1985)* **102** 468-76

Rajaram S, Swift A J, Capener D, Telfer A, Davies C, Hill C, Condliffe R, Elliot C, Hurdman J, Kiely D G and Wild J M 2012 Lung Morphology Assessment with Balanced Steady-State Free Precession MR Imaging Compared with CT *Radiology* **263** 569-77

Reinhardt J M, Ding K, Cao K, Christensen G E, Hoffman E A and Bodas S V 2008 Registration-based estimates of local lung tissue expansion compared to xenon CT measures of specific ventilation *Med Image Anal* **12** 752-63

Rizi R R, Saha P K, Wang B, Ferrante M A, Lipson D, Baumgardner J and Roberts D A 2003 Co-registration of acquired MR ventilation and perfusion images--validation in a porcine model *Magn Reson Med* **49** 13-8

Rodrigues G, Lock M, D'Souza D, Yu E and Van Dyk J 2004 Prediction of radiation pneumonitis by dose-volume histogram parameters in lung cancer - a systematic review *Radiotherapy and Oncology* **71**

Samee S, Altes T, Powers P, de Lange E E, Knight-Scott J, Rakes G, Mugler Iii J P, Ciambotti J M, Alford B A, Brookeman J R and Platts-Mills T A E 2003 Imaging the lungs in asthmatic patients by using hyperpolarized helium-3 magnetic resonance: Assessment of response to methacholine and exercise challenge *Journal of Allergy and Clinical Immunology* **111** 1205-11

Scichilone N and Togias A 2004 The role of lung inflation in airway hyperresponsiveness and in asthma *Curr Allergy Asthma Rep* **4** 166-74

Seppenwoolde Y, Engelsman M, De Jaeger K, Muller S, Belderbos J, Boersma L and Lebesque J 2000 Optimising radiation treatment plans for lung cancer using functional information *Radiotherapy and Oncology* **56**

Simon B A 2000 Non-invasive imaging of regional lung function using X-ray computed tomography *Journal of Clinical Monitoring and Computing* **16** 433-42

Simon B A 2005 Regional ventilation and lung mechanics using X-Ray CT *Acad Radiol* **12** 1414-22

Simon B A, Kaczka D W, Bankier A A and Parraga G 2012 What can computed tomography and magnetic resonance imaging tell us about ventilation? *J Appl Physiol* **113** 647-57

Slats A M, Janssen K, van Schadewijk A, van der Plas D T, Schot R, van den Aardweg J G, de Jongste J C, Hiemstra P S, Mauad T, Rabe K F and Sterk P J 2007 Bronchial inflammation and airway responses to deep inspiration in asthma and chronic obstructive pulmonary disease *Am J Respir Crit Care Med* **176** 121-8

Stewart N J, Norquay G, Griffiths P D and Wild J M 2015 Feasibility of human lung ventilation imaging using highly polarized naturally abundant xenon and optimized three-dimensional steady-state free precession *Magn Reson Med* **74** 346-52

Svenningsen S, Kirby M, Starr D, Leary D, Wheatley A, Maksym G N, McCormack D G and Parraga G 2013 Hyperpolarized (3) He and (129)

Xe MRI: differences in asthma before bronchodilation *J Magn Reson Imaging* **38** 1521-30

Tahir B A, Holsbeke C V, Ireland R H, Swift A J, Marshall H, Parra-Robles J, Hartley R, Laurencin M, Kay R, Siddiqui S, Brightling C E, Backer J D, Vos W and Wild J M 2014a *A108. LUNG IMAGING: STATE OF PLAY ON STRUCTURE AND FUNCTION*: American Thoracic Society) pp A2391-A

Tahir Bilal A, Swift Andrew J, Marshall H, Parra-Robles J, Hatton Matthew Q, Hartley R, Kay R, Brightling Christopher E, Vos W, Wild Jim M and Ireland Rob H 2014b A method for quantitative analysis of regional lung ventilation using deformable image registration of CT and hybrid hyperpolarized gas/ 1 H MRI *Phys Med Biol* **59** 7267

Theuws J C M, Kwa S L S, Wagenaar A C, Boersma L J, Damen E M F, Muller S H, Baas P and Lebesque J V 1998 Dose–effect relations for early local pulmonary injury after irradiation for malignant lymphoma and breast cancer *Radiotherapy and Oncology* **48** 33-43

Thomen R P, Sheshadri A, Quirk J D, Kozlowski J, Ellison H D, Szczesniak R D, Castro M and Woods J C 2015 Regional ventilation changes in severe asthma after bronchial thermoplasty with (3)He MR imaging and CT *Radiology* **274** 250-9

Tomasi C and Manduchi R 1998 Bilateral Filtering for Gray and Color Images. In: *Proceedings of the Sixth International Conference on Computer Vision*: IEEE Computer Society) p 839

Tustison N J and Avants B B 2013 Explicit B-spline regularization in diffeomorphic image registration *Front Neuroinform* **7** 39

Tzeng Y-S, Lutchen K and Albert M 2009 *The difference in ventilation heterogeneity between asthmatic and healthy subjects quantified using hyperpolarized 3He MRI* vol 106

van Beek E J, Hill C, Woodhouse N, Fichele S, Fleming S, Howe B, Bott S, Wild J M and Taylor C J 2007 Assessment of lung disease in children with cystic fibrosis using hyperpolarized 3-Helium MRI: comparison with Shwachman score, Chrispin-Norman score and spirometry *Eur Radiol.* **17** 1018-24. Epub 2006 Aug 29.

van Beek E J, Wild J M, Kauczor H U, Schreiber W, Mugler J P, 3rd and de Lange E E 2004 Functional MRI of the lung using hyperpolarized 3-helium gas *J Magn Reson Imaging* **20** 540-54

van Rikxoort E M and van Ginneken B 2013 Automated segmentation of pulmonary structures in thoracic computed tomography scans: a review *Phys Med Biol* **58** R187-R220

Vandemeulebroucke J, Rit S, Kybic J, Clarysse P and Sarrut D 2011 Spatiotemporal motion estimation for respiratory-correlated imaging of the lungs *Med Phys* **38** 166-78

Venkat R B, Sawant A, Suh Y, George R and Keall P J 2008 Development and preliminary evaluation of a prototype audiovisual biofeedback device incorporating a patient-specific guiding waveform *Phys Med Biol* **53**

Vinogradskiy Y Y, Castillo R, Castillo E, Chandler A, Martel M K and Guerrero T 2012 Use of weekly 4DCT-based ventilation maps to quantify changes in lung function for patients undergoing radiation therapy *Med Phys* **39** 289-98

Wild J M, Ajraoui S, Deppe M H, Parnell S R, Marshall H, Parra-Robles J and Ireland R H 2011 Synchronous acquisition of hyperpolarised 3He and 1H MR images of the lungs - maximising mutual anatomical and functional information *NMR Biomed* **24** 130-4

Wild J M, Marshall H, Bock M, Schad L R, Jakob P M, Puderbach M, Molinari F, Van Beek E J R and Biederer J 2012 MRI of the lung (1/3): methods *Insights into Imaging* **3** 345-53

Wild J M, Marshall H, Xu X, Norquay G, Parnell S R, Clemence M, Griffiths P D and Parra-Robles J 2013 Simultaneous Imaging of Lung Structure and Function with Triple-Nuclear Hybrid MR Imaging *Radiology* **267** 251-5

Wild J M, Woodhouse N, Paley M N, Fichele S, Said Z, Kasuboski L and van Beek E J 2004 Comparison between 2D and 3D gradient-echo sequences for MRI of human lung ventilation with hyperpolarized 3He *Magnetic Resonance in Medicine* **52** 673-8

Woodhouse N, Wild J, van Beek E, Hoggard N, Barker N and Taylor C 2009 Assessment of Hyperpolarized He-3 Lung MRI for Regional Evaluation of Interventional Therapy: A Pilot Study in Pediatric Cystic Fibrosis *Journal of Magnetic Resonance Imaging* **30** 981-8

Woodhouse N, Wild J M, Paley M N, Fichele S, Said Z, Swift A J and van Beek E J 2005 Combined helium-3/proton magnetic resonance imaging measurement of ventilated lung volumes in smokers compared to never-smokers *J Magn Reson Imaging* **21** 365-9

Wu Z, Rietzel E, Boldea V, Sarrut D and Sharp G C 2008 Evaluation of deformable registration of patient lung 4DCT with subanatomical region segmentations *Med Phys* **35** 775-81

Yamamoto T, Kabus S, Berg J v, Lorenz C, Loo M L G W and Keall P J *Proc. 3rd Int. Workshop on Pulmonary Image Analysis,2010),* vol. Series*)* pp 117–28

Yamamoto T, Kabus S, Klinder T, Lorenz C, von Berg J, Blaffert T, Loo B W, Jr. and Keall P J 2011a Investigation of four-dimensional computed tomography-based pulmonary ventilation imaging in patients with emphysematous lung regions *Phys Med Biol* **56** 2279-98

Yamamoto T, Kabus S, Klinder T, von Berg J, Lorenz C, Loo B W and Keall P J 2011b Four-dimensional computed tomography pulmonary ventilation images vary with deformable image registration algorithms and metrics *Medical Physics* **38** 1348

Yamamoto T, Kabus S, Lorenz C, Mittra E, Hong J C, Chung M, Eclov N, To J, Diehn M, Loo Jr B W and Keall P J 2014 Pulmonary Ventilation Imaging Based on 4-Dimensional Computed Tomography: Comparison With Pulmonary Function Tests and SPECT Ventilation Images *International Journal of Radiation Oncology*Biology*Physics* **90** 414-22

Yamamoto T, Kabus S, von Berg J, Lorenz C, Chung M P, Hong J C, Loo B W, Jr. and Keall P J 2012 Reproducibility of Four-dimensional Computed Tomography-based Lung Ventilation Imaging *Acad Radiol* **19** 1554-65

Yamamoto T, Kabus S, von Berg J, Lorenz C and Keall P J 2011c Impact of four-dimensional computed tomography pulmonary ventilation imaging-based functional avoidance for lung cancer radiotherapy *Int J Radiat Oncol Biol Phys* **79** 279-88

Yamamoto T, Langner U, Loo B W, Jr., Shen J and Keall P J 2008 Retrospective analysis of artifacts in four-dimensional CT images of 50 abdominal and thoracic radiotherapy patients *International Journal of Radiation Oncology Biology Physics* **72**

Yaremko B P, Guerrero T M, Noyola-Martinez J, Guerra R, Lege D G, Nguyen L T, Balter P A, Cox J D and Komaki R 2007 Reduction of normal lung irradiation in locally advanced non-small-cell lung cancer patients, using ventilation images for functional avoidance *Int J Radiat Oncol Biol Phys* **68** 562-71

Yuan S, Frey K A, Gross M D, Hayman J A, Arenberg D, Curtis J L, Cai X-W, Ramnath N, Kalemkerian G P, Ten Haken R K, Eisbruch A and Kong F-M 2011 Semiquantification and Classification of Local Pulmonary Function by V/Q Single Photon Emission Computed Tomography in Patients with Non-small Cell Lung Cancer Potential Indication for Radiotherapy Planning *Journal of Thoracic Oncology* **6**

Zhang G, Dilling T J, Stevens C W and Forster K M 2008 Functional lung imaging in thoracic cancer radiotherapy *Cancer control : journal of the Moffitt Cancer Center* **15** 112-9

Zhang G, Huang T C, Dilling T, Stevens C and Forster K 2011 Comments on 'Ventilation from four-dimensional computed tomography: density versus Jacobian methods' *Phys Med Biol* **56** 3445-6

Zhang G G, Huang T C, Dilling T, Stevens C and Forster K M 2010 *World Congress on Medical Physics and Biomedical Engineering, September 7 - 12, 2009, Munich, Germany,* ed O Dössel and W Schlegel: Springer Berlin Heidelberg) pp 1834-7

Zhang G G, Latifi K, Du K, Reinhardt J M, Christensen G E, Ding K, Feygelman V and Moros E G 2016 Evaluation of the DeltaV 4D CT ventilation calculation method using in vivo xenon CT ventilation data and comparison to other methods *J Appl Clin Med Phys* **17** 5985

Zou K H, Tuncali K and Silverman S G 2003 Correlation and simple linear regression *Radiology* **227**